

# **Elucidating a Conserved Myosin XI-RabE GTPase Interaction that is Required for Polarized Cell Growth in Plants**

A Dissertation

Submitted to the Faculty of

WORCESTER POLYTECHNIC INSTITUTE

in Partial Fulfillment of the Requirement for the Degree of

Doctor of Philosophy

in

Biology and Biotechnology

July 31, 2020

by

---

**Robert George Orr**

## **Approved by:**

---

Dr. Luis Vidali  
Associate Professor  
Dept. Biology & Biotechnology  
Worcester Polytechnic Institute

---

Dr. Mary Munson  
Professor  
Dept. Biochemistry and Molecular  
Pharmacology  
University of Massachusetts  
Medical School

---

Dr. Elizabeth F. Ryder  
Associate Professor  
Dept. Biology & Biotechnology  
Worcester Polytechnic Institute

---

Dr. Amity L. Manning  
Assistant Professor  
Dept. Biology & Biotechnology  
Worcester Polytechnic Institute

# Table of Contents

---

	Page
List of Figures.....	iii
Acknowledgements .....	v
Preface.....	vi
Abstract.....	1
Chapter 1 : Polarized Cell Growth in Plants and the Loss-of-Function Tools that Facilitate Our Understanding.....	3
1.1 Introduction .....	4
1.2 <i>Physcomitrella/Physcomitrium patens</i> : A Versatile Plant Model for Cellular Polarized Growth .....	7
1.3 Cytoskeletal Coordination .....	9
1.4 Exocytosis.....	14
1.4.1 Rab GTPases .....	16
1.5 The Apical Plasma Membrane .....	17
1.6 Endocytosis.....	18
1.7 Outlook and Insights from Other Tip Growing Systems .....	20
1.8 Directed Loss-of-Function Approaches in Plant Functional Genomics .....	22
1.8.1 Homology Directed Repair.....	23
1.8.2 CRISPR/Cas.....	24
1.8.3 RNA Interference .....	29
1.9 Concluding Remarks.....	33
Chapter 2 : Robust survival-based RNAi of gene families using in tandem silencing of adenine phosphoribosyltransferase .....	35
2.1 Abstract.....	36
2.2 Introduction .....	36
2.3 Results.....	41
2.3.1 Development of A Novel Positive Selection RNAi Methodology Based on Endogenous APT Activity .....	41
2.3.2 APTi Experimental Design for High-throughput Phenotyping .....	45

2.3.3 The APTi System Silences the Myosin XI Family with High Efficacy .....	49
2.3.4 APTi-based Silencing of the Lyk5 Family Disrupts <i>P. patens</i> ' Response to Chitin Oligosaccharides .....	56
2.4 Discussion.....	62
2.5 Conclusions .....	67
2.6 Materials and Methods.....	67
2.6.1 Plant Materials and Culture Conditions.....	67
2.6.2 APT-based RNAi Construct Design .....	68
2.6.3 APTi Phenotyping Assay .....	70
2.6.4 Analysis of Myosin XI Protein Abundance .....	71
2.6.5 Lyk5-RNAi Construct Design and Functional Assay .....	72
Chapter 3 : RabE and its Interaction with Myosin XI are Essential for Cell Polarization and Growth.....	75
3.1 Abstract.....	76
3.2 Introduction .....	77
3.3 Results.....	80
3.3.1 RabE Localizes to Sites of Polarized Secretion and Colocalizes with Myosin XI .....	80
3.3.2 RabE is Required for Normal Growth in <i>P. patens</i> , and <i>A. thaliana</i> RabE1c Rescues the <i>rabE</i> mutant .....	85
3.3.3 Myosin XI is a Conserved Effector of RabE, and <i>A. thaliana</i> Myosin Isoforms XI-K and XI-E Rescue Loss of Endogenous Myosin XI in <i>P. patens</i> .....	94
3.3.4 Myosin XI:RabE Interface Prediction .....	97
3.4 Discussion.....	107
3.5 Materials and Methods.....	111
3.5.1 Yeast Two-Hybrid Assay.....	111
3.5.2 Construction of Fluorescently Tagged RabE Moss Lines .....	112
3.5.3 Live-cell Confocal Imaging and Kymograph Analysis .....	112
3.5.4 Homology Modeling and Interface Prediction .....	113
3.5.5 CRISPR Knockout of RabE14 and RabE15.....	114
3.5.6 RNAi Growth Assays .....	115
3.5.7 Phylogenetic Analysis .....	116
3.5.8 Western Blot Analysis.....	117
3.5.9 Myosin XI Protoplast Expression .....	117

3.5.10 Myosin XI-CCT Purification.....	118
3.5.11 Statistical Analyses .....	119
Chapter 4 : Future Directions and Conclusions .....	125
4.1 Extension of the APTi System for Long-Term Imaging and Conditional Activation .....	126
4.2 Further Characterization of the Myosin XI:RabE Interaction .....	127
4.3 Conclusions .....	130
Chapter 5 : References .....	132

## List of Figures

Figure 1.1 Drawings depicting tip-growing cell types in mosses, liverworts, and flowering plants.....	5
Figure 1.2 A stylized perspective of three tip growing plant systems and a working model of exocytosis.....	12
Figure 1.3 Model depicting the apex of a generic tip-growing plant cell as a cycling center that coordinates exo- and endocytic activity.....	21
Figure 1.4 CRISPR\Cas9 mediated loss-of-function approaches.....	26
Figure 1.5 RNAi-mediated loss-of-function.....	31
Figure 2.1 Proof-of-principle and construction of APT-based RNAi (APTi) vectors to enable positive selection of actively silencing plants.....	44
Figure 2.2 Experimental strategy and timeline for the novel APTi system.....	47
Figure 2.3 The APTi system robustly silences the myosin XI family in <i>Physcomitrella patens</i> . .....	51
Figure 2.4 The APTi system reduces variability in observed mutant phenotype. ....	52
Figure 2.5 Determination of the linear range of used antibodies and long-term reproducibility of western blots using the APTi system.....	55
Figure 2.6 Phylogenetic tree of Lyk genes from <i>P. patens</i> and other selected plant and alga species. ....	58
Figure 2.7 Simultaneous silencing of the Lyk5 gene family with APTi abolishes chitin-induced calcium transients. ....	61
Figure 3.1 RabE co-localizes with myosin XI at sites of polarized exocytosis. ....	83
Figure 3.2 Subcellular Localization of RabE12 and Independent RabE14 Lines. ....	83
Figure 3.3 Sequence alignment of <i>P. patens</i> RabE and phylogenetic tree of RabE and RabE-like proteins.....	86
Figure 3.4 CRISPR/Cas9 knockout of RabE14 and RabE15. ....	88
Figure 3.5 The RabE GTPases are required for normal plant growth and the growth defect is rescued with RabE1c from <i>Arabidopsis thaliana</i> .....	90
Figure 3.6 RabE is required for normal polarized cell growth.....	92

Figure 3.7 Relative expression of the transcripts from the unedited RabE genes (E11, E12, E13). .....	94
Figure 3.8 <i>P. patens</i> RabE subfamily interacts with both moss myosin XI and <i>Arabidopsis</i> myosin XI-K isoform, and <i>A.t.</i> XI-K/E rescue loss of endogenous <i>P.p.</i> myosin XI. ....	96
Figure 3.9 RabE sequence conservation and prediction of Myosin XI-CBD and GTP-bound RabE14 binding interface. ....	98
Figure 3.10 Ramachandran plots and average RMSDs for myoXIa-CBD and RabE14 homology models. ....	99
Figure 3.11 Prediction of Myosin XI-CBD and GTP-bound RabE14 binding interface is robust. ....	102
Figure 3.12 Structure-guided mutagenesis of predicted Myosin XI-CBD:RabE14 binding interface reveals polarized growth mutants. ....	104
Figure 3.13 Detection of myosin XI protein abundance in Y2H experiments.....	104
Figure 3.14 Myosin XI cargo-binding domain mutants show varying levels of solubility. ....	106

## Acknowledgements

---

At the start, I would like to thank my sources of financial support: the National Science Foundation, the National Institutes of Health, and Worcester Polytechnic Institute. This support enabled my unfettered attention to the pursuit of my scientific goals, and I deeply appreciate their funding of basic research. As President Reagan said, “The remarkable thing is that although basic research does not begin with a particular practical goal, when you look at the results over the years, it ends up being one of the most practical things government does.” I hope there is a continued, if not increased, commitment to basic research from the United States and other countries around the world.

I would like to thank Glenn Gaudette and previous members of the Gaudette Lab in the BME department at WPI. Glenn gave me my first opportunity in research as a summer volunteer. Apparently, Glenn liked me enough to pay me the following summers during my undergraduate years! Upon graduating, Glenn hired me as his lab manager and research technician where I gained even more experience before starting my Ph.D. at WPI. My time in the Gaudette lab was truly transformative, and I cannot say how appreciative I am of Glenn’s previous and present support.

I am indebted to the past and present members of the Vidali Lab who assisted me either indirectly or directly. I would like to acknowledge Stephen Foley, whose enthusiastic demeanor and strong work ethic helped me spiritually and academically. Of course, I cannot overstate the importance of the encouragement, support, and laughs from Jeff Bibeau and Giulia Galotto. Also, I am grateful to the Munson Lab for introducing me to the world of biochemistry and the multitude of vegan food options. I am forever grateful to Mary Munson, who took me in and treated me as one of her own students during my advisor’s sabbatical year and continues to offer me support and guidance.

Most importantly, I would like to acknowledge and thank my advisor Luis Vidali. When I began the program at WPI, I didn’t choose a project, I chose a person. That decision was one of the best I have ever made, as I have genuinely enjoyed learning from and working for (and beside) Luis all these years. I look forward to seeing all the amazing science that is to come from the lab!

Lastly, I would like to thank my family. My parents, as always, have been incredibly supportive through both their words and dessert offerings. In retrospect, growing up as a child where I frequently visited my dad’s office and attended department parties at WPI, it was inevitable that I would end up at WPI in some capacity as an adult. I will never forget the words of my father’s colleague, Prof. Alexander Emanuel, a man who witnessed his world change overnight following the occupation of his native Romania by the former Soviet Union. He said to me as a boy and multiple times after, “Robert, study hard! People would kill to be in your boots. This is the life.”

And he was right. This is the life.

## Preface

---

I have adapted and expanded upon a recently published review article written by myself, Xiohang Cheng, Luis Vidali, and Magdalena Bezanilla for the content presented in Chapter 1.

**Orr, R.G.**, Cheng, X., Vidali, L., and Bezanilla, M., 2020. Orchestrating cell morphology from the inside out - using polarized cell expansion in plants as a model. *Current Opinion in Cell Biology* 62, 46-53.

Chapter 2 presents a collaborative and recently published manuscript. Luis Vidali and I conceived the study, as well as designed and supervised the research. Stephen J. Foley created the two base APTi constructs, with me providing supervision and creating the myoUTi construct. I developed and optimized the APTi high-throughput microscopy assay, as well as the western blot assay. Giulia Galotto and Boyuan Liu provided initial assistance during microscope optimization. Our colleagues in Madrid, Spain (Isidro Abreu and Manuel Gonzalez-Guerrero) with Luis Vidali created the GCaMP line used for the Lyk5 analysis. Catherine Sherman created the Lyk5-RNAi construct and performed experiments with my assistance, and analyzed the data with Luis Vidali's supervision. I wrote the manuscript and all authors approved the final manuscript.

**Orr, R.G.**, Foley, S.J., Sherman, C.A., Abreu, I., Galotto, G., Liu, B., Gonzalez-Guerrero, M. and Vidali, L., 2020. Robust survival-based RNAi of gene families using in tandem silencing of adenine phosphoribosyltransferase. *Plant Physiology*.

Chapter 3 presents a collaborate manuscript that has been peer-reviewed and currently under the status of 'accept subject to revision.' Fabienne Furt, Luis Vidali, Mary Munson, and I designed and supervised the research. Allison Butt and I performed the imaging of Figure 3.2b. Erin M. Agar performed the experiments of Figure 3.14a,b with Fabienne

Furt and Luis Vidali supervising. Figure 3.14c was performed by Jennifer M. Garbarino and Sarah E. Cabral, with supervision from Mary Munson, Michelle L. Dubuke, Fabienne Furt, and Luis Vidali. The experiments of Figure 3.12d,e were performed by Erin L. Warner and Fabienne Furt, and I reanalyzed and visualized the data. All other figures were the result of experimentation and analysis done by myself. I wrote the manuscript and all authors approved the final version.

**Orr, R.G.**, Furt, F., Warner, E.L., Agar, E.M., Garbarino, J.M., Cabral, S.E., Dubuke, M.L., Butt, A.M., Munson, M. and Vidali, L., 2020. RabE and its interaction with myosin XI are essential for cell polarization and growth. (Accept Subject to Revision) *New Phytologist*

## Abstract

---

Symmetry breaking events are indispensable to generate the diverse morphological structures observed across life. One consequence of a symmetry breaking event is polarized growth, the self-propagating and anisotropic expansion of a cell. Within the plant kingdom certain cells undergo an extreme variant of polarized growth, termed tip growth. In tip growth, a cell grows by intricately modulating the extensibility of the cell wall within a restricted area, thereby permitting precise turgor-driven expansion. This process is dependent upon polarized trafficking, specifically the coordinated and faithful delivery of secretory vesicles that contain polysaccharides and other components necessary to maintain tip growth. Unlike in opisthokonts, there is a severe gap within our mechanistic understanding of how plant cells self-organize and sustain polarized growth.

One of the leading causes contributing to this gap in the plant field is a lack of tools that addresses the abundance of gene isoforms, while facilitating functional studies. To fulfill this need, I developed a novel APT-based RNAi technology (APTi) in *Physcomitrella patens* that simultaneously improves upon the multiple limitations of current RNAi techniques. The APTi approach enables simultaneous and potent silencing of gene families, as evidenced by the myosin XI (a,b) and Lyk5 (a,b,c) gene families. The positive selection nature of APTi represents a fundamental improvement in RNAi technology and will contribute to the growing demand for technologies amenable to high-throughput phenotyping.

Despite substantial work uncovering many genes necessary for polarized growth in plants, few mechanistic details are known about how molecular motors, such as myosin XI, associate with their secretory cargo to support sustained directional growth and cell

division. In this work, I employed live-cell imaging, targeted gene knockouts, structural prediction, and a high-throughput RNAi assay to create the first characterization of loss of RabE in plants. I found that RabE and myosin XI are co-localized at sites of active exocytosis, and spatiotemporally coupled at the growing apex. Furthermore, RabE is required for polarized growth in *P. patens*, and the *P. patens rabE* and *myosinXI* mutants are rescued by *A. thaliana*'s RabE1c and myosin XI-K/E, respectively. I demonstrated that *P. patens* myosin XI and *A. thaliana* myosin XI-K interact with RabE14 of *P. patens*, and that specific perturbation of this interaction results in a loss of polarized growth. These results suggest the interaction between myosin XI and RabE is a conserved feature of polarized growth in plants, and perhaps originated from the last common eukaryotic ancestor.

# **Chapter 1 : Polarized Cell Growth in Plants and the Loss-of-Function Tools that Facilitate Our Understanding**

---

## 1.1 Introduction

Cells polarize in response to a myriad of extracellular cues. For example, in multicellular organisms, orientation within tissues is critical for proper tissue and organ function. Plant cells are encased by their extracellular matrix, and thus fixed within the plant body. Consequently, to respond to polarizing cues, plant cells alter their intracellular organization, often resulting in changes to the extracellular matrix that impacts cell and tissue morphology.

Polarity in plants can be discussed on several levels, ranging from orientation of aerial and underground tissues to individual cells as they divide within a tissue to generate structures such as stomata — pores in leaves driving gas exchange without which plants would not be able to utilize environmental carbon dioxide to build their body. Deciphering the molecular mechanisms controlling cell polarity within the context of a whole tissue can be a daunting task, as many cell non-autonomous factors contribute to polarity outcomes. However, all land plants have cell types that are highly polarized and protrude from the plant body by polarized cell expansion, or tip growth, responding more to environmental cues, rather than neighboring cellular cues. These cell types are found throughout the plant kingdom (Figure 1.1).

## Tip Growing Cells

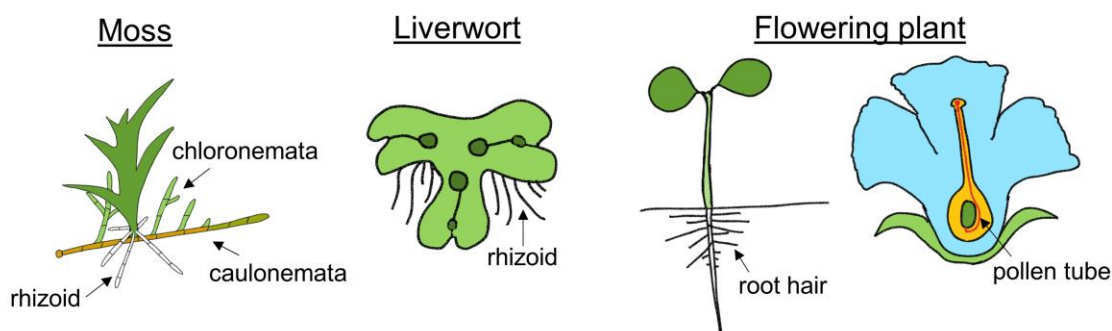


**Figure 1.1** Drawings depicting tip-growing cell types in mosses, liverworts, and flowering plants.

In plants, the products of meiosis can replicate mitotically and generate distinct tissues. The number of divisions and kinds of tissues generated vary throughout the plant kingdom. In early diverging land plants, such as mosses and liverworts, the majority of tissues are haploid having derived from these mitotic divisions. In contrast, flowering plants only undergo a few mitotic divisions after meiosis generating the ovule and pollen. Thus, most of flowering plant tissues develop from a fertilized embryo and are diploid. Mosses have three distinct haploid tip-growing cell types: chloronemata, caulonemata, and rhizoids (Figure 1.1). All three are multicellular. Chloronemal cells are the first to emerge from the spore and have transverse cell plates. Caulonemal cells develop from chloronemal cells and have oblique cell plates. Together, these two cell types comprise the branching filamentous tissue named protonemata, the juvenile tissue of moss that colonize and establish the plant. The adult tissues develop from protonemata and are depicted as a leaf-like structure in the drawing (Figure 1.1). Protruding from the base of the adult tissue are tip-growing rhizoids, which in general do not branch and serve to

anchor the adult tissues in the soil. The moss *P. patens* is particularly amenable to genetic manipulation, regenerates quickly, is easy to propagate in the lab, and is especially suited for live-cell imaging. As a result, *P. patens* has become a powerful model for studying tip growth. Liverworts germinate from a spore into a thallus that is anchored into the soil by single-celled rhizoids. The recent sequencing of the *Marchantia polymorpha* genome (Bowman et al., 2017) together with rapid advances in genome editing (Ishizaki et al., 2016), has propelled this system for the study of evolutionary development questions in plants. While relatively fewer studies have focused on rhizoid development (Honkanen et al., 2016; Otani et al., 2018), *M. polymorpha* promises to be an excellent comparative system to study tip growth.

Vascular plants have root hairs, which are diploid, single-cell protrusions that emerge from the root epidermis. Additionally, vascular plants can manifest the haploid pollen tube, which germinates from a pollen grain that has landed on a receptive stigma (Figure 1.1) in the case of flowering plants or cones for gymnosperms. Several different plant species have been used to study root hairs and pollen tubes, including *A. thaliana*, lily, tobacco, and rice. However, as more molecular tools emerge for diverse plant species, tip growth studies will expand to a larger number of species and capture the diversity across the plant kingdom.

Flowering plant pollen tubes, which are by far the most studied tip-growing cell type, have a short life-span, growing for at most a day. Furthermore, their signaling system solely responds to unique cues emitted from the ovule in the flower. In contrast, the other common model systems, root hairs and moss caulonemal cells, live relatively longer, ranging from weeks to months and both cell types respond to multiple extracellular

signals, such as nutrient and water availability, gravity, and light. Thus, plants provide a unique system to study the evolution of both the initiation and maintenance of cell polarity in cell types that are separated by hundreds of millions of years of evolution, but respond to similar extracellular cues (root hairs versus rhizoids/caulonemata), and within a single plant where cells emerge in response to distinct extracellular cues (root hairs versus pollen tubes).

In plants, tip growth results from the coupling of precise cell wall remodeling at a particular site and turgor-driven cell expansion such that cells grow only at their apex. The apical domain, therefore, is a region of extensive membrane remodeling requiring exocytic delivery of vesicles carrying extensible cell wall material and endocytic retrieval of excess membranes and signaling components marking the apical domain. Here, I discuss recent advances linking the cytoskeleton and vesicle trafficking to directional persistence during growth with possible links to membrane remodeling. I particularly emphasize the moss *Physcomitrella patens* as a model for plant tip growth, and highlight current loss-of-function techniques that are indispensable for a comprehensive understanding of tip growth.

## **1.2 *Physcomitrella/Physcomitrium patens*: A Versatile Plant Model for Cellular Polarized Growth**

The moss *P. patens*, like all land plants, displays a stereotyped alternation of generations characterized by the haploid gametophyte and the diploid sporophyte. The haploid gametophyte stage dominates the life cycle of bryophytes, which consists of mosses, hornworts, and liverworts. The precise taxonomic and phylogenetic organization of extant embryophytes (land plants) is an area of constant flux (Puttick et al., 2018; Delaux et al.,

2019). As a result, recent phylogenetic analyses strongly support that the previously named *Physcomitrella patens* derives from the *Physcomitrium* lineage and should be called *Physcomitrium patens* (Liu et al., 2012; Beike et al., 2014; Medina et al., 2018; Medina et al., 2019). However, as most of the manuscripts contained herein were prepared before the recent call for name change (Rensing et al., 2020), *Physcomitrella patens* is used to maintain internal consistency.

Following the isolation of the Gransden *P. patens* ecotype in 1962, heroic efforts demonstrating the genetic tractability of *P. patens* (Schaefer and Zryd, 1997) and sequencing of the genome (Rensing et al., 2008) firmly established *P. patens* as an indispensable resource for investigating the evolutionary origins of land colonization by plants. In recognition of its importance, *P. patens* constitutes one of the U.S. Department of Energy's flagship genomes (<https://jgi.doe.gov/our-science/science-programs/plant-genomics/plant-flagship-genomes/>). At present, there exists a host of online and experimental resources and tools, reviewed in (Rensing et al., 2020), to facilitate both evo-devo and cell biology studies.

*P. patens* contains many salient features that make it an excellent model for investigating tip growth (Vidali and Bezanilla, 2012), such as its amenability to targeted genetic manipulation and relatively simple body plan (Figure 1.1). Following spore germination, protoplast regeneration, or mechanical wounding, tip cells emerge and radially proliferate thereby establishing a near two-dimensional filamentous network. The juvenile tissue can be asexually propagated *ad infinitum* with mechanical homogenization, or the tissue can be treated with an enzymatic cocktail to digest the cell walls, thereby isolating individual protoplasts. Exogenous DNA is introduced to

protoplasts with a simple PEG-mediated procedure (Schaefer et al., 1991; Liu and Vidali, 2011), which can result in either transient expression or stable integration of a given sequence. Exploiting the haploid dominance and remarkable level of homology directed repair (HDR) native to *P. patens* allows straightforward mutagenesis or fusions of genes to functional tags (fluorescent proteins, affinity tags) at the endogenous locus. A more detailed discussion of techniques to generate loss-of-function mutants is found below. Importantly, regeneration of a single transformed protoplast will result in an isogenic population of tip growing cells, and these cells can complete the sexual life cycle. At the juvenile stage, all growing cells are undergoing tip growth and the filamentous tissue is only one cell thick. This anatomy is excellent for high-resolution live-cell microscopy, and when coupled with facile gene tagging, protein dynamics can be observed at their native concentrations. Furthermore, *P. patens* can be cultured in microfluidic devices, which enables both long-term and single particle imaging (Bascom et al., 2016; Kozgunova and Goshima, 2019; Sakai et al., 2019).

The aforementioned characteristics of *P. patens* unquestionably establish this moss as an exceptional species to work with, but not necessarily as a good model for tip growth. Fortunately, here I discuss recent studies investigating the cytoskeleton, associated motor proteins, and vesicle trafficking among others that have demonstrated an exceptional degree of functional conservation, while noting some important differences.

### **1.3 Cytoskeletal Coordination**

Despite differences in ultrastructural organization (Figure 1.2), all tip-growing systems are thought to employ the actin cytoskeleton to spatially regulate membrane trafficking to

maintain unidirectional expansion. Our antiquated understanding of actin's function in tip growth was based upon the simple definition of active transport whereby molecular motors transport cargo to exocytic sites along established tracks to overcome diffusion limitations. However, F-actin is not a passive track, but rather is a dynamic entity that undergoes rapid, stochastic reorganization (Szymanski and Staiger, 2018). Furthermore, the most dynamic F-actin structures that are required for tip growth (Figure 1.1), such as the cortical fringe in pollen and the intense F-actin spot in caulonemal cells, demonstrate a level of organization that defies point-to-point transport. Recent studies in *Physcomitrella patens* demonstrated that the F-actin spot predicts the site of expansion (Wu and Bezanilla, 2018) and explored possible explanations of F-actin's function, discovering that while F-actin directionally transports vesicles, diffusion alone is theoretically sufficient for growth, albeit at a fraction of the normal rate (Bibeau et al., 2018b). However, depletion of F-actin results in sudden growth arrest, implicating that F-actin actively clusters/focuses membranes, particularly vesicles, in a small area at the growing tip (Qu et al., 2017; Bibeau et al., 2018b).

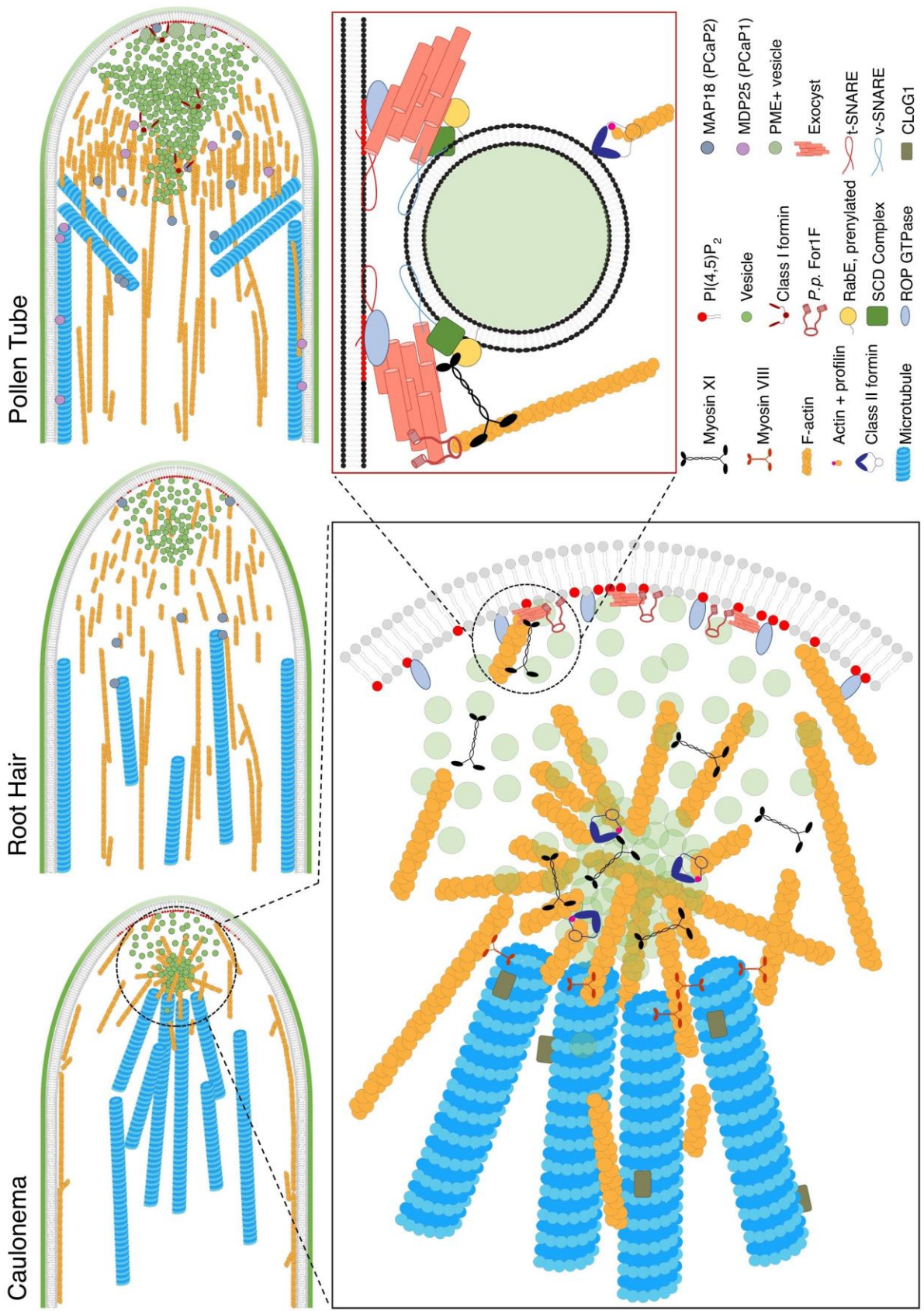


**Figure 1.2** A stylized perspective of three tip growing plant systems and a working model of exocytosis (red box). Based on published data as summarized in the text, all systems display an apically localized and interdependent pool of vesicles, myosins, and formins. This polarized organization is maintained by a dynamic F-actin network that is spatially stabilized by microtubules. In addition to a polarized cytoplasm, the apical plasma membrane is enriched in PI(4,5)P<sub>2</sub>, ROP GTPases, and subunits of the exocyst that facilitate actin polymerization and exocytosis. Our exocytosis model is conceptually similar to the process found in yeast. Tip-localized PI(4,5)P<sub>2</sub> and active ROPs capture the exocyst at discrete membrane sites, thereby functionally restricting the exocyst. Additionally, given the expansion of exocyst subunits in plants, it is likely different subunit composition could regulate the exocyst. The exocyst then coordinates with the secretory vesicle through vesicle-localized effectors, such as myosin XI, Rab GTPases, and their regulators, such as the putative GEF, the SCD complex

The three most well-studied plant tip-growing cells types share one fundamental characteristic at the growing apex: fine, likely single, actin filaments coincident with a dynamic cloud of vesicles (Figure 1.2). Importantly, this organization appears interdependent, suggesting an underlying mechanism that generates and couples the polarized vesicle distribution with F-actin. In *P. patens*, the actin motor myosin XI and secretory vesicles predict the arrival of F-actin at the cell apex; and ectopically generated vesicle clusters also contain myosin XI and precede F-actin formation in the shank region of a tip cell (Furt et al., 2013). Intriguingly, the class II formin, which also localizes with the apical actin accumulation, also precedes F-actin accumulation in similar ectopic clusters (van Gisbergen et al., 2012) and at the cell apex (Wu and Bezanilla, 2018). Recent work investigating class I formins in the pollen tube converged upon a direct association between tip-localized vesicles, F-actin nucleators, and the emergence of actin filaments (Li et al., 2017; Lan et al., 2018). As myosin XI is a relatively low-abundance protein in *P. patens*, we speculate the mechanism described above in concert with homotypic interactions between vesicle-localized Rabs (Segawa et al., 2019) and other unknown

processes could promote vesicle clustering. This may promote a liquid–liquid phase separation and the characteristic vesicle/myosin/actin cluster that drives tip growth. This hypothesis is inspired by the liquid behavior of cross-linked actin (Weirich et al., 2017) and actin’s involvement in biomolecular condensates (Case et al., 2019), as well as the recently proposed diffusion capture paradigm (Bracha et al., 2018). The formation of biomolecular condensates results in a membraneless and fluid compartment that biases the formation of transient interactions (Hyman et al., 2014), as is likely the case with myosin XI and vesicles (Bibeau et al., 2020). Exploring the possibility that phase separation of vesicles and vesicle-associated proteins is a necessary emergent event for tip growth offers a fascinating avenue of future research.

Traditionally, the study of tip growth in plants disproportionately focused on the actin cytoskeletal network as it is indispensable for tip growth. However, recent studies demonstrate that microtubules are critical for growth directionality and implicate microtubules and F-actin as an increasingly interconnected system for maintenance of polarity. In *P. patens* microtubules function in polarity fidelity by spatially restricting actin polymerization and vesicle clustering (Wu and Bezanilla, 2018; Yamada and Goshima, 2018) (Figure 1.2). One possible mechanism that could explain the observed restrictive effect of microtubules on F-actin is through direct microtubule-to-actin interactions. Microtubule and actin cross talk appears to be a consistent feature of tip-growing systems given direct observations in multiple cell types. In *P. patens*, myosin VIII interacts with microtubules and actin to promote persistent polarized growth (Wu and Bezanilla, 2018) (Figure 2). Recent evidence using a conditional forward genetics screen in moss, identified CLoG1, a novel microtubule depolymerizing end tracking protein, which is

involved in tip growth and localizes to zones of microtubule-F-actin overlaps at the tip (Ding et al., 2018) (Figure 1.2). In angiosperms, the microtubule-associated proteins MDP25/PCaP1 and MAP18/PCaP2 associate with actin and demonstrate calcium-dependent severing activity (Zhu et al., 2013; Qin et al., 2014) (Figure 1.2). In addition to direct crosslinking of microtubules to actin, studies have revealed interactions between microtubules and F-actin nucleators, such as formins (Deeks et al., 2010; Li et al., 2010; Zhang et al., 2011; Wang et al., 2013) and a subunit of the ARP2/3 complex (Havelkova et al., 2015). This raises the intriguing possibility of microtubules orchestrating F-actin organization through assisting the clustering of vesicles rich in actin nucleators.

#### **1.4 Exocytosis**

The rapidly expanding cell requires faithful intracellular trafficking of secretory vesicles containing cargo that facilitates the extension of the cell wall. Our mechanistic understanding of polarized trafficking and exocytosis is surprisingly lacking, which we suggest is a consequence of insufficient tools to mark and observe active areas of exocytosis. A quantification method, based on relative levels of exocytosis, corrected for endocytosis, is a welcome development for this problem (Luo et al., 2016).

As a first approximation, by analyzing the localization and loss of function phenotypes of various exocyst subunits, which is a tethering complex for exocytic vesicles, there is evidence in caulonemata, root hairs, and some pollen tubes that exocytosis is enriched at the apical plasma membrane (Wen et al., 2005; Synek et al., 2006; Bloch et al., 2016; van Gisbergen et al., 2018b; Tang et al., 2019) (Figure 1.2). We know from yeast and mammalian studies that the exocyst serves as a multivalent platform orchestrating exocytosis through interactions of plasma membrane and vesicle-localized

effectors, such as the molecular motor myosin V and the Rab GTPase, Sec4 (Lepore et al., 2018). An emerging hypothesis suggests that in plants myosin XI associates with its vesicular cargo through an interaction with a Rab GTPase on the vesicle membrane and then with the exocyst for vesicle tethering at the plasma membrane (Figure 1.2). This transport model is supported by preliminary evidence detailed in this dissertation that demonstrates a myosin XI interaction with the RabE subfamily, which is homologous with the yeast Rab Sec4. Furthermore, biochemical and proteomic data places RabE, its putative GEF (Figure 1.2, SCD complex), and the exocyst complex at sites of polarized exocytosis (Mayers et al., 2017a). The remarkable degree of similarity between two evolutionarily distant clades should empower us to not only use insights from yeast and mammals to inform our future experiments but opens the possibility that other fundamental findings in plants are shared between all polarized growth cell types.

Despite these advancements, it is likely that the seemingly homogenous vesicle cluster we observe at the mesoscale is an amalgamation of different vesicle subpopulations that are decorated by a unique complement of proteins and internal cargo. This is evidenced by a variety of unconventional secretion pathways (Wang et al., 2018), such as pectin methylesterase bypassing the TGN in pollen tubes (Wang et al., 2016). As a result, while the highest vesicle flux may occur at the tip, exocytosis occurs across the entire surface of the cell, as is observed for the cellulose synthase complex (Tran et al., 2018). Thus, identifying cargo that is specifically secreted at sites of polarized expansion will improve our ability to confidently detect specific exocytic events that regulate polarized growth.

### 1.4.1 Rab GTPases

The cytoplasm of a cell is a densely packed and dynamic environment (Dix and Verkman, 2008; Zhou et al., 2008; Goodsell et al., 2020). To an external observer, the molecular dynamics within the cell are almost chaotic. Nevertheless, the cell maintains an exquisite level of control over various cellular process, especially with respect to polarized trafficking. The cell attains robust and faithful transport of endomembrane vesicles by unique identification of endomembrane compartments. Although multiple proteins and lipids in concert impart membrane specificity, Rab GTPases are essential to maintain the fidelity of the endomembrane system (Stenmark, 2009; Pfeffer, 2013).

Importantly, Rab GTPases have expanded concomitantly with the evolved complexity of the eukaryotic cell, with 11 in yeast, over 60 in humans, and over 50 in *A. thaliana* (Pereira-Leal and Seabra, 2001; Rutherford and Moore, 2002). Rabs undergo a characteristic, dynamic structural rearrangement depending on the bound nucleotide—GTP-bound Rabs are typically associated with the membrane and are “active,” whereas GDP-bound Rabs are “inactive” and are preferentially located within the cytosol (Mizuno-Yamasaki et al., 2012). The dynamic on/off cycling of Rab activity is primarily regulated by two classes of proteins: guanine exchange factors (GEFs), which recruit Rabs to the membrane and activate Rabs by facilitating the dissociation of bound GDP; GTPase-activating proteins (GAPs), which inactivate Rabs by enhancing the inherently slow hydrolysis of GTP to GDP. This structural plasticity of Rabs allows precise discrimination of binding partners, with Rab effectors typically displaying preferential binding to the active, GTP-bound, form of the Rab (Khan and Menetrey, 2013). In the context of polarized growth, certain Rabs are required for proper vesicle trafficking and exocytosis

across eukaryotes (Zhen and Stenmark, 2015). Specifically, there is evidence in yeast and human supporting the idea of a Rab transport cascade, whereby transport of secretory vesicles is dictated by the sequential recruitment of Rabs and their cognate GEFs (Jin et al., 2011; Mizuno-Yamasaki et al., 2012). Additionally, these Rabs, such as Sec4 in yeast, interact with the molecular motor myosin V and the exocyst, directly implicating Rabs in the polarized transport pathway (Lepore et al., 2018; Pylypenko et al., 2018). In plants, Rabs have also been implicated in various cellular processes, including post-golgi trafficking (Elliott et al., 2020). Unlike in yeast and mammalian systems, the plant Rab field currently lacks mechanistic insights into how Rabs and their putative effectors coordinate polarized trafficking and exocytosis.

### **1.5 The Apical Plasma Membrane**

Among proteins that are enriched at the apical plasma membrane, ROP GTPases are critical signaling molecules. In *P. patens*, as in other plants, ROPs are essential for polarized growth (Burkart et al., 2015; Feiguelman et al., 2018). Systematic silencing of all the ROP regulators in moss revealed that of the GTPase activating proteins (GAPs) the ROPGAP family, not the REN family, are critical for polarized growth. Silencing of the guanine nucleotide exchange factors (GEFs) demonstrated that the SPIKE type of GEFs, known activators of ROP activity (Basu et al., 2008), were more important for cell polarization than the ROPGEFs. Moreover, the guanine dissociation inhibitors (GDIs), which localized throughout the cytoplasm, were also essential for cell polarity (Bascom et al., 2019a). Using both endogenous knock-in of sequences encoding for fluorescent proteins coupled with inducible expression strategies, another recent study revealed apical localization of PpROP1 and PpROPGEF4, with PpROPGEF4 populating a more

confined region at the extreme tip (Le Bail et al., 2019). However, validating function of the fluorescent fusion proteins can be challenging, particularly for ROP, for which genomic alterations including fusions to fluorescent proteins were unable to support normal polarized growth in the absence of all other endogenous ROPs (Burkart et al., 2015). Thus, it will be critical to identify additional polarity markers amenable to tagging and live-cell imaging.

Recent publications are illuminating mechanistic details of ROP polarization. Denninger and collaborators demonstrated that successive polarization of distinct ROP-GEFs and subsequent ROP recruitment promotes root hair initiation and outgrowth (Denninger et al., 2019). Furthermore, in root epidermal cells ROP6 partitions to discrete nanodomains through an interaction between ROP's intrinsic polybasic region and the anionic phospholipid phosphatidylserine (Platre et al., 2019). It remains an open question how ROP-GEFs, anion phospholipids, and other signals are integrated to drive the initial polarization event. Recent work in root hairs has also discovered that the microtubule-actin cross-linking protein MAP18 preferentially interacts with the GDP-bound state of ROP2 (Kang et al., 2017). This interaction, which may occur at the cytoskeleton, effectively promotes ROP activity by shielding ROP from extraction by the ROP-GDI, providing an exciting link between the cytoskeleton and ROP activity.

## **1.6 Endocytosis**

Retrieval of membrane from the apex via endocytosis also plays a fundamental role in polarizing cells (Samaj et al., 2005). In root hairs endosome motility and FM4-64 uptake were both impaired in the absence of actin (Ovecka et al., 2005; Voigt et al., 2005). Molecular evidence linking endocytosis to polarized growth was provided by studies of

the T-PLATE endocytic adaptor complex. T-PLATE was found to be enriched at the emerging tip of germinating pollen in *Arabidopsis*. Critically, mutations of subunits in the T-PLATE complex impair pollen tube germination in *Arabidopsis*, resulting in accumulation of callose at ectopic sites in the pollen grain (van Damme et al., 2006). More recently, inhibition of clathrin-dependent endocytosis in pollen tubes was shown to impair tip growth (Zhao et al., 2010). Thus, with impaired endocytosis, delivery of wall material is deregulated, suggesting that endocytosis contributes to regulating and or establishing the site of polarized growth during pollen tube germination and growth.

However, evidence of direct molecular links between endocytosis, the cytoskeleton and tip growth is surprisingly lacking. Of note, a recent study discovered that the Endocytosis Adaptor of Pollen Tube, EAP1, specifically binds to REN4, which is a GAP for the ROP GTPase. EAP1 participates in clathrin-mediated endocytosis and is involved in the active removal of REN4 from the cell apex (Li et al., 2018). As GAPs, REN proteins activate the intrinsic GTPase activity of ROPs, converting them to a GDP-bound state, which is inactive for cellular signaling. Thus, RENs could limit ROP activity to particular membrane domains (Feiguelman et al., 2018). In particular loss of REN4 impairs pollen tube directionality, implicating that REN4 works to control a uniform site of polarized expansion (Li et al., 2018). Interestingly, silencing RENs did not alter tip growth in moss caulonemata (Bascom et al., 2019a). While the exact family of GAP is not conserved between pollen tubes and moss, proteins with similar functions still impact cell polarity. Nevertheless, a physical connection between a ROP regulator and endocytosis supports the idea that endocytosis actively ensures that the apical plasma membrane is a distinct membrane domain. Furthermore, based on the localization of EAP1, this leads

to a model where endocytosis occurs at the collar region in pollen tubes (Li et al., 2018), which coincides with the highly dynamic actin fringe. It remains to be determined where endocytosis occurs in other tip-growing cells where the highly dynamic actin resides closer to the apical plasma membrane.

### **1.7 Outlook and Insights from Other Tip Growing Systems**

There are striking parallels between tip growth in plant cells and in filamentous fungi. For example, in *Aspergillus nidulans*, a dynamic cluster of membranes and actin forms near the cell apex (Riquelme et al., 2018). Many of the same classes of molecules that are required in plants are also required in fungi (Takeshita, 2016; Riquelme et al., 2018). Based on elegant studies, a current model posits that chitin synthase B, a cell wall-modifying enzyme essential for tip growth, is recycled from the apical plasma membrane to the trans Golgi network (TGN) via endosomes, with endocytosis of chitin synthase-dependent on actin. From the TGN, chitin synthase then gets rapidly exocytosed to the plasma membrane (Martzoukou et al., 2017; Hernandez-Gonzalez et al., 2018). Even though tip growth likely evolved independently in plants and fungi, the striking similarities may help to inform studies in both systems.

Combining knowledge from both fungi and plants, we hypothesize that the apex of the cell is a cycling center for endosomes and the TGN, and that dynamic actin is central in coordinating endocytosis and exocytosis at the expanding tip (Figure 1.3).



To test this, it will be essential to determine how exocytic cargo is sorted before reaching the apical domain. Thus, it is a priority to identify and image functional cargos that are specifically delivered to the tip (Figure 1.3) analogous to chitin synthase from filamentous fungi. Future work building upon the discovery of the physical link between ROP regulators and endocytosis (Li et al., 2018) (Figure 1.3) in additional plant cell types will provide the foundation for analyzing the dynamics and potential interdependence between endocytosis and cell polarity. Ultimately, determining the temporal and spatial polarization of exocytic, endocytic, and cytoskeletal factors during tip growth initiation will help to establish whether exocytosis, endocytosis, and/or the cytoskeleton generates the polarity cue. Then integrating cytoskeletal interactions and identifying molecular linkages that coordinate membrane trafficking will provide testable models for maintenance of polarized growth via possible feedback tying membrane trafficking and cytoskeletal organization.

### **1.8 Directed Loss-of-Function Approaches in Plant Functional Genomics**

To begin to understand complex traits, such as plant growth, researchers typically adopt a reductionist perspective. Although inherently flawed, reductionism provides an intuitive framework where one can systematically identify and remove all the parts thought to compose a given process. The process of identifying the necessary parts, named forward genetics, represents an invaluable and unbiased approach to enumerate genes involved in a fundamental biological process by random mutagenesis (UV light, chemical, transposable elements, etc.). However, a biological screen is a noisy process and requires validation of the accumulated gene hits. To this end, reverse genetics allows precise perturbation of genes, which enables confident inference of a gene's function.

Reverse genetics can be thought of as “hypothesis testing” experiments, which are a necessary complement to forward genetic, “hypothesis generating” experiments. Here, I describe the most common approaches for generating targeted loss-of-function mutants, using the moss *P. patens* and the process of tip growth as a case study.

### **1.8.1 Homology Directed Repair**

Before the advent of programmable nucleases, a large factor contributing to the prominence of a given model organism was its intrinsic amenability to reverse genetics. Specifically, the capacity of an organism to integrate DNA via the homology directed repair (HDR) pathway allows for precise gene targeting. Unlike bacteria and yeast that display high rates of HDR-mediated gene targeting, multicellular organisms typically resolve DNA lesions through alternative, error-prone mechanisms (Figure 1.4) (Ceccaldi et al., 2016). Notable exceptions exist, such as mouse embryonic stem cells (Doetschman et al., 1987; Thomas and Capecchi, 1987) and the moss *P. patens*.

Unlike *P. patens*, vascular plants, specifically agricultural crops, are notoriously recalcitrant to genetic engineering because of two predominant factors: low transformation and regeneration efficiency, and low rate of HDR (Lee et al., 1990; Offringa et al., 1990; Halfter et al., 1992; Kempin et al., 1997; Puchta and Fauser, 2013). Exogenous DNA is efficiently and easily introduced into *P. patens* via PEG-mediated transformation (Schaefer et al., 1991; Liu and Vidali, 2011). If the transformed DNA possesses sufficient sequence homology to an internal locus, rates of HDR-mediated integration rival that of those observed in yeast and clearly overshadow any other plant model organism (Schaefer and Zryd, 1997; Kamisugi et al., 2005). In practice, precise loss-of-function mutants are generated by flanking an antibiotic resistance gene with ~1kb

of identical sequence upstream and downstream to the gene you wish to disrupt. With this strategy, the endogenous gene is ablated and is easily selected for using the inserted resistance gene (Strepp et al., 1998). Additionally, this strategy can be multiplexed to generate higher order mutants and has been successfully employed in *P. patens* to generate a quintuple knockout of the myosin VIII family (Wu et al., 2011a). However, different antibiotic resistance genes must be used or the preexisting resistance gene must be excised, such as with Cre-Lox recombination. The mechanism(s) by which *P. patens* achieves high rates of HDR is an area of active research (Schaefer et al., 2010; Wiedemann et al., 2018; Mara et al., 2019)—understanding this process will hopefully enable researchers to bias the internal equilibrium of DNA repair towards HDR, thereby converting previously intractable organisms to more malleable genetic engineering platforms.

### **1.8.2 CRISPR/Cas**

Despite the relatively high rate of HDR in *P. patens*, creation of multi-gene knockouts using the classic HDR method is still a cumbersome process that typically requires multiple transformations. Additionally, the HDR-mediated gene replacement strategy described above results in a complete null mutant, which could be undesirable. For example, a null mutant for a pleiotropic gene will have broad phenotypic consequences, or might be lethal. Programmable nucleases allow targeted disruption of a DNA sequence, whereby a specific domain's function can be lost independent of other attributes of the gene product resulting in a hypomorph mutant. Therefore, the observed phenotype is restricted to the specific perturbation, resulting in more meaningful interpretations.

The discovery and domestication of the prokaryotic adaptive immune system, named clustered regularly interspaced short palindromic repeats (CRISPR) and the CRISPR-associated proteins (Cas), revolutionized gene editing (Jinek et al., 2012; Doudna and Charpentier, 2014). The ease-of-use and inexpensive nature of CRISPR-Cas ensured its rapid adoption and quickly supplanted previous methods of targeted DNA double-stranded breaks (DSBs), such as zinc-finger nucleases and transcription activator-like effector nucleases (TALENs). To date, the type II CRISPR/Cas9 system from *Streptococcus pyogenes* is the most popular CRISPR-based editing tool and only requires expression of a single guide RNA (sgRNA) and the Cas9 endonuclease. Successful introduction of a targeted DSB using CRISPR/Cas9 requires that the genomic locus to be targeted contains a canonical protospacer adjacent motif (PAM), which corresponds to the Cas enzyme used (Jinek et al., 2012). Cas9 from *S. pyogenes* utilizes the PAM sequence 'NGG'; therefore, targeting Cas9 to a specific genomic locus necessitates co-expression of Cas9 and a sgRNA containing a 20-nucleotide sequence complementary to the gene target immediately adjacent to a PAM. The sgRNA is a modular unit, with the 5' "spacer" sequence corresponding to the user-defined 20-nucleotide target sequence, and the remaining "scaffold" sequence imparting structure for engagement with Cas9. Loading of Cas9 with the sgRNA followed by target recognition via Watson-Crick base pairing between the sgRNA spacer and genomic target results in a structural rearrangement that promotes the dual catalytic activity of Cas9 (Sternberg et al., 2015) (Figure 1.4).

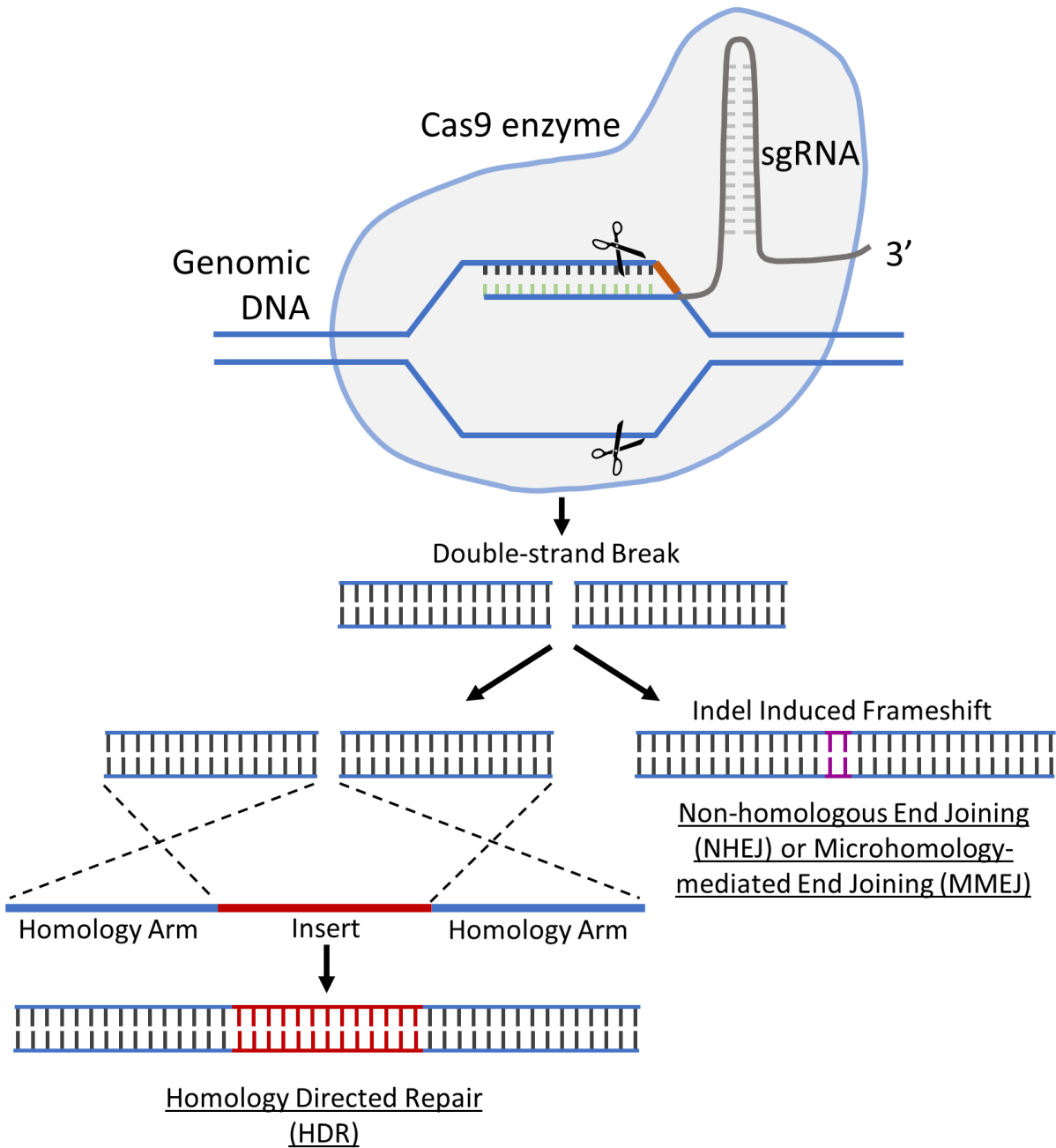


**Figure 1.4** CRISPR/Cas9 mediated loss-of-function approaches. Upon Cas9 loading of the gRNA, the Cas9:gRNA complex base-pairs with the target DNA via the spacer region (green), which is immediately adjacent to the PAM (orange), resulting in a DSB. The DSB can be resolved in multiple ways: NHEJ; MMEJ; or HDR..

CRISPR/Cas technology has been successfully implemented in plants, ranging from maize to moss, to generate loss-of-function alleles (Chen et al., 2019; Zhang et al., 2019). The output of a CRISPR experiment is entirely dependent upon the user-designed sgRNA input. Previous work, predominantly in mammalian systems, has empirically guided algorithms that assist in determining optimal sgRNA sequences to maximize on-target cleavage and minimize off-target effects (Hanna and Doench, 2020). Each of these tools differ, so the best choice of tool is dependent on the specific experimental objectives. Typically, a reverse genetic loss-of-function experiment with CRISPR will use either one or two sgRNAs per gene. The one sgRNA strategy minimizes reagents, thereby enabling multiple genes to be targeted by different sgRNAs in a single transformation (Lopez-Obando et al., 2016). If the sgRNA is designed to disrupt a naturally occurring restriction site, successful editing events can be quickly determined. However, the detection of an editing event is not sufficient to determine the loss of gene function. Use of a downstream start site or alternative splicing could result in a fully or partially functional protein. The two sgRNA strategy allows for large deletions, which increases the probability of recovering a loss-of-function mutant (Dang et al., 2015). Nevertheless, the resultant repaired DNA lesion is not an entirely predictable outcome, but it appears *P. patens* favors microhomology end-joining (MMEJ) (Collonnier et al., 2017b). As a result, multiple independent and distinct alleles can be recovered from one transformation with a single sgRNA.

Directed double-strand breaks of DNA stunningly enhance the incidence of homologous recombination (Puchta et al., 1993; Choulika et al., 1995; Smih et al., 1995). However, even with enhanced prevalence of HDR through CRISPR-induced DSBs, the

observed efficiency of HDR in most plant species fails to exceed a few percent (Shan et al., 2014; Cermak et al., 2015; Collonnier et al., 2017a; Rozov et al., 2019). The moss *P. patens*, with its already high rate of HDR, makes an excellent partner with CRISPR/Cas to generate precise mutants. Instead of relying on the seemingly stochastic internal repair mechanisms to resolve the induced DSB, a homologous DNA template can be co-transformed with the CRISPR machinery to drive HDR (Figure 1.4). The homology template could contain a series of stop codons to ensure gene knockout (Mallett et al., 2019), or an explicit mutation to render the resulting protein product catalytically inactive (Yi and Goshima, 2020).

Despite the observed fidelity of CRISPR-HDR gene editing in *P. patens*, anytime DNA DSBs are introduced the possibility of unintended mutations exists. These unintended mutations result from either off-target effects, which can be minimized through stringent sgRNA selection and/or modification of Cas itself (Ran et al., 2013), or unexpected and complex rearrangements at the target site (Kosicki et al., 2018; Lee and Kim, 2018). Fortunately, advances in CRISPR/Cas technologies has resulted in ways to create loss-of-function mutants without DNA DSBs. These strategies follow the same principle: a catalytically inactive Cas (dCas) is fused to functional domain, such as the KRAB domain for gene transcriptional repression (Gilbert et al., 2013) or a cytidine/adenine deaminase for precise base editing (Komor et al., 2016; Nishida et al., 2016; Gaudelli et al., 2017). CRISPR-interference (CRISPRi) is less popular in plants, presumably a consequence of the robustness of, and preexisting reagents/methods for, traditional RNAi (discussed below). Both cytidine (Shimatani et al., 2017; Zong et al., 2017; Qin et al., 2020; Veillet et al., 2020) and adenine (Kang et al., 2018; Yan et al.,

2018) base editors have been utilized in plants to create loss and gain of function mutations. Although the CRISPR/Cas toolbox has greatly expanded, the applicability is limited by PAM requirements, efficacy, and amenability of the target organism to transformation, regeneration, and HDR. Recent pioneering work in human cells vastly enhanced the power of CRISPR by enabling multiple and simultaneous precise nucleotide changes (Anzalone et al., 2019), as well as nearly eliminating the PAM requirement of Cas9 (Chatterjee et al., 2020; Walton et al., 2020). It will be fascinating to observe how these technologies transform gene editing in plant research in the coming years.

### **1.8.3 RNA Interference**

The importance of CRISPR/Cas technology in generating targeted gene knockouts cannot be overstated, as it has single-handedly propelled molecular biology forward into a new era. However, the most popular methodology of CRISPR/Cas9 is constrained in several fundamental ways that limits its scope, particularly with respect to agricultural species. This is a consequence of many essential crops containing multiple copies of a given gene because of polyploidization events (Bowers et al., 2003), such as the indispensable allotetraploid cotton *Gossypium hirsutum* (Paterson et al., 2012; Zhang et al., 2015). Therefore, DNA-based technologies become increasingly inefficient with increased copy number. Fortunately, technologies exist that exert their action downstream of DNA (post-transcriptionally), such as RNA interference (RNAi) acting upon messenger RNA (mRNA).

RNA interference is a conserved eukaryotic process whereby approximately 20-30 nucleotides of double-stranded RNA (dsRNA) results in downregulation, termed “silencing,” of any gene that contains sequence complementary to the dsRNA (Wilson and Doudna, 2013). Since initial observations of gene silencing phenomena, termed “co-suppression” in plants (Napoli et al., 1990), “quelling” in *Neurospora crassa* (Romano and Macino, 1992), and formalized as “RNA interference” in the Nobel Prize-awarded work in *Caenorhabditis elegans* (Fire et al., 1998), our molecular understanding of the RNAi mechanism has greatly increased. Importantly, RNAi silences genes in two fundamental and non-exclusive ways: transcriptional and post-transcriptional gene silencing (PTGS) (Figure 1.5).

### RNAi Inducing Transgene

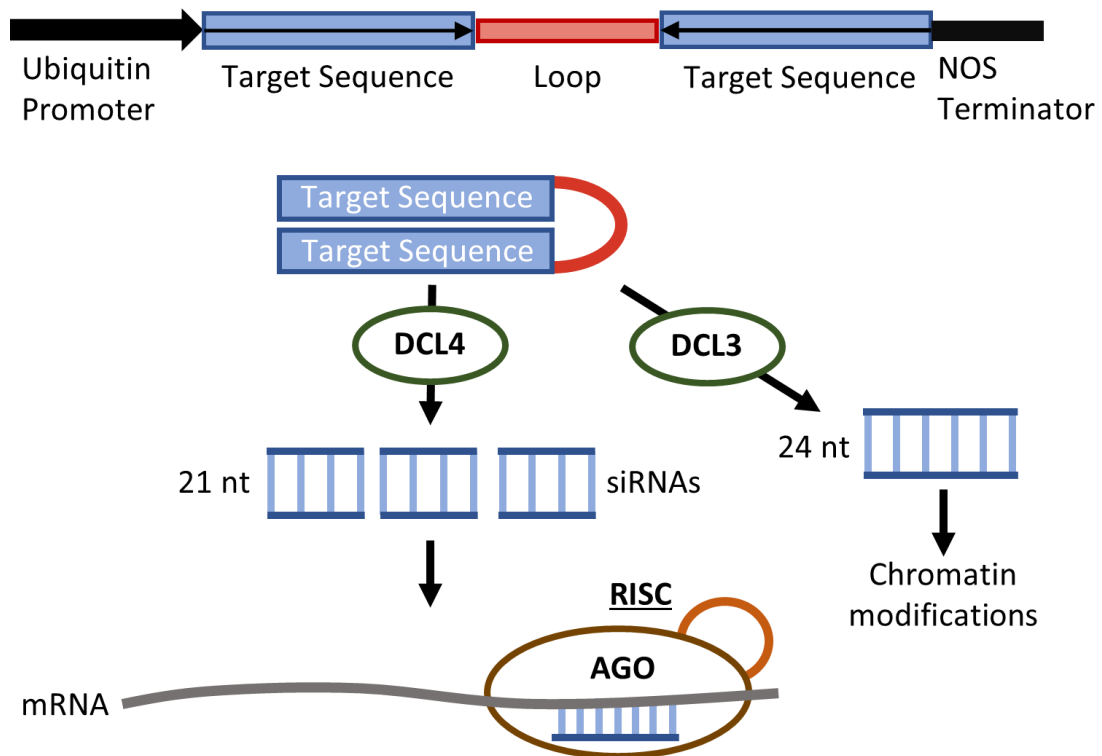


**Figure 1.5** RNAi-mediated loss-of-function. Schematic of an RNAi inducing transgene. The desired target of RNAi is expressed as inverted repeats separated by a loop region that facilitates the formation of a long hairpin RNA structure, resulting in processing by the endogenous RNAi machinery. The processed siRNAs then silence the target gene(s) either transcriptionally or post-transcriptionally.

In both instances, long dsRNA is processed by an RNase III enzyme Dicer resulting in multiple small, ~21 nucleotide dsRNA fragments named short interfering RNAs (siRNAs). Unlike humans and *C. elegans* that contain only one Dicer gene, plants contain multiple Dicer-like genes with the precise siRNA length and interference pathway primarily dictated by the dicer enzyme that processed the initial dsRNA (Margis et al., 2006; Small, 2007). After Dicer processing, a given siRNA is loaded into an Argonaute protein followed by association of other dsRNA-binding proteins and selection of the primary RNA strand, thus creating the RNA-induced silencing complex (RISC) (Wilson and Doudna, 2013). In PTGS, a functional RISC will then bind to complementary RNA and either degrade the transcript or prevent translation. Therefore, one cannot conclude the absence of RNAi by investigating transcript abundance.

In one of the great conveniences of molecular biology, the endogenous RNAi machinery can be easily induced by exogenous application of dsRNA. In this way, researches can easily downregulate multiple genes of interest by expressing a long, concatenated sequence of gene targets as an inverted repeat, thereby forming a double-stranded, hairpin RNA that elicits RNAi (Figure 1.5). Fascinatingly, RNAi appears particularly robust and potent in plants. This is evidenced by the functional diversification of the dicer-like enzymes (Margis et al., 2006), greater stringency of micro RNA (miRNA) complementarity relative to metazoans (Kamthan et al., 2015), systemic spread of the

RNAi trigger (Voinnet and Baulcombe, 1997), graft transmissibility (Palauqui et al., 1997), and amplification of the original RNAi trigger through a process termed “transitivity” (Himber et al., 2003; Moissiard et al., 2007). Despite the robustness and simplicity of induction of RNAi in plants, the plant cell wall presents a non-trivial barrier for RNAi-based experiments. Therefore, research into alternative siRNA delivery vehicles, such as with carbon nanotubes (Demirer et al., 2020), is an active area of development. On the other hand, this problem can be circumvented by prudent selection of a model plant more amenable to manipulation, such as the moss *Physcomitrella patens*.

As mentioned above, *P. patens* has emerged as a popular platform to use reverse genetics to answer basic cell biological questions (Rensing et al., 2020). Like other plants, the genome of *P. patens* contains multiple gene duplications (Lang et al., 2018), which impedes traditional gene knockout approaches. As a result, the use of either long dsRNA or artificial micro RNA (amiRNA) to induce RNAi of gene families is frequently encountered in the literature (Arif et al., 2013). Long dsRNA-based RNAi appears to be the prevalent approach for gene silencing over amiRNA in *P. patens*, likely due to the ease of use and maximization of silencing efficacy. Recall that the dsRNA is processed into many unique siRNAs (Figure 1.4b); therefore, opposed to the one unique targeting sequence of an amiRNA, the resulting pool of distinct siRNAs likely contains an efficacious 21 nucleotide targeting sequence. However, this enhancement comes with the potential cost of increased off-target activity. Fortunately, straightforward complementation experiments with the targeted gene allow definitive determination of off-target effects. For example, the 5' or 3' UTRs are frequently targeted with dsRNA to

enable complementation with the same coding sequence lacking the UTRs, thereby evading the RNAi machinery (Vidali et al., 2009; Vidali et al., 2010a).

Plant tip growth, an extreme variant of traditional polarized growth, has been extensively studied in *P. patens* using RNAi to discover genes involved in this fundamental and conserved process (Vidali and Bezanilla, 2012). RNAi-based investigation of tip growth using *P. patens* represents a powerful platform, as phenotypes can be identified within one week of transformation with the RNAi construct. Additionally, reagents and analysis pipelines are well-established given the wide-adoption of the technique. Despite the successes of RNAi in *P. patens* and plants writ large, two fundamental disadvantages remain: variable efficacy of target silencing and the manual labor required to isolate silencing plants from a heterogeneous population. A new RNAi methodology that addresses both limitations would be an invaluable addition to the plant biologist's reverse genetics toolbox.

## **1.9 Concluding Remarks**

Approximately 500 million years ago marks one of the most important events in the history of Earth, the land colonization of plants (Rensing, 2018). This event and the subsequent expansion and diversification of embryophytes (land plants) was the requisite event for creation of modern-day atmospheric oxygen levels, thereby supporting the evolution of life on land (Lenton et al., 2016). Despite the length of evolutionary time separating that initial event and the present day, a remarkable degree of conservation is found in fundamental processes when examining representative extant species between the early diverging bryophytes and vascular plants (Delaux et al., 2019). Some of these conserved processes were necessary and novel innovations for survival on land, such as the

production of flavonoids to absorb harmful UV-B (Wolf et al., 2010) and symbiotic relationships with microorganisms to acquire necessary nutrients (Field et al., 2015). However, other essential processes, such as cell polarization, pre-date land colonization and were likely present in the last common eukaryotic ancestor. Despite the ancient history and apparent homology across eukaryotes, we know surprisingly little about how plants achieve the extraordinarily organized and self-propagating mechanism of polarized growth. To address this critical gap in the plant biology field, this dissertation develops a novel tool and integrates it with existing quantitative cell biological and biochemical techniques to advance our mechanistic understanding of plant polarized growth.

## **Chapter 2 : Robust survival-based RNAi of gene families using in tandem silencing of adenine phosphoribosyltransferase**

---

## 2.1 Abstract

RNA interference (RNAi) enables flexible and dynamic interrogation of entire gene families or essential genes without the need for exogenous proteins, unlike CRISPR-Cas technology. Unfortunately, isolation of plants undergoing potent gene silencing requires laborious design, visual screening, and physical separation for downstream characterization. Here, we developed a novel APT-based RNAi technology (APTi) in *Physcomitrella patens* that simultaneously improves upon the multiple limitations of current RNAi techniques. APTi exploits the pro-survival output of transiently silencing the APT gene in the presence of 2-fluoradenine, thereby establishing survival itself as a reporter of RNAi. To maximize silencing efficacy of gene targets we created vectors that facilitate insertion of any gene target sequence in tandem with the APT silencing motif. We tested the efficacy of APTi with two gene families, the actin-dependent motor, myosin XI (a,b), and the putative chitin receptor Lyk5 (a,b,c). The APTi approach resulted in a homogenous population of transient *P. patens* mutants specific for our gene targets, with zero surviving background plants within 8 days. The observed mutants directly corresponded to a maximal 93% reduction of myosin XI protein and complete loss of chitin-induced calcium spiking in the Lyk5-RNAi background. The positive selection nature of APTi represents a fundamental improvement in RNAi technology and will contribute to the growing demand for technologies amenable to high-throughput phenotyping.

## 2.2 Introduction

Loss-of-function studies have long served as building blocks of our understanding of biological processes. Currently, the researcher is confronted with an ever-growing toolbox

to perturb gene function at the genetic, transcript, or protein level, with each presenting its unique challenges and insights (Housden et al., 2017). CRISPR-Cas technology has facilitated targeted genetic knockouts in previously intractable systems, but its efficacy is limited by accessibility of the genetic locus and is subject to off-target effects (Horlbeck et al., 2016; Jensen et al., 2017; Verkuil and Rots, 2019). Furthermore, genetic knockouts cannot isolate essential genes or reversibly interrogate developmental, tissue, or cell specific functions of a given gene or splice variant. Importantly, recent work has questioned the lasting dogma that genetic knockouts are the “gold standard” loss-of-function approach (Rossi et al., 2015; Smits et al., 2019). These studies demonstrated genetic compensation or residual protein expression, signifying that genetic alterations alone are insufficient to directly infer gene function. Therefore, reliable inferences of loss-of-function studies will require integration of multiple independent approaches (Deans et al., 2016), ideally in a high-throughput manner to maximize confidence.

RNA interference (RNAi) is a popular gene silencing strategy that does not depend upon exogenous proteins, such as Cas9, and enables reversible reduction of protein levels through targeted degradation of mRNA (Small, 2007). RNAi's ease of use and flexibility lends itself as an indispensable complement to genetic editing techniques. Traditionally, RNAi in plants is induced through expression of long inverted repeats that self-base pair to form double-stranded RNA (dsRNA), which is then processed into multiple small interfering RNAs (siRNA) and targeted to complementary sequences within mRNA (Chuang and Meyerowitz, 2000; Hannon, 2002; Baulcombe, 2004). Importantly, a single dsRNA targeting one gene can simultaneously silence multiple genes with sufficient similarity, or a single dsRNA can be generated that contains multiple gene

targets in tandem for simultaneous silencing (Vidali et al., 2007a; Li et al., 2013). The expression of dsRNAs can be specifically modulated, either through induction or unique promoters, which allows developmental and cell-type specific reduction of even essential gene products (Byzova et al., 2004; Nakaoka et al., 2012; Miki et al., 2015; Liu and Yoder, 2016). Despite these advantages, RNAi is hindered by variable efficacy of target gene silencing and potential off-target effects (Xu et al., 2006). However, some argue the prevalence of off-target effects is overstated (Zimmer et al., 2019), and importantly an ideal RNAi experiment should demonstrate rescue of the gene silencing phenotype (Vidali et al., 2009; Vidali et al., 2010a; Ding et al., 2018). Work using artificial microRNAs (amiRNA) attempts to circumvent the limitations of traditional dsRNA-based RNAi by engineering a single siRNA (Schwab et al., 2006; Gutierrez-Nava et al., 2008). Although amiRNA technology ameliorates possible off-targets derived from the initial dsRNA, evidence in *Physcomitrella patens* showed generation of additional siRNAs upon cleavage of the amiRNA target, potentially negating the specificity of the amiRNA (Khraiweh et al., 2008). Furthermore, amiRNAs display variable silencing efficiency, thereby necessitating screening of multiple amiRNAs and limiting experimental throughput (Li et al., 2013; Zhang et al., 2018). To date, no RNAi method addresses another potential source of variability of silencing: transcriptional silencing of the RNAi transgene itself, likely mediated by DCL3 (Morel et al., 2000; Fusaro et al., 2006; Small, 2007).

Generation and characterization of loss-of-function mutants using gene silencing methods is fundamentally a two-step process: (1) the molecular mechanism resulting in gene silencing; (2) the identification and isolation of your target undergoing gene silencing

to further characterize. Recent advancements in gene silencing technologies focused on enhancing the flexibility and robustness of (1) (Hauser et al., 2013; Zhang et al., 2018) but fail to address the practical limitations imposed by (2). Identification of actively silencing mutants has been eased by coupling the silencing target of interest to a reporter, such as a nuclear-localized fluorescent protein (Bezanilla et al., 2005a; Vidali et al., 2007a; Vidali et al., 2010a; van Gisbergen et al., 2018a; Zhang et al., 2018). When paired with an automated or semi-automated image acquisition and analysis pipeline the burden of identifying silencing mutants is substantially mitigated (Wu and Bezanilla, 2012; Galotto et al., 2019). Nevertheless, the tedium of manually isolating silencing plants remains. This limitation is a consequence of traditional gene-silencing construct design, whereby the silencing module is regulated independently from the selectable marker. A typical gene-silencing experiment will contain a heterogeneous population of actively silencing plants, presumably a result of the plant silencing the exogenous silencing module to rescue itself (Fusaro et al., 2006; Khraiweh et al., 2010). This transcriptional-based silencing not only increases variability of target silencing, but when coupled with visual screening it exacerbates the manual labor required to isolate mutants. Therefore, downstream characterization of silencing plants, such as qPCR and western blots is stymied. Furthermore, certain reporter-based silencing limits the experimental scope to testing only within established reporter lines, (Bezanilla et al., 2003a; Nakaoka et al., 2012). For example, using a fluorescent reporter to infer silencing could complicate the subsequent use of other fluorescent outputs, such as biosensors or fluorescent fusions for protein localization, to characterize mutant function.

Here, we generated a modular, Gateway-based, RNAi construct that couples silencing any gene(s) of interest in tandem with silencing of adenine phosphoribosyltransferase (APT-interference/APTi). This approach results in near undetectable levels of background (non-silencing) transformants, thereby trivializing the identification and isolation of actively silencing plants to the simple observation and harvesting of all living plants. Unlike traditional antibiotic positive selection followed by visual screening, our new construct simultaneously selects for transformation and silencing through positive selection alone. We achieved this by exploiting the ubiquitous selectable marker system APT, which converts purine analogs to cytotoxic nucleotides (Schaff, 1994). The APT loss-of-function selection system has been successfully used in plants (Moffatt and Somerville, 1988; Charlot et al., 2014), mammals (Schaff et al., 1990), and bacteria (Levine and Taylor, 1982), but to our knowledge, all experiments with APT involve stable genetic mutants. To quantitatively evaluate the performance and robustness of our APTi system, we separately targeted two gene families, myosin XI (a,b) and Lyk5 (a,b,c), using the plant model organism *Physcomitrella patens*. Targeting the myosin XI family using APTi resulted in an exclusively mutant surviving population, displaying the characteristic loss-of-growth growth phenotype (Vidali et al., 2010a) and a >90% reduction of target myosin XI protein abundance. Additionally, APTi enabled rapid functional analysis of the previously uncharacterized *P. patens* Lyk5 chitin receptor family, which resulted in complete desensitization of *P. patens* to chitin. Together, APTi-based silencing efficacy far surpasses other dsRNA-based methods (Vidali et al., 2007a; Vidali et al., 2010a; Nakaoka et al., 2012; Guo et al., 2019), is comparable to silencing

efficiencies for optimized amiRNAs (Zhang et al., 2018), and simplifies downstream analysis for functional genomics.

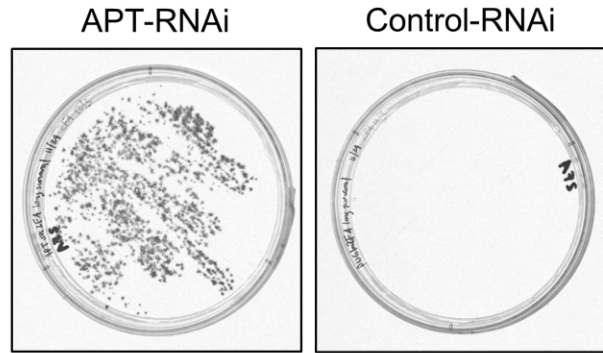
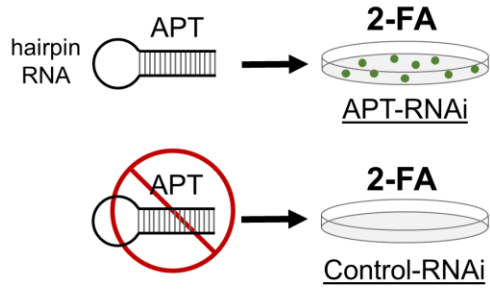
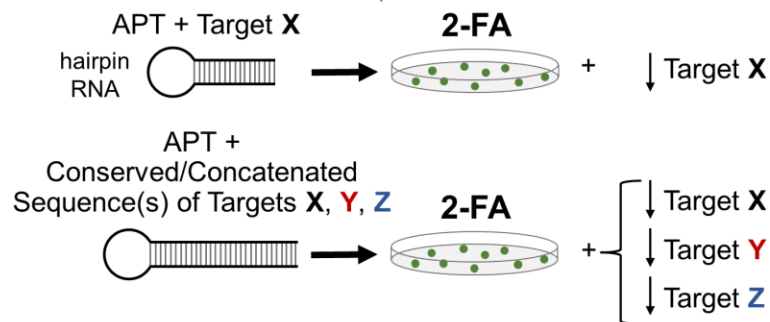
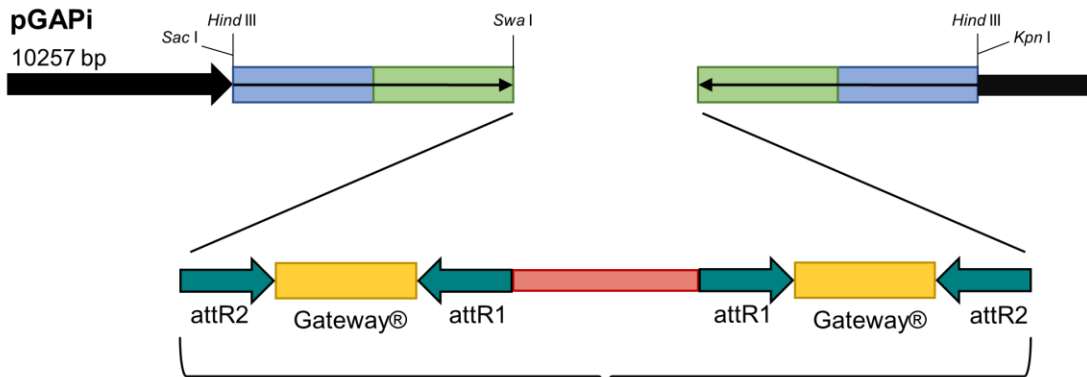
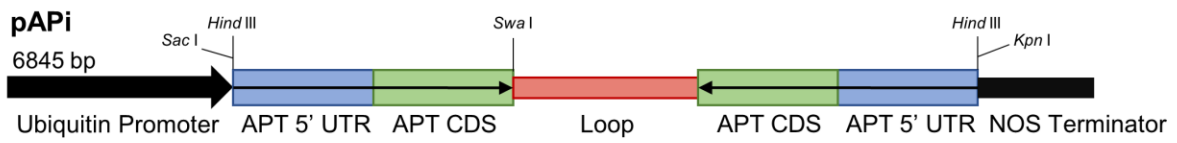
## **2.3 Results**

### **2.3.1 Development of A Novel Positive Selection RNAi Methodology Based on Endogenous APT Activity**

Current RNAi methods produce a range of phenotype severity due to variable silencing efficiencies. This variability necessitates optimization experiments that screen fluorescent reporters to maximize silencing by gene sequence targets (Li et al., 2013; Zhang et al., 2018). We sought to simultaneously improve RNAi silencing efficiency and streamline characterization of RNAi mutants by coupling silencing of the gene target with a survival advantage. Previous work in *P. patens* directly coupled the sequence of a stably integrated, constitutively expressed reporter, such as a fluorescent protein and/or GUS, to the gene target sequence in inverted repeats (Bezanilla et al., 2003a; Bezanilla et al., 2005a; Nakaoka et al., 2012). Therefore, expression would result in dsRNA formation and co-reduction of the intracellular reporter and the coupled target gene. We reasoned that coupling of a lethal reporter sequence in tandem with any other gene sequence would result in maximal co-silencing to ensure silencing of the lethal reporter, thereby promoting survival.

The adenine phosphoribosyltransferase (APT) gene has been frequently used as a reporter to evaluate gene-targeting efficiency (Schaefer, 2001; Charlot et al., 2014). Functional APT converts adenine analogs, such as 2-fluoroadenine (2-FA), to cytotoxic nucleotides (Schaff, 1994). Therefore, sufficient reduction of APT activity will impart resistance to 2-FA, but this has only been demonstrated in genetic knockouts. To test if

silencing of PpAPT (Pp3c8\_16590) effectively conferred survival to plants grown on 2-FA, we inserted an APT targeting sequence into a previously developed RNAi vector that also contains a reporter targeting sequence (Bezanilla et al., 2005a). To maximize silencing efficacy, we generated an APT targeting sequence consisting of the 5' UTR (179 bp) and first 210 bp of the APT gene. The APT silencing construct (APT-RNAi) conferred resistance to wild-type *P. patens* cultured on 1.25 µg/mL 2-FA, whereas zero plants survived on 2-FA when transformed with a control plasmid lacking the APT silencing sequence (Control-RNAi) (Figure 2.1a). This result clearly establishes survival on 2-FA paired with APT targeting as a conspicuous phenotypic reporter of active silencing.

**A****B**

**Figure 2.1** Proof-of-principle and construction of APT-based RNAi (APTi) vectors to enable positive selection of actively silencing plants. A, Illustration of the APT-interference positive selection principle: plants are transformed with a vector that creates a long dsRNA hairpin targeting the APT gene, thereby reducing endogenous APT levels and subsequent production of cytotoxic nucleotides when supplemented with 2-fluoroadenine (2-FA). Targeting APT using RNAi is sufficient for transformed plants to grow on standard PpNH<sub>4</sub> medium supplemented with 1.25 µg/mL 2-FA. B, Schematics of the APT-based RNAi vectors. The pAPi (plasmid APT RNAi) and pGAPi (plasmid Gateway® APT RNAi) constructs were created using the pUGi and pUGGi vectors, respectively, from Bezanilla et al., 2005 as templates. The thin black arrows indicate the direction of the open reading frame, and the inverted repeat regions of both constructs are flanked by a constitutive maize ubiquitin promoter (thick black arrow) and a NOS terminator sequence (black rectangle). Both constructs target the 5' UTR (blue rectangle, 179 bp) and coding sequence (green rectangle, 210 bp) of the APT gene. pAPi contains only the loop (red rectangle, 402 bp in pAPi, 392 bp in pGAPi) region within the inverted repeat, whereas pGAPi contains inverted Gateway® sites to facilitate insertion of target sequence. The target may be unique to gene X, or if the target sequence is conserved the user can simultaneously silence multiple targets in tandem with APT silencing, thereby enabling survival of silencing plants

Our previous APT silencing experiment demonstrated feasibility, but further development of the technique was constrained by the available construct. As mentioned above, the first iteration of the APT-based interference (APTi) was inserted into a vector created specifically for RNAi (Bezanilla et al., 2005a). This construct included a pair of inverted Gateway® sites coupled to a target sequence (GUS) for an internal reporter of active silencing. The reporter sequence targeted a nuclear-localized GFP:GUS fusion protein, thereby requiring the use of a special transgenic line for RNAi experiments (Bezanilla et al., 2003a). In principle, our novel APTi would not require any specific moss line, and instead would permit the researcher to perform RNAi experiments in any genetic background. Therefore, we replaced the GUS reporter target sequence with the APT target sequence, while maintaining the inverted Gateway® cassettes and loop region and named the construct pGAPi (Figure 2.1b). This construct allows straightforward insertion of any gene sequence and ensures fusion to the APT target, thus permitting inference of

gene silencing within surviving plants. Importantly, entire gene families can be targeted by simple insertion of a conserved sequence of approximately 400 bp, or concatenation of individual target sequences followed by cloning into our pGAPi (Figure 2.1b). Additionally, we created another APTi construct, named pAPi, which lacks the internal Gateway® cassettes to serve as a “positive control” for any RNAi experiment (Figure 2.1b). Together, these constructs serve as the foundation for our novel APT-based RNAi (APTi) that advances positive selection as an effective reporter of gene silencing.

### **2.3.2 APTi Experimental Design for High-throughput Phenotyping**

Although our APTi system clearly selects for silencing plants cultured over a two-week period by visual inspection (Figure 2.1a), we sought to establish a rapid, semi-automated microscopy assay using APTi for plant phenotyping. A fundamental attribute of any high-throughput assay is the effective and automated discrimination between objects of interest and background that co-occupy the same space. Our APTi system simplifies the problem of automated separation. Unlike fluorescence reporter systems where the reporter signal is continuous and exhibits natural variation, APTi reduces separation of silencing and non-silencing plants to the binary decision of alive or dead. We reasoned that chlorophyll autofluorescence could function as a proxy for plant survival, thereby enabling automated detection of alive, and therefore actively silencing, plants. In principle, all plants successfully transformed with a construct silencing APT, pAPi (Figure 2.1b), will survive on 2-FA medium, whereas plants transformed with an RNAi construct silencing a non-existent reporter, pUGi (Bezanilla et al., 2005a), will die.

We tested this by using the experimental design illustrated in Figure 2.2. *P. patens* protoplasts were transformed with either pAPi or pUGi, allowed to regenerate for 4 days,

then transferred to growth medium supplemented with 1.25  $\mu\text{g}/\text{mL}$  2-FA. Importantly, during the optimization phase of this assay we observed substantial variability in the outcome of 2-FA selection. We empirically determined that starting the selection four days post-transformation and making the 2-FA selection plates fresh on the day of selection mitigated essentially all experimental variability. We strongly suggest first optimizing the 2-FA selection concentration when applying the APTi system, as our results were all obtained using a single lot of 2-FA from Oakwood Chemical, SC, USA.

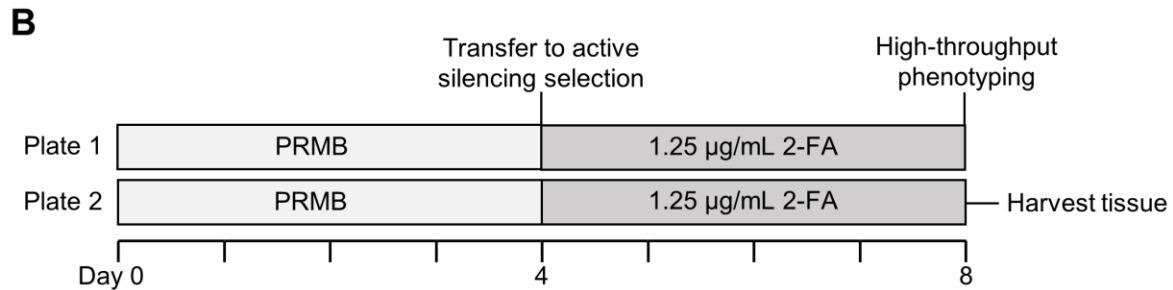
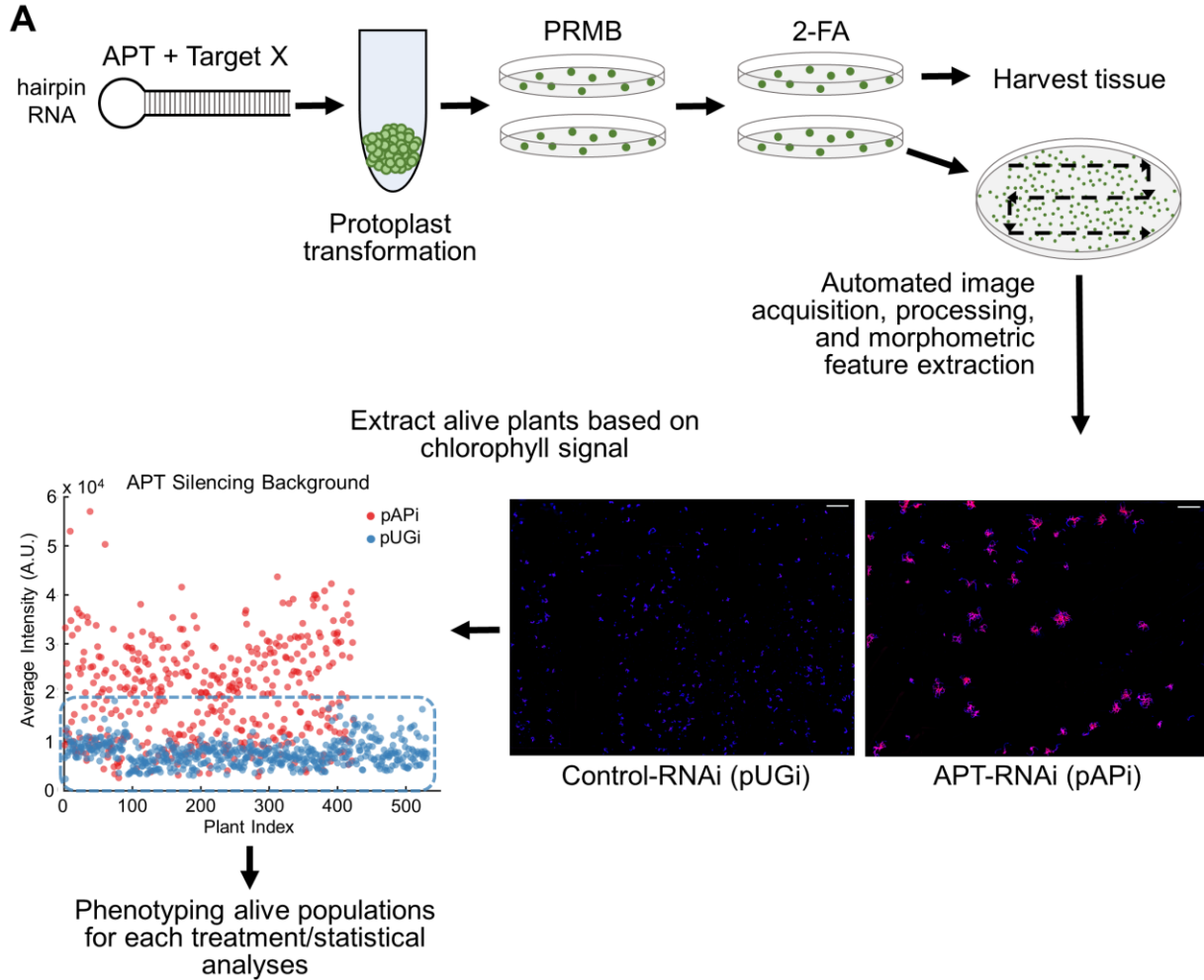


**Figure 2.2** Experimental strategy and timeline for the novel APTi system. A, Optimized experimental pipeline for transient transformation of *P. patens* protoplasts and high-throughput acquisition and analysis for the APTi system. Images are a subsection of the entire plate area and demonstrate the characteristic difference in survival between conditions that do (pAPi) or do not (pUGi) silence APT. The scatter plot determines the background threshold value, which is based upon the maximal observed chlorophyll signal in the Control-RNAi condition (pUGi, blue dots). Each point corresponds to an individual plant, where the points are pooled from three independent experiments. B, Timeline of events for an APTi assay. Typically, each condition is plated in at least duplicate for adequate sample abundance for both imaging and molecular analyses.

Following four days on 2-FA supplemented growth medium, cultures were removed from the growth chamber for protein extraction and microscopy analysis (Figure 2.2b). To facilitate high-throughput phenotyping and remove human bias, we used an epifluorescent microscope equipped with an automated stage integrated with image tiling and stitching software. This enabled large region-of-interest acquisition, with the size of the ROI only constrained by the memory available to the computer. For our experiments, every composite image is constructed from a 12x12 grid of single images, with a 15% overlap, which corresponds to an ROI surface area of approximately 1.8 cm<sup>2</sup>.

To simplify downstream image segmentation all plants were stained with calcofluor to label the cell wall before imaging. Each individual image contained two channels, the chlorophyll autofluorescence and the calcofluor signal. Visualization of the chlorophyll signals of APT-RNAi and Control-RNAi clearly reveals the efficacy of the APTi system: not a single plant with endogenous APT survives and does not markedly grow beyond the initial regeneration size (Figure 2.2a). This result is reproducible, as the chlorophyll signal across three independent experiments for Control-RNAi plants consistently clustered below a characteristic intensity (Figure 2.2a). We used chlorophyll intensity parameter as a threshold, from which we functionally partitioned a mixture of plants on a plate into alive (silencing) and dead (non-silencing) plants (Figure 2.2a). The alive or dead classification ensured that the morphometric parameters extracted from the image analysis pipeline was confined to only alive, and therefore silencing, plants. Therefore, it stands to reason that when using our APTi system any statistically supported observed difference between control and treatment plants is directly attributable to silencing of the targeted gene(s).

### 2.3.3 The APTi System Silences the Myosin XI Family with High Efficacy

We demonstrated that silencing of APT permits potent positive selection of actively silencing plants (Figure 2.2a), but we sought to extend APTi to mutant analysis. We reasoned that insertion of a target sequence into our APTi vector (Figure 2.1b) would produce in tandem silencing of APT and the target gene. To test this hypothesis we exploited the well-characterized transient *myosin XI(a+b)* RNAi mutant that produces a dramatic loss of polarized growth phenotype (Vidali et al., 2010a). Furthermore, the *myosin XI(a+b)* mutant was previously generated using a fluorescent reporter-based RNAi strategy, allowing a direct comparison of methodology.

In *P. patens*, the myosin XI gene family contains two functionally redundant isoforms, XIa and XIb, which are both expressed in protonemata (Vidali et al., 2010a). To simultaneously silence both myosin XI genes and allow for rescue experiments, we created an APTi construct that contains a concatenated 5' UTR sequence derived from both isoforms of myosin XI. We named this construct 'myoUTi(a+b)', and it resulted in a striking recapitulation of the *myosin XI* phenotype (Figure 2.3a). Impressively, nearly every surviving plant manifested the characteristic "bunch of grapes" morphological phenotype (Figure 2.4). This is exemplified by the relatively narrow distributions of the APTi myosin XI knockdown in the two morphology parameters, solidity and area (Figure 2.3b). We speculate the survival advantage inherent to our APTi method could reduce phenotypic variability sometimes observed in RNAi experiments.

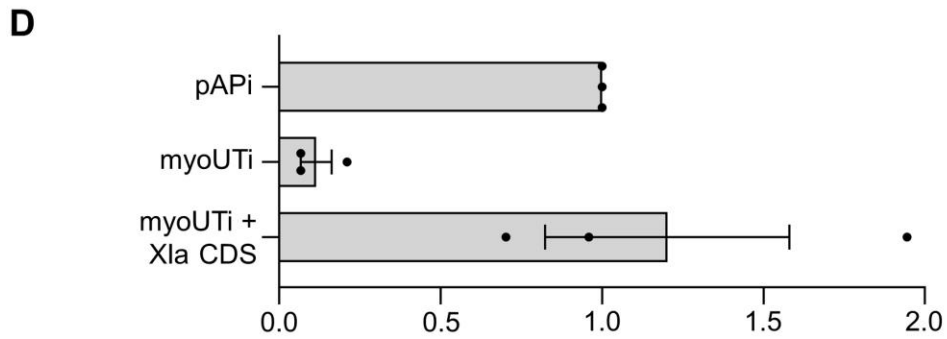
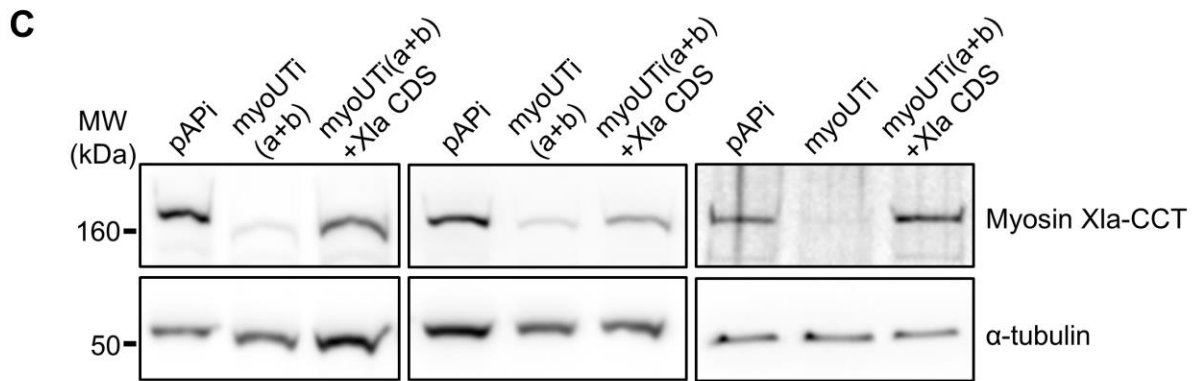
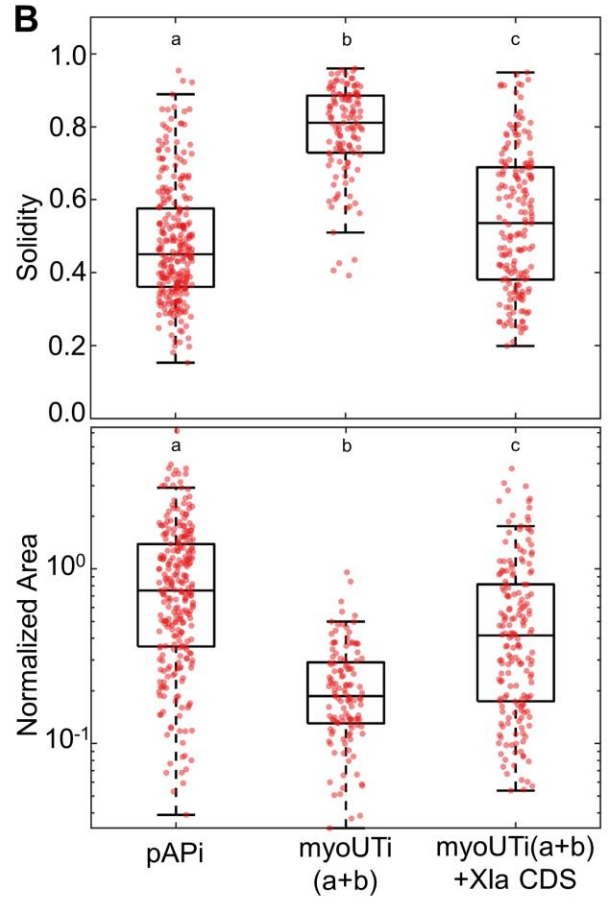
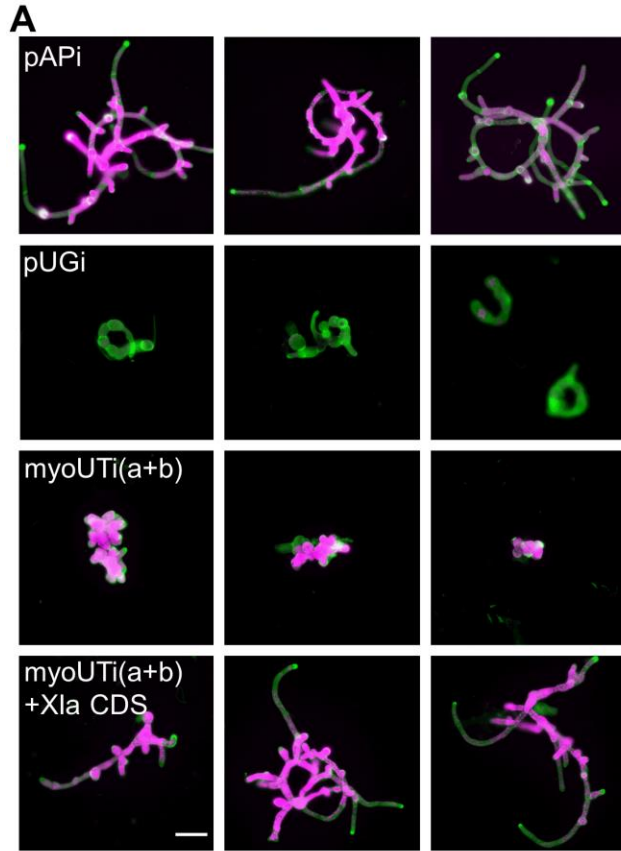


**Figure 2.3** The APTi system robustly silences the myosin XI family in *Physcomitrella patens*. A, Representative images of 8-day old plants regenerated from protoplasts transformed with APTi vectors targeting APT alone (pAPi), APT in tandem with a concatenated 5' UTR sequence for myosin Xla and Xlb (myoUTi), targeting a non-existent GUS sequence (pUGi), or myoUTi co-transformed with a construct overexpressing myosin Xla's coding sequence. All images are cropped from composite images that capture a large sample area for an individual condition, as shown in Figure 2A. For every condition, each image corresponds to an independent experiment. Chlorophyll autofluorescence is colored magenta and calcofluor signal is colored green. Scale bar = 100  $\mu$ m. B, Quantification of morphometric parameters solidity and area from three independent experiments. Area is normalized to the mean area of the pAPi condition, which represents near wild-type growth morphology. pAPi, n = 270; myoUTi, n = 125; myoUTi + Xla CDS, n = 178. Letters indicate statistical difference ( $P < 0.001$ ) between groups as determined by one-way ANOVA with post-hoc Tukey test. C, Western blots demonstrating the reduction and restoration of myosin XI protein levels when using the novel APTi system. Each experiment represents an independent transformation and subsequent plant harvesting and western blotting. 10  $\mu$ g of total protein was loaded per lane. Myosin XI was probed using a polyclonal antibody generated against the myosin Xla coiled-coil tail (CCT) fragment from *Physcomitrella patens* and  $\alpha$ -tubulin was used as a loading control. D, Densitometry of western blot signals was performed using ImageJ and shows an approximate 90% reduction of myosin XI and a complete rescue of myosin XI protein levels when compared to the pAPi control.

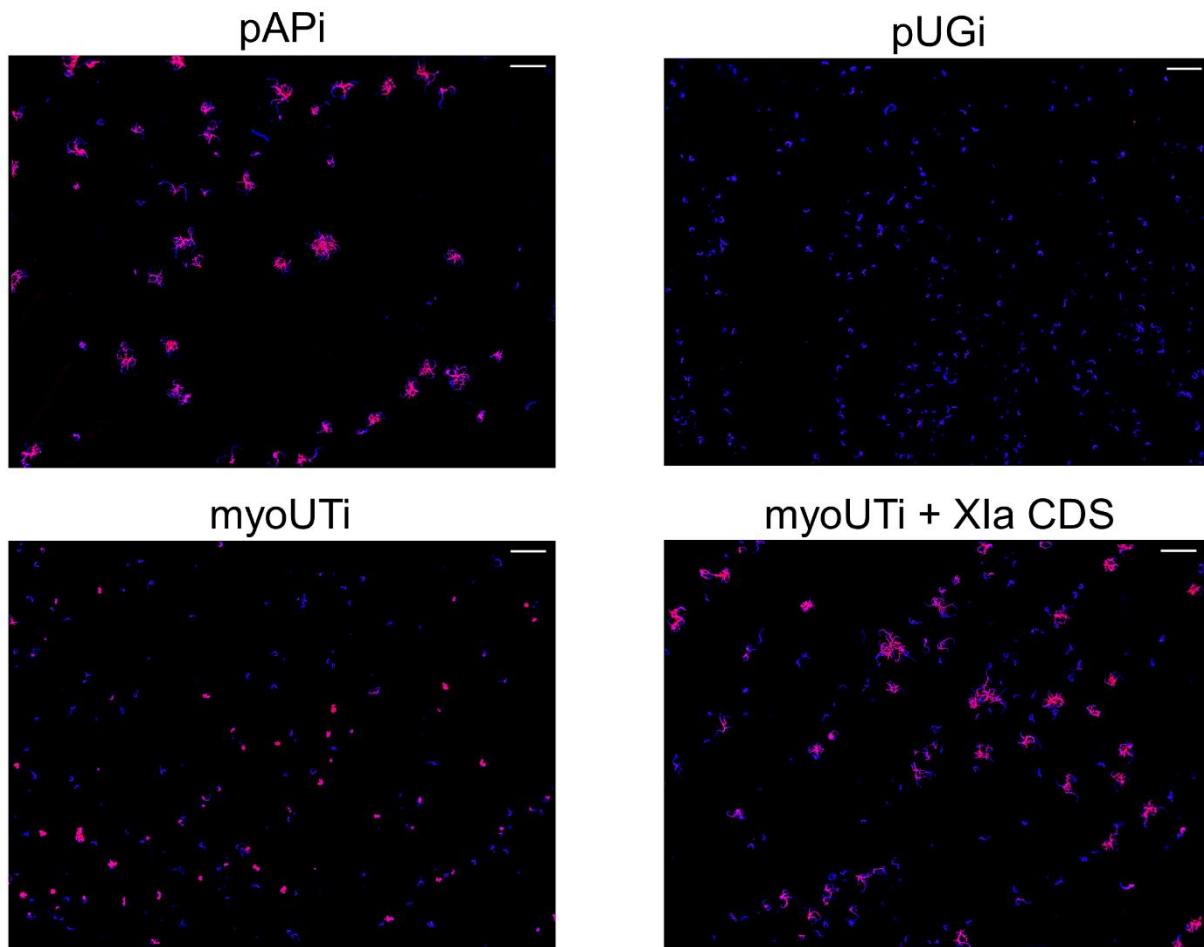


**Figure 2.4** The APTi system reduces variability in observed mutant phenotype. Each image is a composite of a 12x12 grid of individual images, which were automatically acquired at a 15% overlap using a Zeiss Axiovert 200M epifluorescent microscope covering a surface area of 180 mm<sup>2</sup>. The composite image was stitched together using Zeiss' AxioVision 4. The plants were stained with calcofluor (blue) and were sequentially imaged with the chlorophyll signal (red). Scale bar = 1 mm

We inquired whether this phenotype could be rescued in the APTi system by co-transforming the myoUTi(a+b) construct with a plasmid expressing only the coding sequence of myosin XIa, “XIa CDS,” thereby evading the silencing construct that targets the 5' UTR. We observed near complete rescue of the *myosin XI* phenotype (Figure 2.3a,b), demonstrating an absence of off-target effects and, more importantly, highlighting the rapid phenotyping utility of the APTi system when coupled with *P. patens*. Within 8-days our APTi system isolated through positive selection a relatively homogenous population of mutant plants, which are amenable to rescue. Our APTi system produced average myosin XI mutant morphological parameters similar to a myosin XI mutant derived from RNAi using an internal GFP reporter system (Vidali et al., 2010a), but without non-silencing background plants. Together, these results support our prediction that aberrant morphologies observed using the APTi system are caused by silencing of the conjugated target, in our case myosin XI.

As our novel APTi approach removes essentially all background, we asked if the previously intractable problem of reliable protein quantification could be trivialized to harvesting all material present on the 2-FA plate. To accurately quantify myosin XI protein abundance using our APTi method, we first established the linear range of our antibodies. To reflect our RNAi experimental conditions, we transformed wild-type moss with pAPi, grew on medium supplemented with 2-FA, then harvested the entire plate at 8-days post-transformation. Total protein was determined using a Bradford microplate microassay (Bio-Rad), then a range of total protein (1-20  $\mu$ g) was probed using both an in-house developed antibody against myosin XIa's coiled-coil tail (CCT) region and a publicly

available anti-alpha tubulin antibody (DSHB: AA4.3). This approach revealed an approximate linear range for both antibodies from 5-20  $\mu\text{g}$  total protein (Figure 2.5a). Importantly, under equivalent conditions our limit of detection for endogenous, wild-type myosin XI is approximately 1  $\mu\text{g}$  total protein (Figure 2.5a). This step is essential, as it allows for confident, semi-quantitative estimation of the extent of protein reduction. Without this, the wild-type protein of interest could be loaded at or very near the limit of detection, resulting in a complete absence of protein signal in the RNAi condition even if the true reduction is modest.

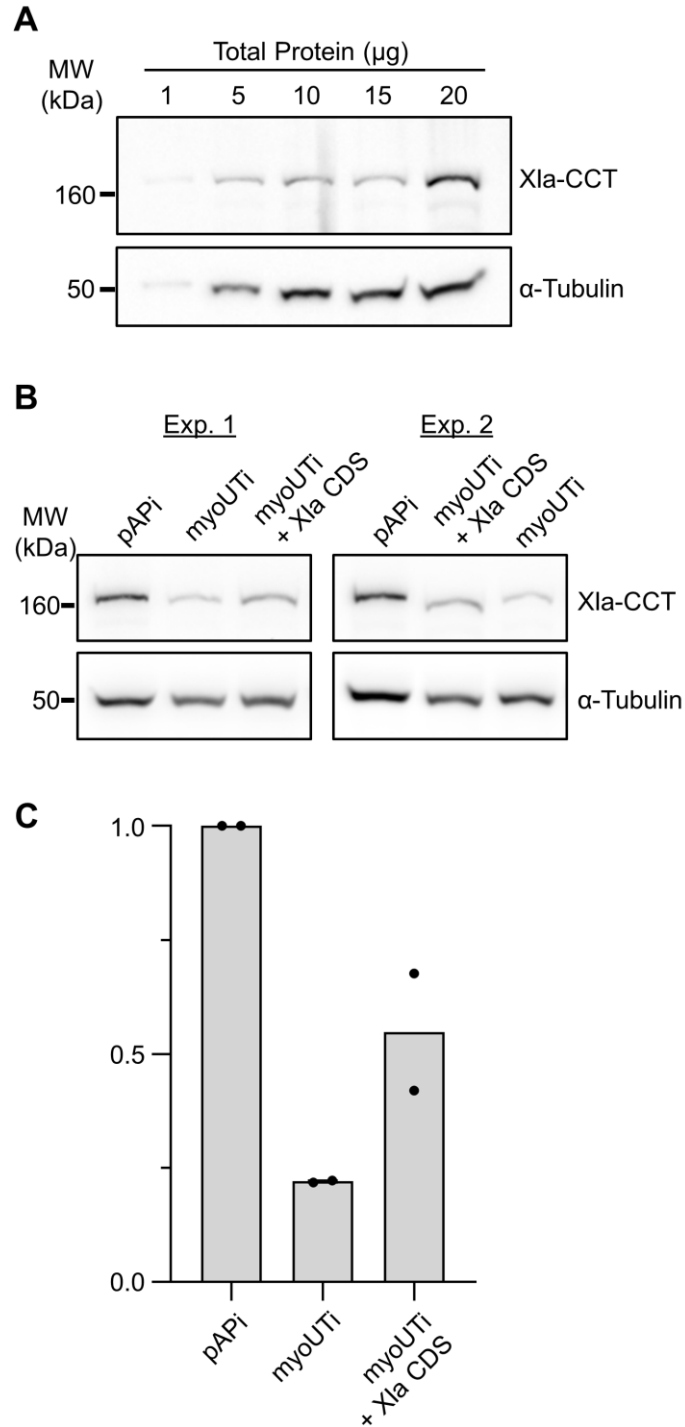


**Figure 2.5** Determination of the linear range of used antibodies and long-term reproducibility of western blots using the APTi system. A, Western blot demonstrating an overlap of the linear ranges for both the myosin Xla-CCT and  $\alpha$ -tubulin antibodies. All experiments used either 10 or 15  $\mu$ g of total protein. B, Two western blots from independent APTi experiments at two weeks post-transformation. 15  $\mu$ g of total protein was loaded per lane. C, Densitometry was performed using ImageJ and signal was normalized to the  $\alpha$ -tubulin loading control.

We performed an APTi experiment for myosin XI, as shown in Figure 2.3, and harvested at 8-days post-transformation. Every condition was implemented in at least duplicate to allow for both harvesting of plants and our phenotyping assay (Figure 2.2). In this way, the results of our protein analysis directly reflect the internal protein abundance and corresponding morphologies we observe in the phenotyping assay (Figure 2.3a). We observed a dramatic decrease of myosin XI in the “myoUTi” condition, which when normalized to  $\alpha$ -tubulin results in a maximal 93% reduction relative to the control (“pAPi”). Additionally, the rescued mutant morphology precisely corresponds to an almost wild-type restoration of myosin XI levels (Figure 2.3c,d). Of note, these results are consistent across independent experiments and results in an average silencing efficiency of 90% (Figure 2.3c,d). We explored the longevity target silencing using APTi by probing myosin XI at two weeks post-transformation. Although less potent than at 8-days post-transformation (Figure 2.3), myosin XI levels are still substantially reduced (Figure 2.5b,c), opening the possibility for long-term phenotyping. At the longer time, the rescue condition is noticeably weaker than at the short time point. We attribute this to loss of the myosin XI expression plasmid, as it is not under selection. Taken together, these data establish that aberrant phenotypes observed using our APTi system are directly attributable to reduction of target protein abundance.

### **2.3.4 APTi-based Silencing of the Lyk5 Family Disrupts *P. patens*' Response to Chitin Oligosaccharides**

Despite the success of the APTi system when applied to myosin XI, we could not discount the possibility that myosin XI was particularly amenable to APTi and alternative gene targets would yield less favorable results. To address this concern, we reasoned that the

Lyk5 gene family of *P. patens* presents an excellent candidate to test the robustness and potential for functional discovery using APTi. In *Arabidopsis*, LYK5 is a member of a gene family of lysin-motif (LysM) containing proteins and functions as a receptor for the fungal polysaccharide chitin, likely in concert with CERK1 (Cao et al., 2014). LYK5, together with LYK4 in *Arabidopsis*, functions redundantly in chitin perception, with the *lyk4 lyk5* double mutant losing all chitin sensitivity (Cao et al., 2014). Like *Arabidopsis*, application of chitin to *P. patens* elicits calcium transients (Galotto et al., 2020), resulting in the upregulation of a downstream defense response (Oliver et al., 2009; Alvarez et al., 2016); however, the mechanism of chitin perception in *P. patens* is unknown. Previous work has identified the putative ortholog of the co-receptor CERK1 in *P. patens* (Bressendorff et al., 2016); however, the ortholog of LYK5 chitin receptor is still unidentified. Phylogenetic analysis revealed a monophyletic group of three putative Lyk5 genes in *P. patens* (Pp3c7\_26350, Pp3c9\_5820, Pp3c1\_6050), which are homologous at the amino acid level to the LYK2/4/5 clade in *Arabidopsis* (Figure 2.6). Importantly, LYK2 expression is extremely low in *Arabidopsis*, thus limiting our functional interpretations to LYK4/5 (Liang et al., 2014). Our gap in understanding of how *P. patens* senses pathogenic fungi coupled with sequence homology between the LYK2/4/5 gene family of *Arabidopsis* and the Lyk5a/b/c family of *P. patens* presents an opportune test for our APTi system.

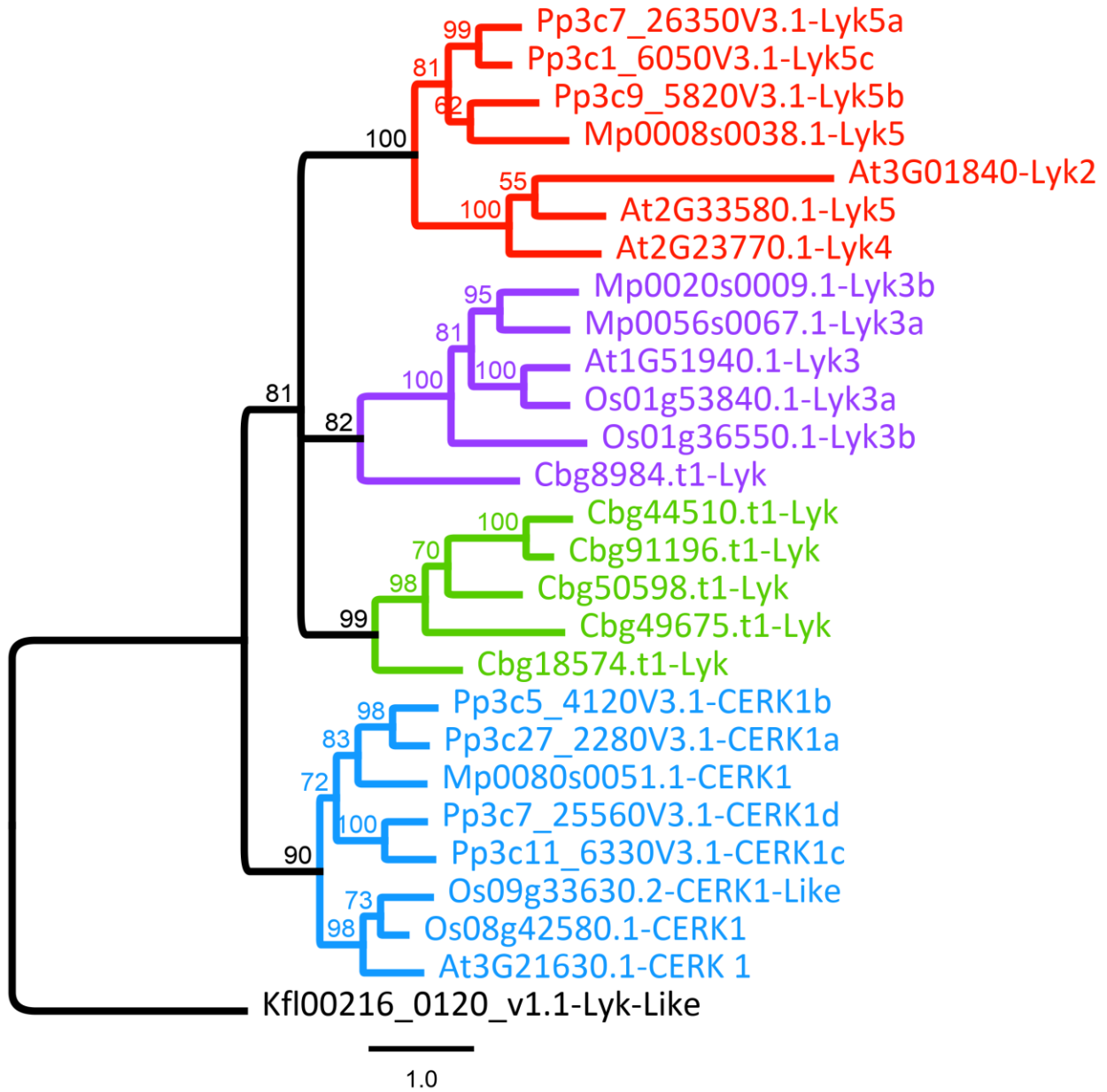


**Figure 2.6** Phylogenetic tree of Lyk genes from *P. patens* and other selected plant and alga species. Amino acid sequences from the full-length proteins were aligned with ClustalW, and a maximum likelihood consensus tree constructed with PHYML using the LG substitution model and 100 bootstraps in Geneious software. Numbers represent consensus support values for each branch above 50%. Pp – *Physcomitrella patens*, Mp- *Marchantia polymorpha*, At- *Arabidopsis thaliana*, Cb- *Chara braunii*, Os- *Oryza sativa*, Kf- *Klebsormidium flaccidum*. *K. flaccidum*'s sequence was used for rooting the tree.

To simultaneously target all three *P. patens* Lyk5 genes, we concatenated three separate sequences derived from the coding sequences of Lyk5a,b,c and cloned this into our novel pGAPi vector, producing the 'Lyk5-RNAi' construct. Based on our phylogenetic analysis, we hypothesized the Lyk5 family in *P. patens* is functionally homologous to LYK4/5 in *Arabidopsis*. Therefore, we predicted depletion of all three Lyk5 isoforms using APTi will result in a population of surviving plants that fail to elicit calcium spikes when stimulated with chitin oligosaccharides. To test this, we transiently transformed plants expressing the calcium sensor GCaMP6 (Nakai et al., 2001; Chen et al., 2013; Galotto et al., 2020) with our Lyk5-RNAi construct, transferred plants to selection 4-days post-transformation, then randomly selected plants at 8-days post-transformation for chitin treatment and imaging (Figure 2.7a). Plants only targeting APT displayed calcium spikes indistinguishable from wild-type when treated with chitin (Figure 2.7b), and the quantified parameters (Figure 2.7c, d) are consistent with previous results (Galotto et al., 2020), suggesting APT-RNAi alone has no influence on the output of our assay. When treated with Lyk5-RNAi, plants are rendered entirely insensitive to chitin (Figure 2.7b). Furthermore, the characteristic dose dependence of calcium signal on external chitin is abolished (Figure 2.7c) and calcium oscillations are non-existent when targeting the entire Lyk5 family (Figure 2.7d).

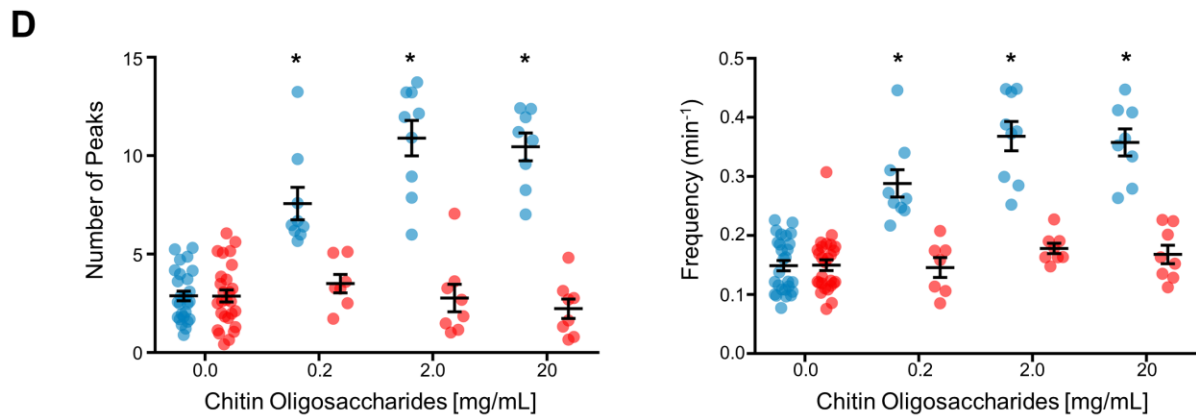
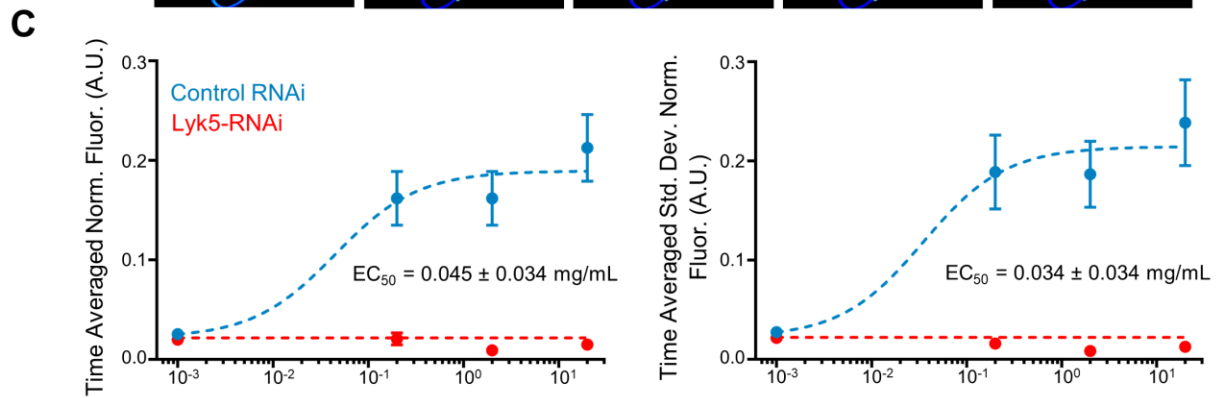
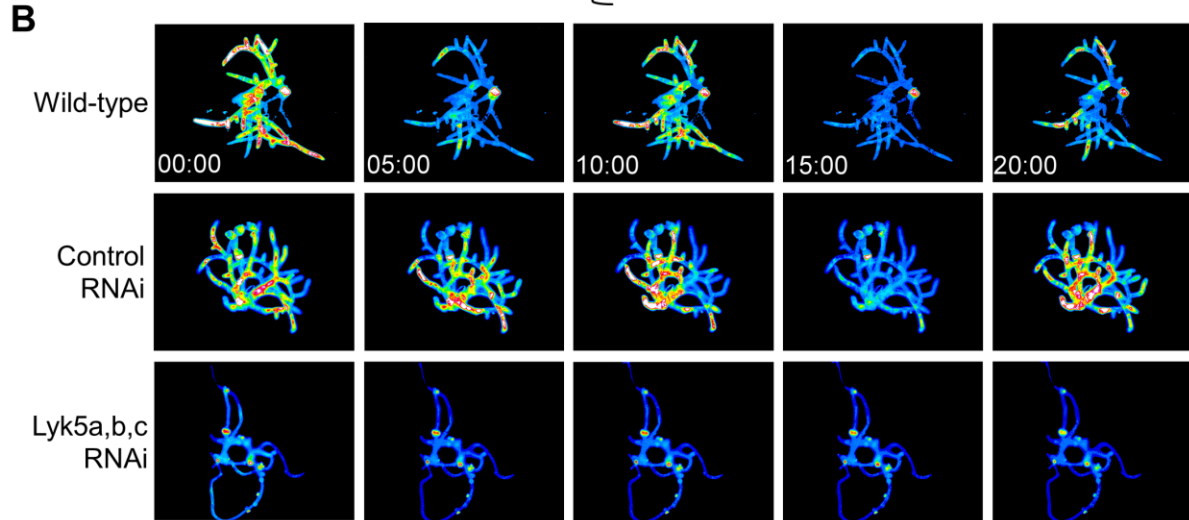
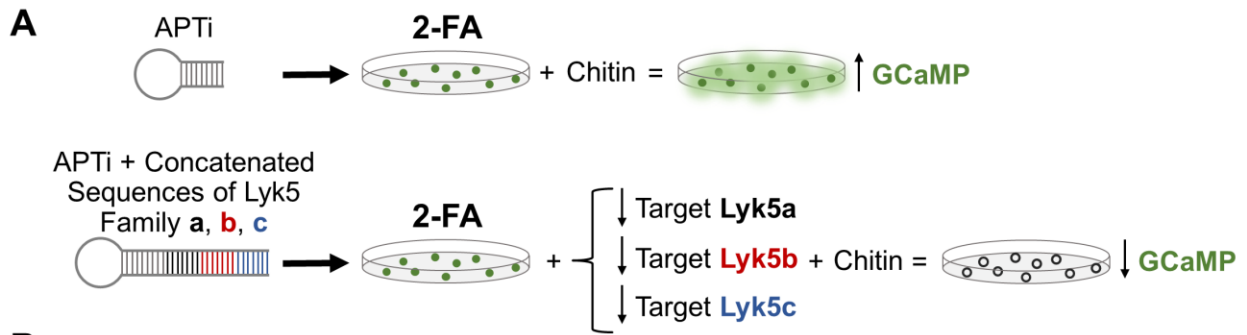


**Figure 2.7** Simultaneous silencing of the Lyk5 gene family with APTi abolishes chitin-induced calcium transients. A, Schematic of APTi-based functional assay of Lyk5. Control RNAi plants treated with chitin elicit calcium transients, visualized with GCaMP. Simultaneous depletion of the Lyk5 receptor family (a,b,c) using APTi desensitizes the plants to chitin, resulting in loss of calcium spikes. B, 8-day old plants treated with 20 mg/mL chitin oligosaccharides. Time stamps are min:sec. Dark blue indicates plant autofluorescence, where aqua to red reflects an increase of calcium signal. “Wild-type” represents GCaMP6 in the Gransden background. C, Dose response of *P. patens*’ calcium signal to chitin application for control RNAi plants and plants transformed with an APTi construct targeting all three Lyk5 genes. Time-averaged mean gray value (left plot) and the standard deviation (Std. Dev.) of the time-averaged mean gray value (right plot) are normalized by  $(F - F_0) / F_0$  for both conditions. All data points are the mean of at least three plants pooled from three independent experiments. D, Characterization of calcium transients within a 30 minute observation period, as in A, across multiple concentrations of chitin. All points represents an individual plant, pooled across three independent experiments. Bars represent the mean  $\pm$  the standard error of the mean. Each condition was compared against itself across concentrations, with an asterisk representing a statistical difference between that condition and its corresponding water control. Statistics were performed with a Kruskal-Wallis one-way non-parametric ANOVA, followed by a Dunn’s multiple comparisons test. \* $p < 0.001$

Our preliminary experiments silencing only two of the three Lyk5 genes showed calcium spikes in response to chitin, suggesting we are targeting all three genes with our Lyk5-RNAi construct. Additionally, as only the double knockout *lyk4 lyk5* mutant in *Arabidopsis* loses all chitin sensitivity (Cao et al., 2014), we conclude our APTi-based silencing of the Lyk5 family is functioning with high efficiency in order to phenocopy a double knockout mutant in *Arabidopsis*. Importantly, these results elucidate functional homology of the LYK4/5 genes between *Arabidopsis* and *P. patens*, whereby Lyk5 functions at the level of chitin perception. Previous work demonstrated that *P. patens* CERK1 rescues the *Arabidopsis cerk1* mutant (Bressendorff et al., 2016), strongly supporting a conserved mechanism of chitin sensing. Altogether, our findings demonstrate the robustness and versatility of our novel APTi system for mutant isolation and characterization.

## 2.4 Discussion

RNAi offers an invaluable complement to traditional gene knockout studies. However, substantive advancements in RNAi methods are trailing the explosion of CRISPR/Cas-based technologies. Here we established the first survival-based RNAi methodology that robustly selects for actively silencing plants. We accomplished this by engineering vectors that elicit a pro-survival response when processed by the organism's endogenous RNAi machinery. Using the previously characterized *myosin XI* mutant in *P. patens* as an initial case study, we showed that in tandem fusion of a myosin XI target with the pro-survival sequence resulted in potent selection of morphologically mutant plants. We demonstrated that surviving plants actively targeting myosin XI through our novel vectors contained approximately 7% of normal myosin XI protein abundance. Additionally, using APTi facilitated the silencing of the Lyk5 family and resulted in moss plants completely insensitive to chitin-induced calcium spikes. To our knowledge, this is the first evidence demonstrating the function of Lyk5 in *P. patens*, and supports the notion of conservation in fungal perception between vascular and non-vascular plants. Our APTi technology represents a dramatic improvement in silencing efficacy and experimental implementation over previous RNAi methods.

RNAi has been extensively employed in the model moss *Physcomitrella patens* for both discovery and validation of gene function (Vidali et al., 2007a; Augustine et al., 2008; Prigge et al., 2010; Vidali et al., 2010a; Augustine et al., 2011; Wu et al., 2011b; Miki et al., 2015; Bascom et al., 2019b). We attribute the popularity of dsRNA-based RNAi in *P. patens* to a method that uses an internal fluorescent reporter of RNAi to obtain results in one week (Bezanilla et al., 2003a). We sought to fundamentally improve upon RNAi

reporters by creating a reporter where survival itself is indicative of active silencing. We demonstrated the feasibility and effectiveness of this approach by silencing the APT gene in the presence of 2-FA in the medium. Furthermore, we engineered two plasmids that facilitate insertion of any target of interest in tandem with the APT-silencing sequence. We call this novel approach APT-based RNA interference, or APTi. To achieve rapid phenotyping using APTi, all experiments were performed in transient. Modifications of the APTi plasmids to promote stable integration and induction of the silencing cassette represent an important area of future work. Both APTi plasmids and the myosin XI-RNAi plasmid are publicly available from the plasmid repository Addgene.

We obtained potent positive selection of actively silencing plants in *Physcomitrella patens* by engineering RNAi vectors that exploit the function of the APT gene. However, the physiological consequences of APT silencing remain in question. Although a salvage enzyme, APT's function presents a more energetically efficient means of nucleotide production than *de novo* synthesis (Ashihara et al., 2018). Consequently, knockouts of APT in vascular plants demonstrate severe defects in pollen germination and pollen tube growth, presumably a result of impairing the energy-intensive fast growth of the pollen tube (Moffatt and Somerville, 1988; Zhou et al., 2006). Interestingly, an alternative mutant allele of APT that results in partial reduction of APT activity imparts enhanced growth and stress tolerance (Sukrong et al., 2012). We suspect this hypomorphic allele better represents the internal state of our APT-silenced plants. Taken together with our observations of APT-silencing plants reproducing results achieved with an orthogonal RNAi system and APT-RNAi plants displaying calcium spikes consistent with wild-type,

we conclude the reduction of APT results in no clear physiological defects within the scope of our assays.

We expect our APTi strategy to be applicable to other organisms given the ubiquity of the APT gene (Schaff, 1994). Like other organisms, such as in humans, *Physcomitrella patens* contains only one copy of APT making it especially amenable to the APTi strategy as we showed. Interestingly, the vascular plant *Arabidopsis thaliana* contains five APT genes (Allen et al., 2002). We suspect APTi could be applied in *A. thaliana* by constructing an APT-silencing module comprised of concatenated sequences targeting specific isoforms. Additional work is necessary to translate to other systems, but we submit that our efforts establishing APTi in *P. patens* will greatly benefit the community in understanding fundamental and conserved biological processes (Orr et al., 2020a).

Previous work using the fluorescent reporter-based RNAi identified silencing plants based on loss of fluorescence (Bezanilla et al., 2003a). However, slight reduction in fluorescence confounded interpretation because it could be attributed to natural variation in the reporter signal or reflect a real, but modest, silencing effect. Furthermore, in our hands we observed spontaneous loss of reporter signal in the moss reporter line over long periods of continuous propagation. Without careful observation and subcloning to remove chimeric reporter cultures, a researcher could inadvertently conclude silencing when none is occurring. Our APTi system simultaneously removes the requirement of a dedicated moss reporter line and dismisses any ambiguity inherent to a continuous reporter signal. We demonstrated the utility of this advancement in our investigation of Lyk5 by transforming our APTi-based construct into a moss line expressing the calcium sensor GCaMP6f (Galotto et al., 2020). This saved considerable time, as the previous

RNAi methodology would require creation of a new transgenic line that contains the RNAi GFP reporter and a non-GFP-based calcium sensor.

Interestingly, prior RNAi methods can result in background plants that survive antibiotic selection for the plasmid containing the RNAi transgene but do not silence the reporter. This is likely a result of transcriptional gene silencing, whereby the plant rescues itself from RNAi transgene expression but expression of the independently regulated antibiotic resistance is unmodified (Morel et al., 2000; Fusaro et al., 2006; Small, 2007). We hypothesize our method enhances silencing efficiency by engineering a fitness punishment for the organism to silence the RNAi transgene. To this end, with APTi survival on 2-FA is directly coupled to expression of the APT-RNAi transgene. Therefore, the organism cannot survive if it silences the expression of the RNAi cassette, thus ensuring expression of the APT + gene target hairpin. Although we did not determine the extent of APT silencing, we know the reduction is sufficient to promote survival on 2-FA and produce a 90% reduction of a fused target, myosin XI, or complete loss of detectable calcium signal when all three Lyk5 genes are targeted.

We speculated that the enhanced fitness benefit imposed by our APTi system will result in more consistent and potent silencing efficiencies of target genes. Consistent with this, we observed a homogenous population of mutants evidenced by a 90% reduction of endogenous myosin XI and total loss of chitin sensitivity when targeting myosin XI(a,b) and Lyk5(a,b,c), respectively. APTi offers a noticeably higher silencing efficacy when compared to previous reports using dsRNA and GFP-based reporters in *P. patens* (Vidali et al., 2007a; Vidali et al., 2010a; Nakaoka et al., 2012). Importantly, previous reports could only estimate protein silencing based on a small subset of individual plants

deliberately chosen by the experimenter, which may not accurately reflect the average silencing effect (Vidali et al., 2007a; Augustine et al., 2008; Vidali et al., 2009; Vidali et al., 2010a). This microscope-based methodology was required because mutants resulting in small morphologies failed to yield adequate plant material for immunoblots, and were surrounded by non-silencing background plants. We demonstrated that APTi's positive selection enables simple harvesting of the entire plate that can be easily scaled for reproducible protein quantitation. Based on our observed myosin XI knockdown, our APTi silencing efficacy is comparable to the most effective amiRNAs (Zhang et al., 2018), but without the need for prior engineering and screening of multiple amiRNAs. Furthermore, performing our Lyk5 functional assay with prior GFP-based RNAi would require an additional time-consuming and tedious pre-screening step, where actively silencing plants are physically isolated from the non-silencing background. With APTi, any surviving plant can be chosen at random for functional analysis, greatly enhancing the throughput and likely the consistency of the results.

We showed that the APTi system is well suited for high-throughput phenotyping. We fully anticipate this area to be iteratively improved, not just with respect to the volume of acquisition but with increased computational sophistication. The large obtainable data sets are ripe for both classic exploratory data methods and cutting-edge deep learning techniques. For example, we analyzed living plants by first segmenting the images by traditional thresholding. We then filtered and classified the hundreds of plants based on a characteristic biological feature, chlorophyll autofluorescence, which we derived from the Control-RNAi dying population. Although less intuitive, deep-learning offers the

possibility of automating image segmentation and classification, perhaps resulting in discovery of novel mutant features (Moen et al., 2019).

## **2.5 Conclusions**

This work represents a fundamental transition from visual screening for RNAi plants to positive selection of actively silencing plants. We achieved this by engineering vectors that produce a single hairpin RNA targeting the APT gene and any other genes of interest in tandem. This results in effective isolation of all surviving plants undergoing RNAi of the target gene when grown in the presence of 2-FA. Importantly, the efficacy of gene-silencing was consistently greater with the APTi system, maximal 93% reduction of target protein, than previous reports silencing the same myosin XI genes using a fluorescent screening method. Additionally, with APTi we simultaneously silenced the Lyk5 gene family (a,b,c) and demonstrated their requirement for perception of chitin oligosaccharides in *P. patens*. We believe our APTi system provides a flexible, fast, and effective platform with unprecedented low background and variability to facilitate high-throughput characterization for loss-of-function mutants.

## **2.6 Materials and Methods**

### **2.6.1 Plant Materials and Culture Conditions**

Three *Physcomitrella patens* lines were used in this study: (1) NLS4 (Bezanilla et al., 2003a) in Figure 2.1a; (2) GCaMP6f called “wild-type” in Figure 2.7 (Galotto et al., 2020); (3) “wild-type” Gransden (Ashton et al., 1979) all other experiments. All lines were cultured as previously described (Vidali et al., 2007a). In brief, tissue was propagated weekly by homogenization and transferred to solid PpNH<sub>4</sub> medium overlaid with

cellophane. Cultures were grown at 25°C under long-day light (90  $\mu\text{mol m}^{-2} \text{s}^{-1}$ ) conditions (16 h : 8 h, light : dark).

### 2.6.2 APT-based RNAi Construct Design

The APT transcript fragment (Phytozome: Pp3c8\_16590) containing 5'UTR and coding sequence (CDS) was amplified by PCR with forward (APT\_BSK\_F) and reverse (APT\_BSK\_R) primers and cloned into pBlueScript K+ using restriction enzymes *SacI/EcoRV* (generating the APT pBSK+ plasmid). The pUGGi Gateway cassette and loop domain lacking the GUS regions was amplified in two pieces using PCR with primer sets Gateway1\_F/R and Gateway2\_F /R (both reactions at 60°C, 2min elongation), and both fragments were ligated individually into pBlueScript K+ (generating the Gateway F pBSK+ and Gateway R pBSK+ plasmids). The pUGGi loop was amplified by PCR with primers Loop\_F/R and inserted into pBlueScript K+ (generating the Loop pBSK+ plasmid). The APT and Loop pBSK+ constructs were transformed into DH5 $\alpha$  *E. coli*, whereas both Gateway pBSK constructs were transformed into ccdB *E. coli*. All constructs were blue-screened for successful clones by plating transformants on LB+Carb+Chlor plates and adding 40 $\mu\text{L}$  each of IPTG and X-Gal. Next, using the *SacI/XhoI* restriction sites the Gateway F fragment was inserted into the Gateway R pBSK+ backbone, generating the complete Gateway pBSK+ plasmid. Importantly, this construct contains the entire loop region derived from pUGGi, as the two intermediate Gateway constructs discussed above each contain half of the loop region. It was necessary to isolate the pUGGi Loop in its own plasmid because we wished to create an additional control plasmid lacking the Gateway cassettes.

The first APT fragment was then excised from APT pBSK+ using *HindIII/SwaI*, then transferred into the Gateway pBSK+ plasmid, cut with *HindIII/PmeI* (generating Gateway-1APT pBSK+). Next, the second APT fragment was excised from APT pBSK+ and transferred into the Gateway-1APT pBSK+ plasmid using *SacI/SwaI* sites (generating Gateway-2APT pBSK+). The Gateway-2APT fragment was digested then ligated into the pUGGi backbone using *SacI/KpnI* sites, generating the pGAPi plasmid. To generate our positive control plasmid without Gateway sites, two APT fragments were inserted into the Loop pBSK+ plasmid using the same procedure as described above—first by *HindIII/SwaI* and *HindIII/PmeI* sites, then by *SacI/SwaI* sites - producing the Loop-2APT pBSK+ plasmid. Then the Loop-2APT fragment was cloned into the pUGGi backbone using *SacI/KpnI* sites, generating the pAPi plasmid. At all points in this process where new plasmids were made by restriction-based cloning, those plasmids were confirmed by restriction and sequence analysis.

The myoUTi:pGAPi construct was created by extracting the previously published, concatenated 5' UTR targeting sequences (Vidali et al., 2010a) from its RNAi destination vector via a Gateway® BP reaction, then inserted into our new pGAPi construct via a Gateway® LR reaction. The transient myosin XI-RNAi phenotype was rescued by expressing the myosin XIa CDS (Vidali et al., 2010a). All three APTi plasmids are publicly available from Addgene (pGAPi #127547; pAPi #127548; myoUTi:pGAPi #127549) and sequences are also available at Genbank (pGAPi = MK975250; pAPi = MK975251; myoUTi:pGAPi = MK975252).

### **2.6.3 APTi Phenotyping Assay**

One week-old moss was protoplasted and transformed as described (Liu and Vidali, 2011), with transformed protoplasts being plated at  $1.4 \times 10^5$  protoplasts per 100 mm petri dish of PRMB in liquid plating medium. Each condition was plated in at least duplicate, with the myoUTi condition being plated in triplicate to allow enough plant material of the mutant plants to be harvested for immunoblotting and imaging. Four days post-transformation the cellophanes of each plate were transferred to growth medium (PpNH<sub>4</sub>) supplemented with 1.25 µg/mL 2-fluoradenine from a 5 mg/mL in DMSO stock (Oakwood Chemical). As mentioned previously, we emphasize that each lab should first optimize the 2-FA selection concentration, as our results were all obtained using a single lot of 2-FA from Oakwood Chemical, SC, USA.

Eight days post-transformation plants were stained with 10 µg/mL calcofluor from a 1 mg/mL in H<sub>2</sub>O stock (Fluorescent Brightener 28, Sigma) and imaged with a 10X A-Plan (0.25 NA) objective of an epifluorescent microscope (Zeiss Axiovert 200M) coupled to a CCD camera (Zeiss AxioCam MRm). This microscope was equipped with an automated stage and integrated with the AxioVision software through the MosaicX module, enabling precise acquisition, tiling, and stitching of individual images to create a large composite. Our composite images contained 12x12 individual images, acquired with a 15% overlap. Each individual image consisted of two channels, the calcofluor and chlorophyll signals. The chlorophyll channel was acquired with a 480/40 bandpass excitation, a 505 longpass dichroic mirror, and a 510 long-pass emission filter cube and with a fixed 150 ms exposure for all experiments. The calcofluor signal was acquired with

a standard DAPI filter and automatically adjusted for each experiment to maximize contrast.

Stitched images were first processed and segmented using a custom-written ImageJ macro. Our macro only discarded segmented objects approximately the size of two adjoining protoplasts or smaller, as to not bias against the discovery of small mutants and remove non-surviving protoplasts. Each segmented image was visually inspected for overlapping or truncated plants, and if present they were discarded from further analysis. Subsequent filtering of alive plants and visualization of the data was performed using MATLAB (MathWorks). Statistical testing (one way ANOVA-Tukey) was performed with GraphPad Prism.

#### **2.6.4 Analysis of Myosin XI Protein Abundance**

Eight days post-transformation, all tissue was harvested by scraping, flash-frozen in liquid nitrogen, and stored at  $-80^{\circ}\text{C}$ . To create protein extracts, the frozen tissue was ground to a powder in liquid nitrogen, then resuspended in extraction buffer (250mM Sucrose, 20mM EGTA, 50mM PIPES, 150mM NaCl, 60mM  $\text{MgCl}_2$ , and 1% w/v Casein) supplemented with fresh DTT (2mM final) and protease inhibitors. The powder from the pAPi condition was resuspended in 300  $\mu\text{l}$ , whereas the myoUTi and rescue conditions were always resuspended in 200  $\mu\text{l}$  extraction buffer. Extracts were vortexed for 15 seconds, then placed on ice for 30 seconds, with this repeated twice more. Extracts were then spun at 13,000 RPM for 10 mins at  $4^{\circ}\text{C}$ , followed by removal of 175  $\mu\text{l}$  of the clarified supernatant; 120  $\mu\text{l}$  of extract was immediately combined with SDS loading buffer and boiled, then stored at  $-80^{\circ}\text{C}$ . The remaining extract was used for total protein determination using the Bradford microplate microassay procedure (Bio-Rad).

To probe myosin XI protein directly, we developed an antibody against a 6xHis fusion of the *P. patens* myosin XIa-CCT (Capralogics, Inc. Hardwick, MA). We used an antibody against alpha tubulin as our loading control (DSHB: AA4.3). We determined the approximate linear range of both antibodies by first loading 1-20 µg of total protein from a pAPi treated moss extract on a 4-12% Bis-Tris SDS-PAGE gel (ThermoFisher). Protein was then transferred to nitrocellulose overnight at 4°C, followed by blocking with 5% milk in TBS-T at room temperature for 1hr. The nitrocellulose was cut at the 80 kDa marker, with the higher molecular weight piece incubated with myosin XIa-CCT primary antibody (1:10,000) and the α-tubulin (0.5 µg/ml final) incubated with the lower molecular weight fragment for 1hr at room temperature. Following primary incubation, blots were washed three times in TBS-T, incubated in secondary antibody (goat anti-rabbit for XIa-CCT, goat anti-mouse for α-tubulin) at 1:100,000 dilution for 1hr at room temperature, then washed a final three times. Blots were developed using homemade ECL reagent and chemiluminescent images were acquired using an Azure 600 (Azure Biosystems). Densitometry was performed using ImageJ (Schneider et al., 2012) to allow comparison of relative protein abundance.

### **2.6.5 Lyk5-RNAi Construct Design and Functional Assay**

To disrupt the expression of Lyk5 genes in *P. patens*, an RNA interference plasmid was constructed. The first 414 bp of Lyk5a and 418 bp of Lyk5b were amplified using specific primers (Table S1) with the Phusion polymerase (ThermoFisher). Then, both fragments were joined by overlapping PCR, and the 0.8 kb fragment was gel purified (NucleoSpin® Gel and PCR Clean-up, Macherey-Nagel) and inserted in the entry vector pDONR207 via a BP reaction (Thermo). To insert the remaining Lyk5 gene, primers were designed for

Lyk5c (Table 2.1) that amplifies a fragment of exon 1. The corresponding 0.4 kb amplicon was gel purified (Zymogen Clean Gel DNA Recovery Kit) and inserted into pDONR207-Lyk5a,b via BamHI. Successful pENT-Lyk5a,b,c clones were identified through restriction analysis and sequencing. The concatenated Lyk5a,b,c target sequence was inserted into pGAPi via an LR reaction (ThermoFisher) between pGAPi and pENT-Lyk5a,b,c, yielding Lyk5-RNAi. The Lyk5-RNAi construct was sequence verified. Transient transformation and APT selection were performed as described above.

Calcium imaging and analysis were performed as previously described (Galotto et al., 2020). In brief, plants were mounted on an agar pad containing serial dilutions of chitin oligosaccharides, starting at 20 mg/mL (Tokyo Chemical Industry-TCI), or water and imaged with a Zeiss Axio Observer.A1 motorized microscope using a 10x objective lens (NA 0.25). The internal calcium sensor was excited with a mercury lamp X-Cite series 120 PC EXFO, and individual plant images were acquired every 30 sec for 30 min within 10 min of initial chitin exposure. Analysis of the calcium time series data was performed using ImageJ and RStudio. Microscope drift was corrected in ImageJ using the 'StackReg' plugin (Thevenaz et al., 1998). Next, the area around the plant was selected and the background was cropped. Then our macro applied, for each frame in the series, a thresholding function that equalized the images and masked the area around the plant; the masked images were used to analyze the Ca<sup>2+</sup> peaks in chitin treated plants. In addition, the ImageJ macro recorded the mean gray value of each image. The mean gray values for a time-series were averaged (calcium levels) and the standard deviation of the average calculated (calcium fluctuations). The dose-response was calculated in GraphPad Prism by plotting the time-averaged values and standard deviation for each

concentration of chitin oligosaccharides. To estimate the number of calcium peaks and their frequency, the masked images produced by our ImageJ macro were analyzed using MATLAB. The script uses a rolling 3x3 pixel grid to detect the position of the plant throughout the video. For each frame, the grid scans through the image and records the pixel value of a 3x3 pixel area. Only the grids with positive values are considered as being part of a plant. When all the positive pixels are identified, the MATLAB script computes the mean of the pixel values and calculates the standard deviation of that mean. Once the mean of the pixel values is obtained, the script finds the Ca<sup>2+</sup> peaks. A signal is considered a peak when its intensity is greater than one standard deviation multiplied by 0.345, a constant, from the mean gray value of the plant. Once the peak detection was completed, the period between peaks was measured with a built-in MATLAB function 'findpeaks.' This analysis was repeated for each plant.

<b>Primer Name</b>	<b>Primer Sequence</b>
APT_BSK_F	CATCATGAGCTCAAGCTTTACCGTGCGCCACTTGAC
APT_BSK_R	CATCATATTTAAATACCTCGAGCTTCAATTCCCAC
Gateway1_F	CATCATGAGCTCATTAAATCCACTTTGTACAAGAAAGCTG
Gateway1_R	CATCATCTCGAGGGTTCGTTGGCAATACTCCAC
Gateway2_R	CATCATGGTACCAAGCTTGTTAAACCCACTTTGTACAAGAAAGCTG
Gateway2_F	CATCATCTCGAGGGATACCCGTCCGCAAGTG
Loop_F	CATCATGAGCTCATTAAATTGATTACGTACAGATGAACATGG
Loop_R	CATCATGGTACCAAGCTTGTTAAACTGATTACGTACCTAGGCATCA
UbiProSeq_F	CTTTTGTGCGATGCTCACCCTG
LinkerSeqF	TGATTACGTACCTAGGCATCA
NosTermSeqR	CCGGCAACAGGATTCAATCTT
Lyk5cF	AGGAGGATCCATGTCAATATCAGAACTGAAATCTCAG
Lyk5cR	ACTAGGATCCAACCACATTAGACGTAGGCGC

**Table 1** List of primers used for vector construction and sequence verification.

## **Chapter 3 : RabE and its Interaction with Myosin XI are Essential for Cell Polarization and Growth**

---

### 3.1 Abstract

The fundamental process of polarized exocytosis requires the interconnected activity of molecular motors trafficking vesicular cargo within a dynamic cytoskeletal network. In plants, few mechanistic details are known about how molecular motors, such as myosin XI, associate with their secretory cargo to support the ubiquitous processes of polarized growth and cell division. Here, we used live-cell imaging coupled with targeted gene knockouts and a high-throughput RNA interference assay, thereby enabling the first characterization of the loss of RabE function. Additionally, yeast two-hybrid and subsequent *in silico* structural prediction uncovered a specific interaction between RabE and myosin XI that is conserved between *P. patens* and *A. thaliana*. *In planta*, RabE co-localizes with myosin XI at sites of active exocytosis, and at the growing tip both proteins are spatiotemporally coupled. RabE is required for normal plant growth in *P. patens* and the *rabE* and *myosin XI* phenotypes are rescued by *A. thaliana*'s RabE1c and myosin XI-K/E, respectively. Both cargo-binding domains of *P. patens* myosin XI and *A. thaliana* myosin XI-K interact with *P. patens* RabE14, and the interaction is specifically mediated by residue V1422 in myosin XI of *P. patens*. Furthermore, this interaction is required for polarized cell growth. Our results suggest the interaction of RabE and myosin XI is a conserved feature of polarized cell growth in plants.

### 3.2 Introduction

Polarized exocytosis requires precisely coordinated vesicle trafficking to support the essential function of polarized growth across eukaryotes, in addition to more plant-specific functions such as pathogen defense and cell wall biogenesis (Robatzek, 2007; Bove et al., 2008; Ebine and Ueda, 2015; Bibeau et al., 2018a). Plant polarized growth, or tip growth, exploits turgor pressure and active transport of secretory vesicles to drive rapid anisotropic expansion (Hepler et al., 2001; McKenna et al., 2009). At present, a mechanistic understanding of how secretory vesicles are trafficked for exocytosis in plants is lacking.

Polarized delivery of secretory vesicles is the rate limiting step for tip-growth in plants, and is dependent upon the molecular motor myosin XI (Vidali et al., 2010b; Madison and Nebenfuhr, 2013; Rounds and Bezanilla, 2013). Our traditional understanding of active transport interprets myosin XI as providing the mechanical force to translocate cargo on F-actin cables (Campas and Mahadevan, 2009; Moscatelli et al., 2012), since diffusion alone is insufficient to support the rate of polarized growth (Bibeau et al., 2018a). An emerging perspective proposes myosin and its vesicular cargo as a fluid organizing center of actin nucleation and cargo transport (Schuh, 2011; Furt et al., 2013; Pylypenko et al., 2016; Bibeau et al., 2020). Across the plant kingdom, myosin XI is observed at regions of active exocytosis and is essential for proper movement of organelles and the organization of secretory vesicles at the growing cell tip (Ojangu et al., 2007; Peremyslov et al., 2008; Vidali et al., 2010b; Peremyslov et al., 2012; Park and Nebenfuhr, 2013; Bibeau et al., 2020; Orr et al., 2020a). Additionally, work with chimeric myosin XIs established a strong correlation between myosin XI velocity and cell growth

(Tominaga et al., 2013). Presumably, the relationship between myosin XI velocity and cell growth is a consequence of augmented delivery of myosin XI cargo; however, a direct interaction with myosin XI and its secretory cargo remained elusive.

At present, there exists a pronounced disconnect between previously identified myosin XI interactors and our understanding of eukaryotic polarized growth. A plant-specific myosin XI interactor, called MyoB (Peremyslov et al., 2013), contributes to bulk cytoplasmic streaming but fails to colocalize with any known markers (Peremyslov et al., 2015; Kurth et al., 2017). Additionally, MyoB is noticeably absent at the growing cell plate where myosin XI (Abu-Abied et al., 2018; Sun et al., 2018), Rab GTPases (Chow et al., 2008; Ahn et al., 2013), and multisubunit tethering complexes (Rybak et al., 2014) are present. The non-vascular plant *Physcomitrella patens* displays no, or undetectably low, cytoplasmic streaming. Despite this, *P. patens* grows polarized filaments that contain a similar complement of proteins (myosin XI, MyoB, Rab GTPases, etc.) with typically fewer isoforms (13 myosin XI genes in *A. thaliana*, 2 in *P. patens*) than seed plants. This reduced complexity motivates the moss *Physcomitrella patens* as an attractive model to investigate heretofore unidentified myosin XI interactors necessary for polarized growth without background cytoplasmic movement. Observations of robust correlations between myosin XI and vesicles in *P. patens* (Furt et al., 2013; Bibeau et al., 2018b) and well-characterized homologous myosin V-Rab interactions from yeast to human (Hammer and Sellers, 2012), strongly suggests the presence of a homologous myosin-Rab interaction in plants to mediate vesicle association and transport.

Myosin XI is presumed homologous to the class V myosins, such as Myo2 from *Saccharomyces cerevisiae* (Li and Nebenführ, 2007), but functional evidence of

conserved interactions is lacking. In yeast, Myo2's C-terminal globular tail sequentially interacts with vesicle-localized Rab GTPases Ypt31/32 and Sec4 to faithfully transport vesicles to the growing bud tip and sites of cytokinesis in a stereotypical "transport cascade" (Schott et al., 1999; Pashkova et al., 2006; Lipatova et al., 2008; Jin et al., 2011; Donovan and Bretscher, 2012). Rab GTPases localize to discrete endomembrane compartments and discriminate between effectors by undergoing dynamic structural rearrangements in a nucleotide-dependent manner (Khan and Menetrey, 2013; Pfeffer, 2017). Myo2 and Sec4 interact and localize to secretory vesicles, and both interact with the plasma membrane localized, hetero-octameric tethering complex called exocyst (Jin et al., 2011; Donovan and Bretscher, 2012). While the precise coordination and/or exclusivity of the interactions between myosin, Rabs, and the exocyst is unclear, together these proteins compose the terminal step of the Rab-Myosin transport cascade immediately preceding exocytosis (Lepore et al., 2018). Sec4 is homologous to the Rab8 subfamily in mammals, and despite evolutionary distance the subfamily's interaction with class V myosin is conserved from yeast to human (Welz and Kerkhoff, 2017). An analogous Rab cascade in mammalian cells (Knodler et al., 2010; Mizuno-Yamasaki et al., 2012), suggests the presence of a conserved eukaryotic polarized exocytosis mechanism.

The plant RabE subfamily is homologous at the amino acid level to Sec4/Rab8 (Rutherford and Moore, 2002), implying the presence of an analogous Rab-mediated transport model of secretory vesicles by myosin XI. Both functional and live-cell imaging studies demonstrated RabE's involvement in anterograde transport to the plasma membrane from the Golgi, and a general requirement for plant growth and cell division

(Zheng et al., 2005; Speth et al., 2009; Ahn et al., 2013). Recently, RabE was identified as functioning in concert with both the SCD and exocyst complexes (Mayers et al., 2017b). The SCD complex displays putative GEF activity for RabE, thereby suggesting an activated RabE in proximity to the exocyst. This finding tentatively places RabE in a transport pathway similar to Myo2/Sec4/exocyst (Heider and Munson, 2012); however, the presence of a molecular motor to actively transport secretory cargo in plants remained elusive.

Here, we show through yeast two-hybrid, bioinformatic, and *in vivo* analyses that myosin XI specifically interacts through its globular tail domain with a RabE GTPase enriched at sites of exocytosis, and disruption of the interaction results in a concomitant impairment of polarized growth. Furthermore, we demonstrated RabE's requirement for plant growth and found that *A. thaliana* RabE rescues the *rabE* phenotype in *P. patens*.

### **3.3 Results**

#### **3.3.1 RabE Localizes to Sites of Polarized Secretion and Colocalizes with Myosin XI**

We hypothesized a homologous polarized trafficking mechanism exists between opisthokonts and plants, whereby plant specific myosin XI associates with RabE to support polarized growth. Previous work in plants implicates RabE in polarized exocytosis (Zheng et al., 2005; Speth et al., 2009; Ahn et al., 2013; Mayers et al., 2017b), and work with homologous Rabs in yeast and mammals directly couples Rabs to the motor protein myosin V to promote polarized vesicle deposition (Jin et al., 2011; Donovan and Bretscher, 2012). To determine the subcellular localization of RabE, and test colocalization with myosin XI, we generated a constitutive expression construct of

3mCherry-RabE14 (Cherry-RabE14) and transformed this into a *P. patens* line with myosin XI tagged with 3xmEGFP at the endogenous locus (Sun et al., 2018). Transgenic plants that expressed the fluorescent RabE protein and showed no growth phenotype were used for subsequent analysis.

We observed, using confocal laser scanning microscopy, that Cherry-RabE14 localizes to discrete, cytosolic compartments, and predominantly accumulates at the extreme apex of growing caulonemal cells (Figure 3.1a, Figure 3.2a). Furthermore, both myosin XI and RabE colocalized at the growing tip (Figure 3.1a). Importantly, myosin XI and RabE show synchronized stochastic fluctuations of their fluorescent intensity over time within the apex of the growing moss cell (Figure 3.1b). Cross-correlation analysis of the myosin XI and RabE time series reveals that these two proteins are in-phase (Figure 3.1c). This result is commensurate with our previous data demonstrating a tight spatiotemporal correlation with myosin XI and VAMP-labeled vesicles (Furt et al., 2013), thus supporting the inference that RabE is at least partially vesicle-localized. We investigated the subcellular localization of another RabE isoform, RabE12, and found similar dynamic localization to the growing tip (Figure 3.2b), suggesting functional redundancy. The strong spatial and temporal correlation between myosin XI and RabE is consistent with our hypothesis that RabE and myosin XI interact to drive polarized growth. However, we cannot conclude with this approach whether they interact directly or indirectly.

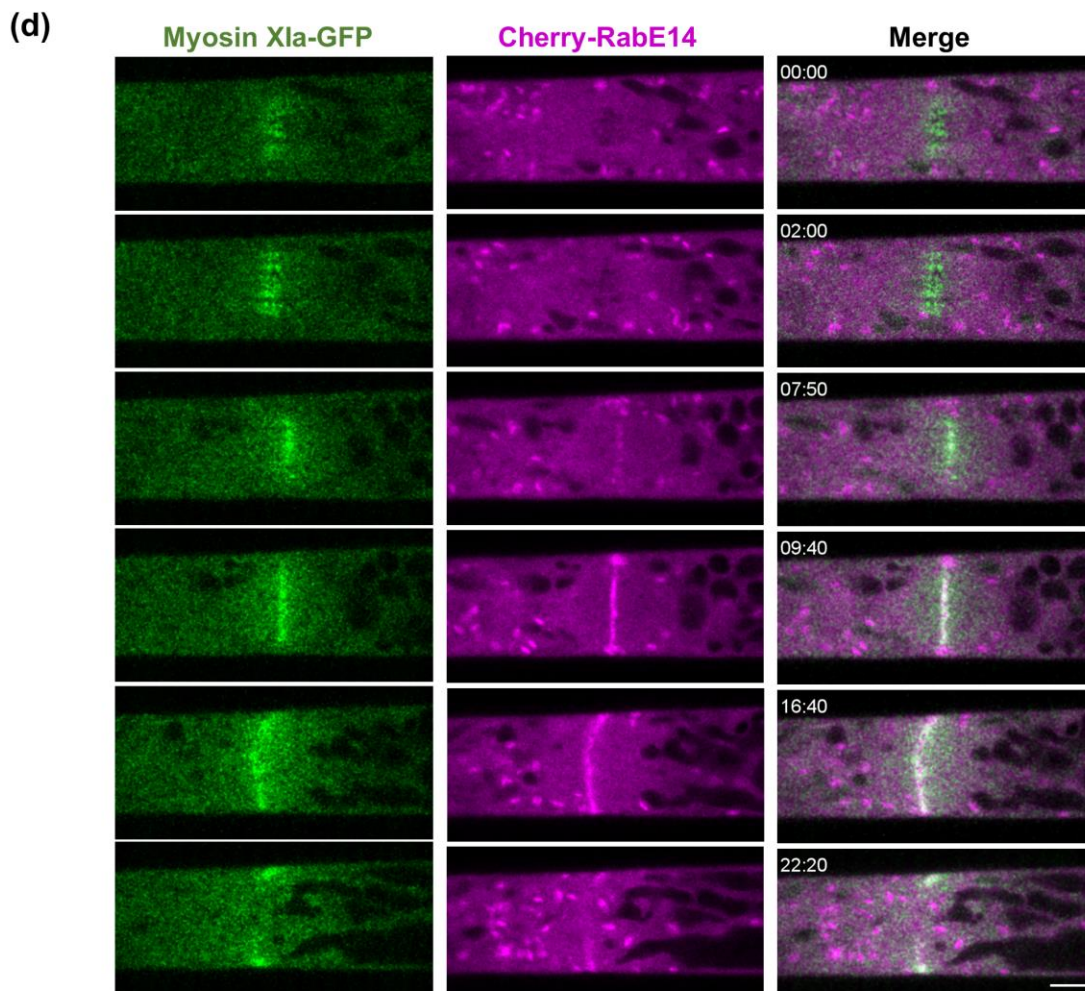
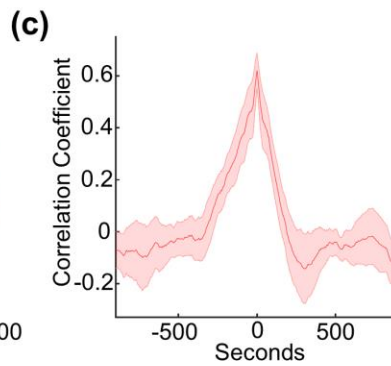
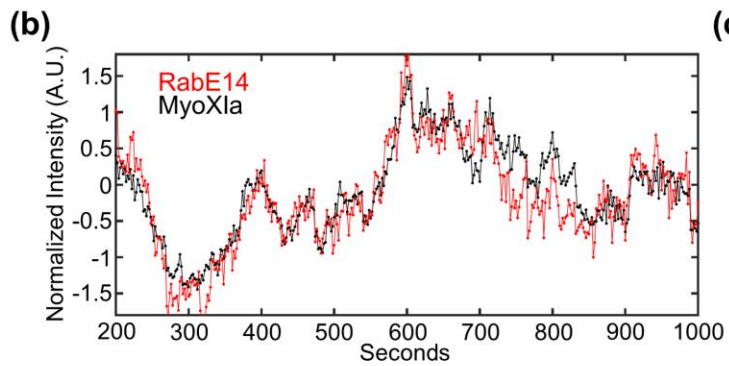
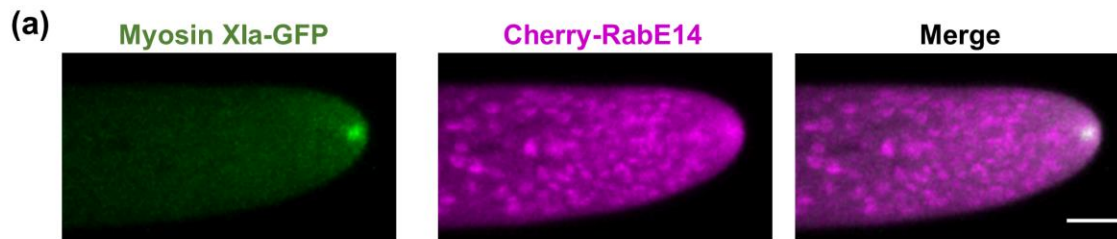


**Figure 3.1** RabE co-localizes with myosin XI at sites of polarized exocytosis. A, Subcellular localization of 3xmCherry-RabE14 and MyosinXIa-3xmEGFP by confocal microscopy. Images are maximum projections of 8 confocal slices at 1  $\mu\text{m}$  spacing to visualize the apical volume. Scale bars are 5  $\mu\text{m}$ . B, Intensity fluctuations of myosin XI and RabE at the apex of the growing cell. Intensity values were obtained through kymograph analysis of time series video. C, Maximum correlation coefficient of myosin XI and RabE intensity fluctuations. Solid line indicates the average correlation coefficient of 5 cells. The shaded region represents the standard error of the mean. Scale bar, 5  $\mu\text{m}$ . D, An apical caulonemal cell of the double myosinXI-GFP and Cherry-RabE14 line was imaged during cell division approximately 1-minute post nuclear envelope breakdown. Scale bar, 5  $\mu\text{m}$ .

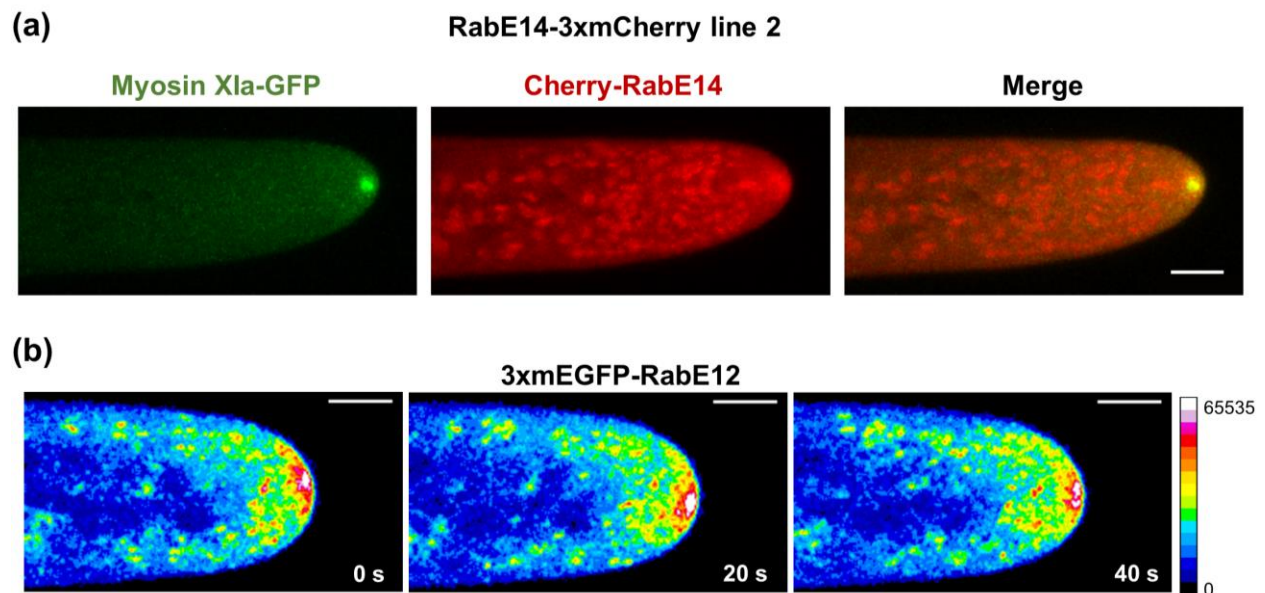


**Figure 3.2** Subcellular Localization of RabE12 and Independent RabE14 Lines. A, Subcellular localization of 3xmEGFP-RabE12 by confocal microscopy. Images are maximum projections of 3 confocal slices to visualize the medial volume of the cell and acquired at 5-sec intervals. Selected images from a time series are shown using a 16-color look-up table with the corresponding pixel value range shown on the right. B, Subcellular localization of 3xmCherry-RabE14 and MyosinXIa-3xmEGFP from an independently isolated line. Scale bar, 5  $\mu\text{m}$

Plants use the exocytosis machinery to transport secretory vesicles and other cargoes to build the cell plate in a mechanism similar to tip growth (Fendrych et al., 2010; Wu and Bezanilla, 2014; Mayers et al., 2017b). Therefore, we predicted that myosin XI and RabE function together, not only at the tip for cell growth, but also at the cell plate for cytokinesis. Consistent with recent work (Abu-Abied et al., 2018; Sun et al., 2018), we observed that myosin XI localized to the cell's division zone immediately following nuclear envelope breakdown (Figure 3.1d). RabE is noticeably absent from the division zone until approximately 8 minutes following nuclear envelope breakdown, which is consistent with the emergence of the phragmoplast (Sun et al., 2018). Upon RabE arrival at the division zone, RabE and myosin XI display coordinated behavior while confined to the phragmoplast (Figure 3.1d). RabE initially localizes as discrete puncta and then expands outward toward the cell wall (Figure 3.1d). Interestingly, unlike myosin XI, intense foci of RabE are present on the opposing plasma membranes that the phragmoplast-localized RabE grows towards. These foci manifest via the coalescence of RabE-decorated endomembrane structures. Upon fusion of plasma membrane-localized RabE and phragmoplast-localized RabE, coincident with myosin XI reaching the plasma membrane, the bright foci dissipate and a near homogeneous cytoplasmic signal of RabE remains (Figure 3.1d). Together, these observations establish RabE and myosin XI as spatiotemporally coupled in polarized transport processes.

### 3.3.2 RabE is Required for Normal Growth in *P. patens*, and *A. thaliana* RabE1c Rescues the *rabE* mutant

Our data and previous studies strongly implicate RabE in supporting plant growth and development (Zheng et al., 2005; Speth et al., 2009; Ahn et al., 2013; Mayers et al., 2017b). However, to date no study has investigated RabE in the context of a comprehensive loss-of-function (*rabE*) background.

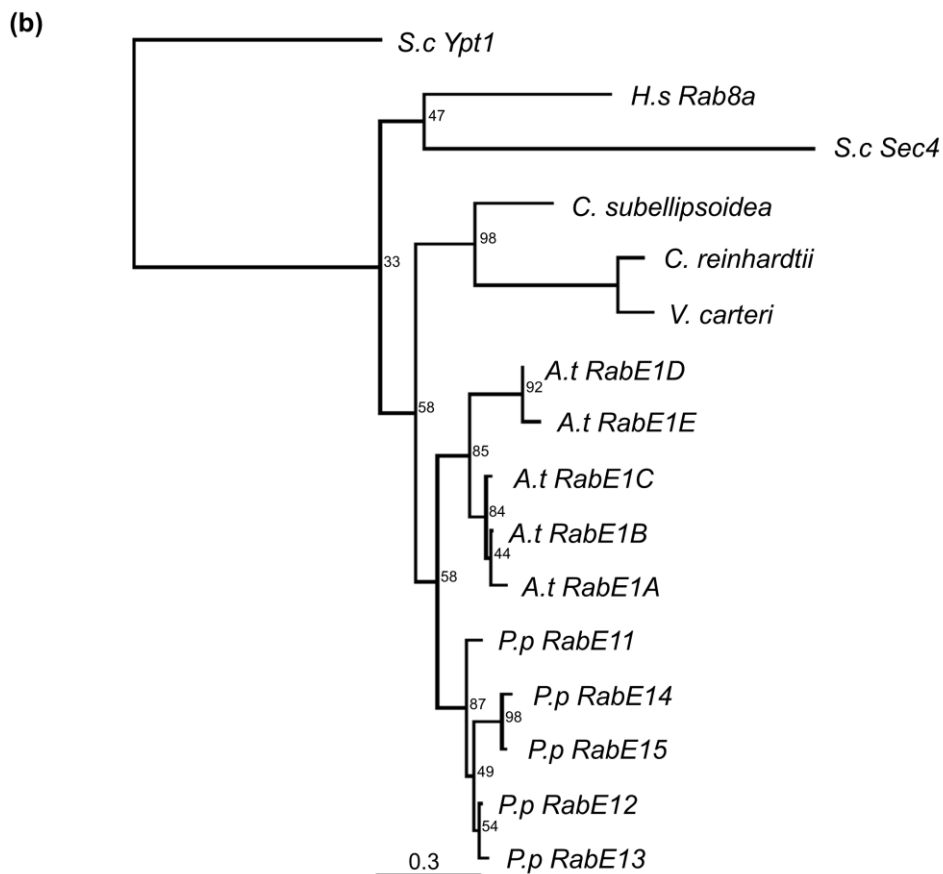
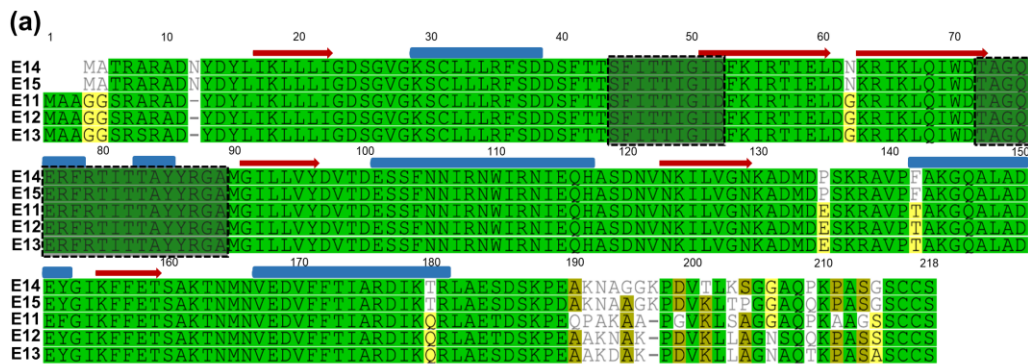


**Figure 3.3** Sequence alignment of *P. patens* RabE and phylogenetic tree of RabE and RabE-like proteins. A, Multiple sequence alignment of the five members of the *Physcomitrella patens* RabE subfamily. Pairwise percent identity ranges from 89% (RabE14-RabE11), to 97% (RabE14-RabE15, RabE12-RabE13). Pairwise residue percent similarity is visualized by color: green=100%, yellow=60-80%, white<60%. Predicted secondary structure of active RabE14—red arrow= $\beta$ -sheet, blue tube= $\alpha$ -helix. Switch I and II domains are outlined by the dotted line. B, Maximum likelihood phylogenetic tree of RabE subfamily members from select Viridiplantae species (*Coccomyxa subellipsoidea*, *Chlamydomonas reinhardtii*, *Volvox carteri*, *Arabidopsis thaliana*, *Physcomitrella patens*) and homologous Rab8a from human and Sec4 from *Saccharomyces cerevisiae*. *Saccharomyces cerevisiae* Ypt1 (Rab1) was used as the outgroup. Numbers indicate bootstrap support values for their respective branch.

To systematically deplete *P. patens* of the five-member RabE subfamily (Figure 3.3), we employed an integrative approach. We reasoned complete removal of RabE might result in non-viable plants, so we coupled CRISPR/Cas9 mediated knockouts of two isoforms,  $\Delta$ rabE14/15 (Figure 3.4), with subsequent RNAi to knockdown the remaining three isoforms.

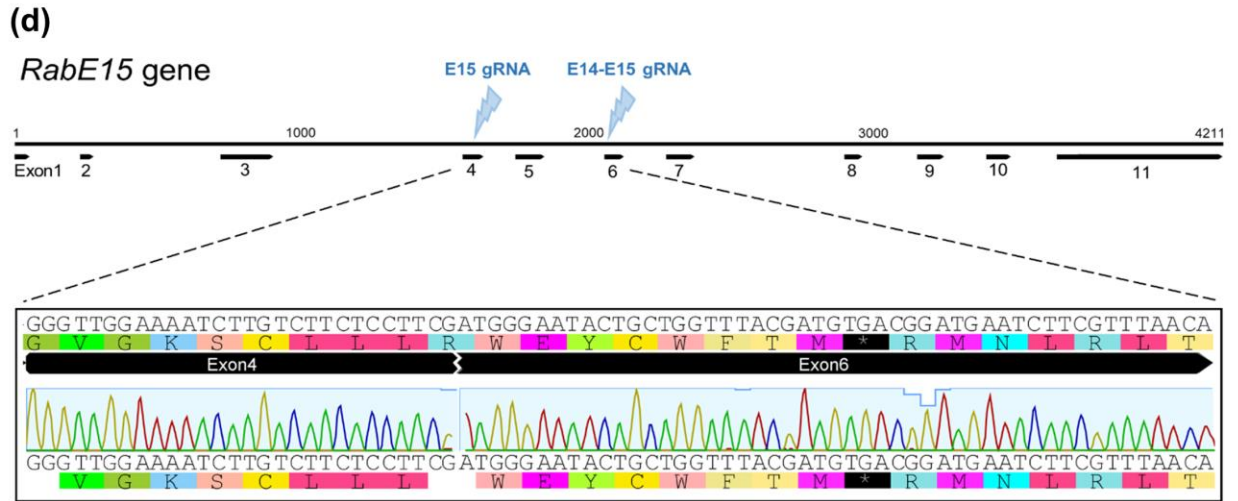
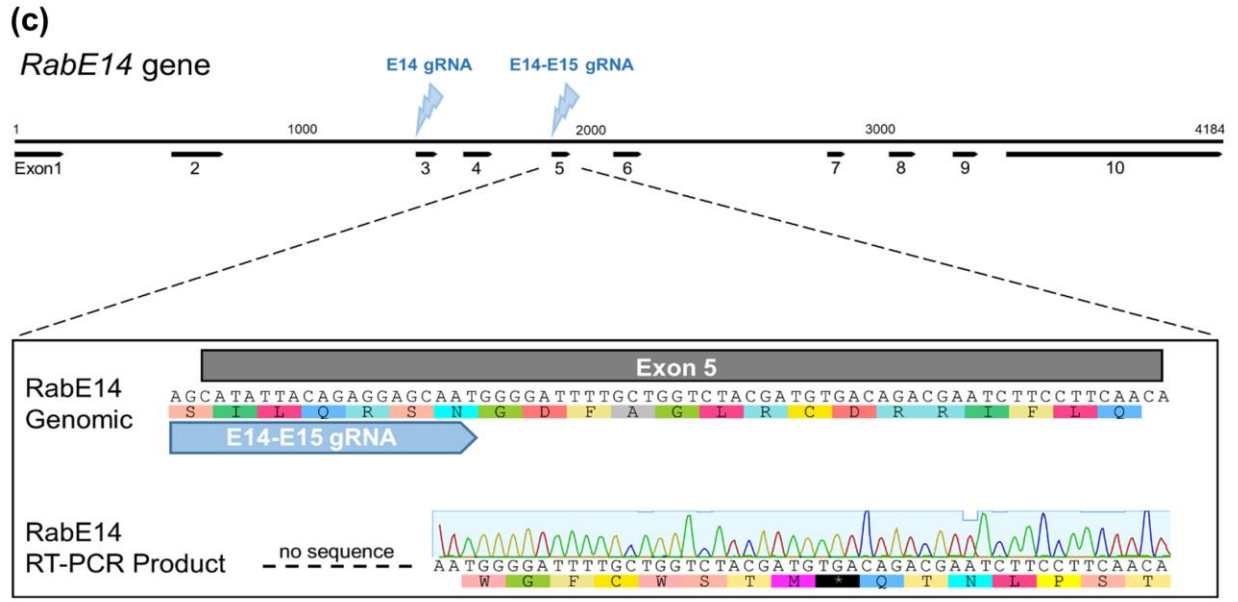
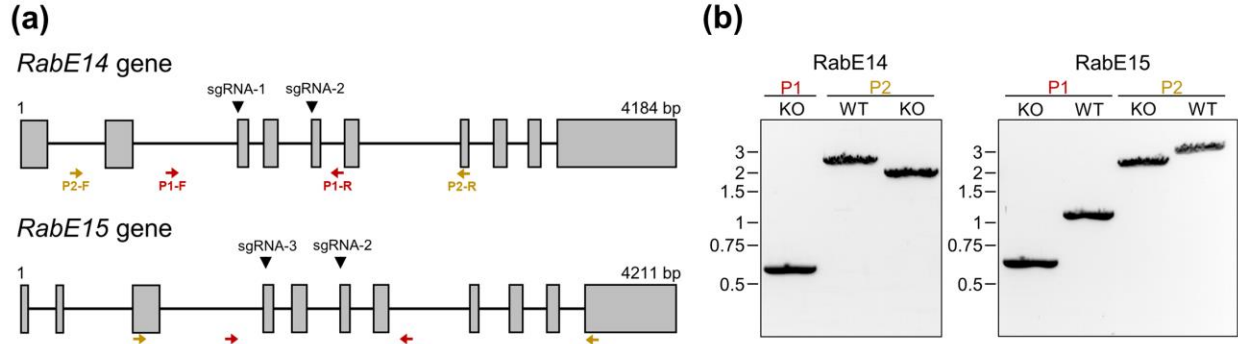


**Figure 3.4** CRISPR/Cas9 knockout of RabE14 and RabE15. A, Schematic of the RabE14 and RabE15 genomic loci that were targeted for CRISPR-mediated knockout. For both RabE14 and RabE15, two sites were targeted with sgRNAs to excise a large fragment from each locus. The gray boxes represent exons, with the arrows underneath showing the location of the primers used for genotyping. B, Genotyping of the RabE14 + RabE15 CRISPR knockout line using the primer combinations shown in (a). Both loci show the predicted ~1kb excision indicating successful CRISPR editing with both pairs of sgRNAs. C, Sequence verification of a premature stop codon located within wild-type exon 5. This RabE14 mutation results in a 31-residue protein product. D, Sequence verification of a premature stop codon located within wild-type exon 6. This RabE15 mutation results in a 40-residue protein product.

To deplete the final three RabE isoforms we generated an RNAi construct targeting a conserved ~400 bp region within the RabE11 CDS (RabE11i), which is 88% and 90% identical to RabE12 and RabE13, respectively. To investigate our *rabE* plants without the need for a specialized RNAi reporter line we used our recently developed RNAi system that exploits positive selection of an endogenous marker to enable robust, high-throughput phenotyping (Orr et al., 2020b). To characterize the growth phenotype of the mutant moss plants, we quantified two morphological parameters of the plant, area and solidity (Vidali et al., 2010b). Solidity is the ratio of the plant area to the convex hull area, which is used as a morphological metric of plant polarization. Upon silencing with the RabE11i construct in the  $\Delta$ rabE14/15 background, we observed morphologically stunted plants at 8-days post-transformation (Figure 3.5). Notably, when tested separately, both the  $\Delta$ rabE14/15 and RabE11i conditions resulted in slightly smaller plants, and neither displayed any significant difference in plant solidity. Only when the RabE11i construct was introduced into the  $\Delta$ rabE14/15 background did we observe an additive effect on plant size and reduced solidity, again highlighting the functional redundancy of the RabE subfamily (Figure 3.5). The *rabE* mutant's diminished size and polarity (Figure 3.4b) is

consistent with a role in polarized growth, as myosin XI displays a similar, albeit more pronounced, phenotype (Vidali et al., 2010b).

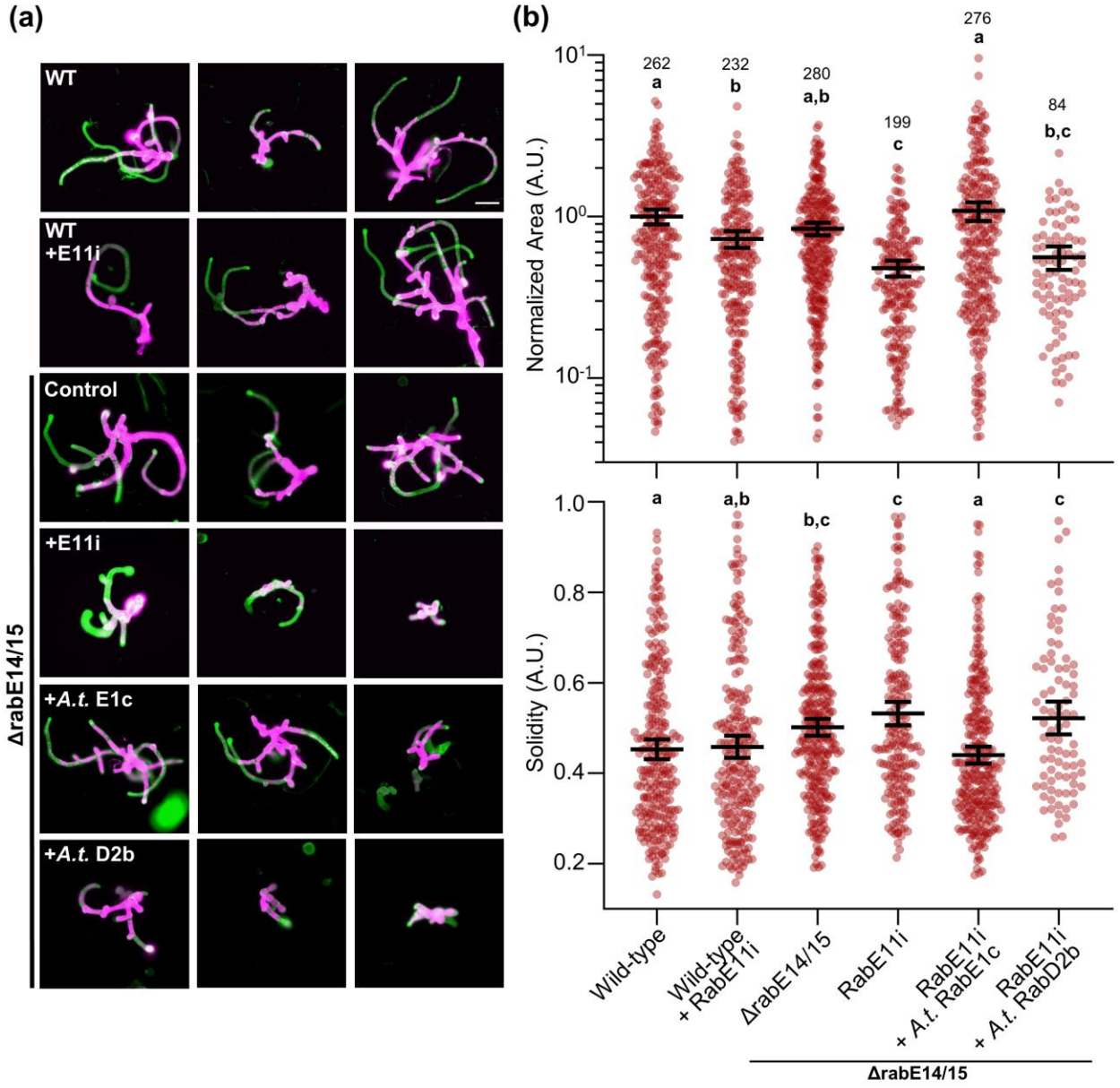


**Figure 3.5** The RabE GTPases are required for normal plant growth and the growth defect is rescued with RabE1c from *Arabidopsis thaliana*. A, Representative 8-day old plants regenerated from protoplasts using the APT-based RNAi assay. Plants were stained and imaged with calcofluor, colored in green, and also imaged for chlorophyll autofluorescence shown in magenta. Bar = 100  $\mu$ m. B, Quantification of plants from the APT-based RNAi growth assay. Each data point represents an individual plant. Three independent experiments were performed and pooled. Plant area was normalized to the wild-type condition. Lines and error bars represent the mean and 95% confidence interval for each group, respectively. Shared letters above the bars show those experimental groups that cannot be statistically distinguished. Statistical significance was determined by a one-way ANOVA-Tukey ( $P < 0.01$ ). Numbers above the letters indicate number of plants analyzed per condition.

We next tested whether our *rabE* mutant could be rescued by a distantly related RabE. This idea was motivated by the fundamental cellular requirement of RabE for polarized trafficking, similar RabE localization between our observations and other plant species, and protein-level conservation (~90% identity between *A. thaliana* and *P. patens*). Strikingly, RabE1c from *Arabidopsis thaliana* fully rescued our *rabE* phenotype (Figure 3.5). Importantly, the observed phenotype is specific to the plant RabE subfamily. Exogenously supplied *A. thaliana* RabD2b failed to rescue the morphological defects (Figure 3.5). These data establish RabE as indispensable for cellular polarization and growth. Furthermore, rescue of the *rabE* phenotype with RabE1c from *A. thaliana* supports an evolutionarily conserved function, likely in concert with myosin XI.

Although our plant-level morphological analysis is entirely consistent with RabE being required for polarized growth, we sought to directly observe cell growth. We achieved this through long-term (ranging from 9-24 hours) live cell imaging of wild-type and *rabE* plants. Plants were manipulated identically to those in Figure 3.5, except at day 5 post-transformation the plants of interest were transferred to plates with a thin layer of agar surrounded by a larger agar reservoir, thereby allowing acquisition close to the

agar/plate interface. Additionally, the agar contained calcofluor to facilitate automated image acquisition and downstream analysis. This approach revealed a substantial cellular growth phenotype, with the *rabE* line growing at an average of  $1.1 \pm 0.75 \mu\text{m h}^{-1}$  compared to the average wild-type growth rate of  $4.9 \pm 1.9 \mu\text{m h}^{-1}$  (Figure 3.6).

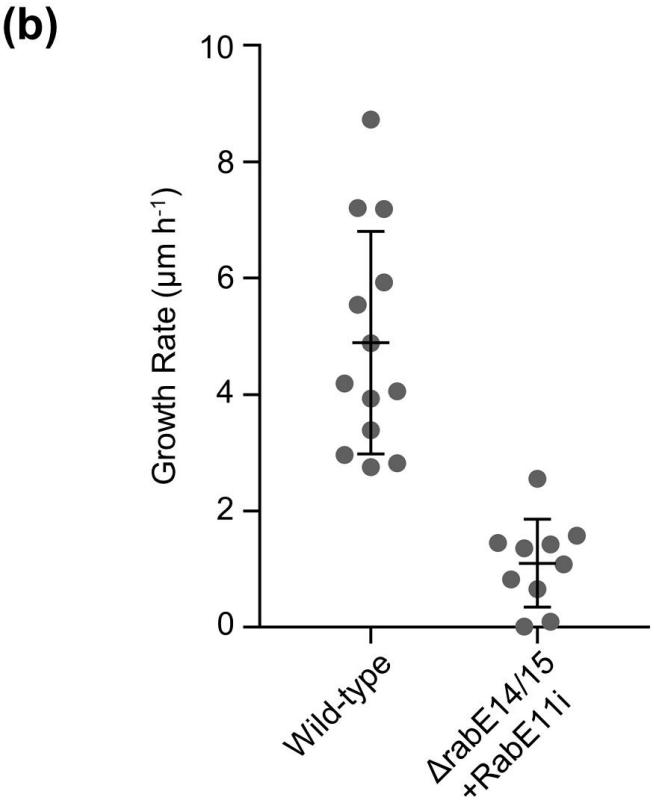
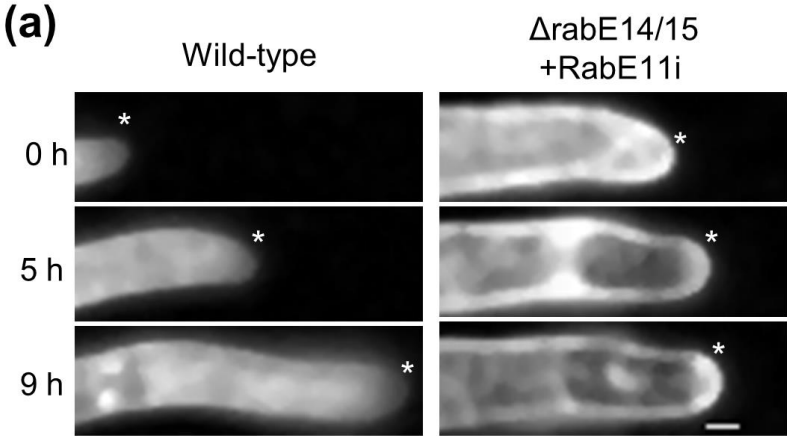


**Figure 3.6** RabE is required for normal polarized cell growth. A, Time series of representative apical cells used for growth rate determination. The asterisk denotes the cell tip, scale bar = 10  $\mu\text{m}$ . B, Quantification of growth rate extracted from kymographs of apical cell growth time series, such as in (A). Data points represent in-focus apical cells. Apical cells were pooled across two independent experiments. Bars represent the mean and standard deviation. Significance was tested via a two-tailed T-test,  $p < 0.001$

Together, these results support our hypothesis that RabE is essential for polarized cell growth. However, to rule out the unlikely possibility (given the *A. thaliana* RabE rescue) of an off-target RNAi effect being the cause of the loss of polarized growth phenotype, we performed RT-qPCR on the remaining full-length RabE transcripts. This analysis confirmed that RabE transcripts were downregulated, specifically RabE11, which was reduced by approximately 80% (Figure 3.7). Additionally, RabE12 and RabE13 had their transcript abundance decreased by 70% and 30%, respectively. This level of transcript reduction is consistent with both the observed reduction in growth rate and our expectation that RabE is essential for viability. Based on these results, we conclude that RabE is necessary for plant polarized growth and likely functions analogously in tip growing cells of vascular plants given the functionality of *Arabidopsis* RabE1c in *P. patens*.

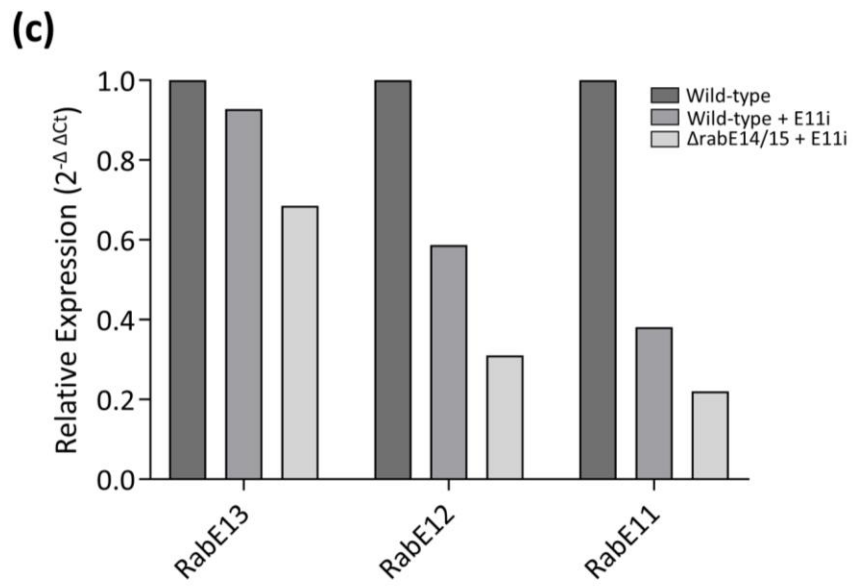
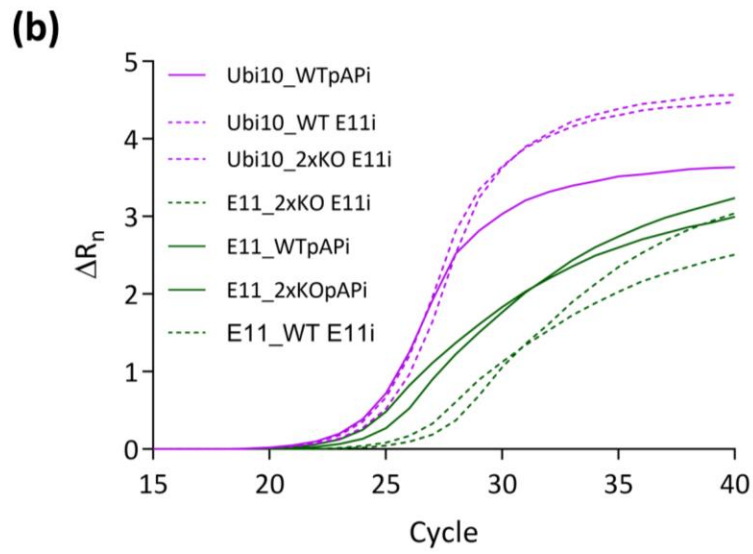
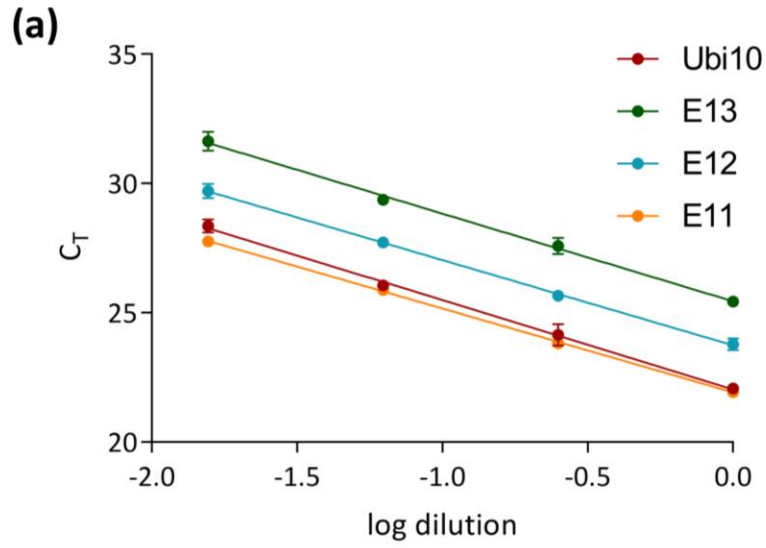


**Figure 3.7** Relative expression of the transcripts from the unedited RabE genes (E11, E12, E13). A, Determination of PCR efficiency for each primer pair to verify the assumption of equal amplification efficiency implicit in the standard method of relative quantitation of RT-qPCR results. B, Amplification curves of the reference gene and the most downregulated gene, RabE11, across different experimental conditions. C, Transcript abundance was determined via RT-qPCR and quantified using the  $2^{-\Delta \Delta Ct}$  method. Ubiquitin 10 was used for normalization. Data is the mean of two technical replicates taken from one biological replicate, therefore no error bars are displayed.

### **3.3.3 Myosin XI is a Conserved Effector of RabE, and *A. thaliana* Myosin Isoforms XI-K and XI-E Rescue Loss of Endogenous Myosin XI in *P. patens*.**

Our data demonstrated a strong relationship between RabE and myosin XI in polarized growth, therefore we investigated the existence of a direct interaction. We hypothesized that myosin XI directly interacts with RabE, and that this interaction is required for polarized growth. In parallel with our directed investigation, we performed a yeast two-hybrid screen in conjunction with Hybrigenics (France) as an unbiased approach to identify putative *P. patens* myosin XI interactors. The myosin XI bait construct contained the canonical C-terminal myosin XI cargo-binding domain plus a small N-terminal extension into the coiled-coil domain, hereafter called MyoXI-CCT. Consistent with our previous data and hypothesis, our Y2H screen identified a full-length RabE GTPase protein, RabE14 (Pp3c6\_11710). As yeast two-hybrid screens can be prone to false-positives, we independently verified this putative interaction with a directed Y2H (Figure 3.8a). Almost all sequence diversity between the RabE isoforms is located within the hypervariable C-terminal domain, while the canonical effector-determining regions localized within and near the switch regions maintain high sequence identity (Figure 3.3a). Therefore, we predicted that myosin XI binding is a shared function within the RabE subfamily. The most similar isoform, RabE15, and divergent isoform, RabE11, both show

a positive interaction with myosin XI (Figure 3.8a). We interpret this as the RabE subfamily being functionally redundant with respect to myosin XI binding, and is consistent with other identified RabE effectors (Camacho et al., 2009; Mayers et al., 2017b).

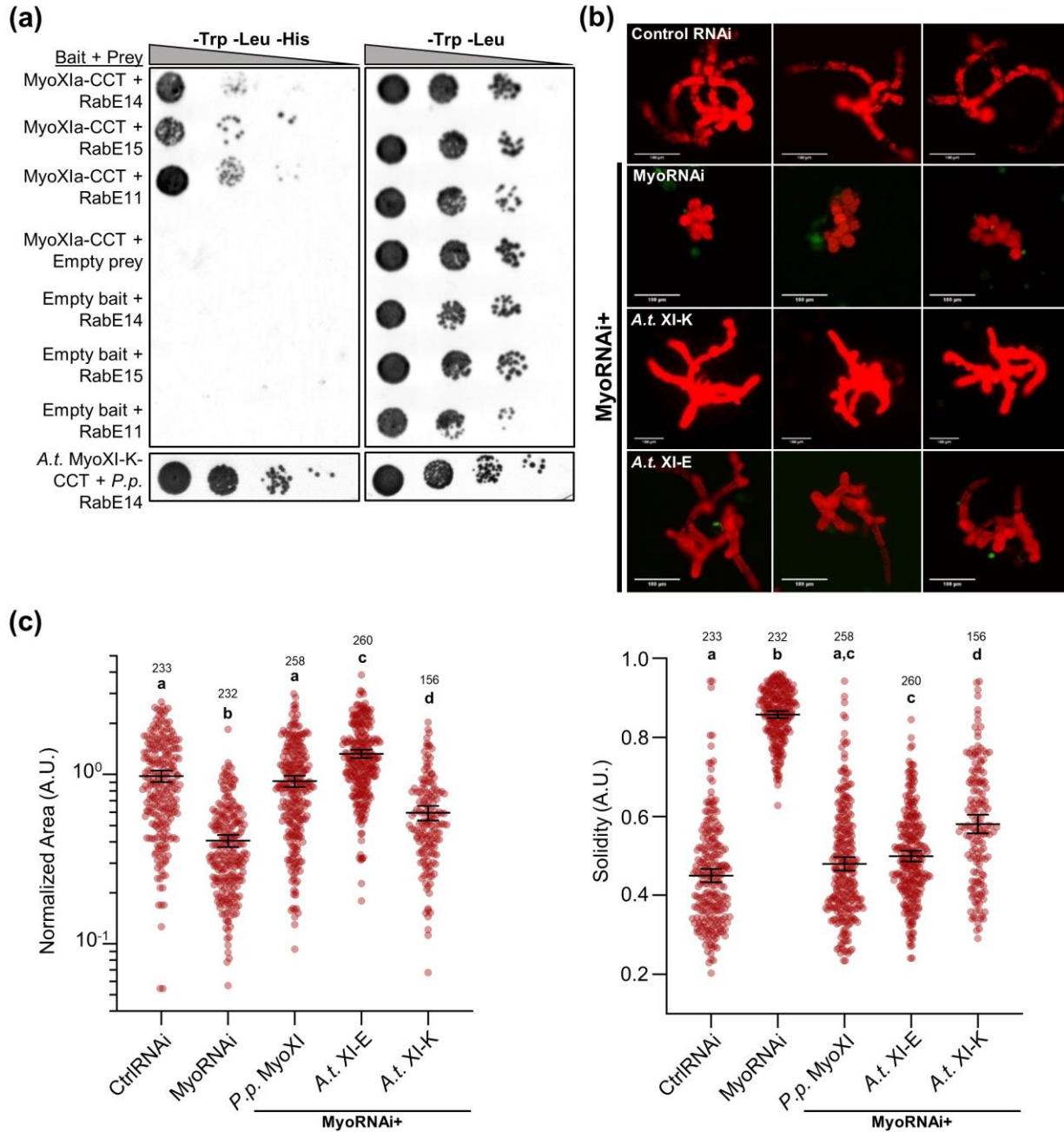


**Figure 3.8** *P. patens* RabE subfamily interacts with both moss myosin XI and *Arabidopsis* myosin XI-K isoform, and A.t. XI-K/E rescue loss of endogenous P.p. myosin XI. A, Directed Y2H using the P.p. myoX1a-CCT and A.t. XI-K-CCT bait constructs and full-length RabE14, RabE11, and RabE15 results in growth on synthetic defined (SD) medium lacking histidine. Empty bait and prey plasmids were tested with their respective partners to test for autoactivation of *HIS3*. B, Representative 1-week old RNAi plants—all plants except ‘CtrlRNAi’ are silencing expression of both endogenous myosin XIs. All plants except ‘MyoRNAi’ were co-transformed with the myosin XI silencing construct and another construct expressing either WT myosin XI or mutant myosin XI. Bar = 100  $\mu$ m. C, Quantification of plants from the myosin XI-chimera growth assay. Each data point represents an individual plant. Three independent experiments were performed and pooled. Plant area was normalized to the wild-type condition. Lines and error bars represent the mean and 95% confidence interval for each group, respectively. Shared letters above the bars show those experimental groups that cannot be statistically distinguished. Statistical significance was determined by a one-way ANOVA-Tukey ( $P < 0.01$ ). Numbers above the letters indicate number of plants analyzed per condition.

Our results demonstrating cross-species functionality of RabE and the pervasiveness of homologous myosin:Rab interactions across eukaryotes motivated us to explore the possibility of a conserved interaction in plants. To that end, we tested and confirmed that the cargo-binding domain of *A. thaliana* myosin XI-K interacts with *P. patens* RabE (Figure 3.8a). Taken together with the literature showing similar subcellular co-localization of XI-K with vesicles at the growing root hair tip and XI-K’s general requirement for polarized growth, we hypothesized the CBD of XI-K from *A. thaliana* would rescue *P. patens* plants depleted of endogenous myosin XI. To test this, we generated a full-length chimeric myosin XI protein containing the CCT of A.t. XI-K, while maintaining the head and neck domains of *P. patens* myosin X1a. In this way, we are directly investigating the same domain of XI-K for our *in planta* assay as tested in the Y2H. We found that A.t. XI-K and another Arabidopsis isoform, XI-E, are sufficient to promote polarized growth in *P. patens* plants lacking native myosin XI (Figure 3.8b,c).

These results support the hypothesis of a conserved mechanism of polarized growth, likely mediated by an interaction between myosin XI and RabE.

### **3.3.4 Myosin XI:RabE Interface Prediction**

To gain molecular insights of the MyoXI:RabE interaction, we hypothesized that the binding interface is structurally homologous that of the well characterized class V myosin binding to Rab8/Sec4 (Goldenring et al., 2012; Welz and Kerkhoff, 2017). A multiple sequence alignment of moss RabE14, Sec4 from *Saccharomyces cerevisiae*, and Rab8a from *Homo sapiens* strikingly illustrates the extent of conservation within the canonical Rab effector-binding regions (Figure 3.9a). Rabs undergo a dynamic GTP-dependent rearrangement of two structural regions, named “switch-I” and “switch-II,” which defines their “active” GTP-bound state and effector recognition (Stroupe and Brunger, 2000; Khan and Menetrey, 2013). Given the near perfect identity within the switch regions, we speculated that structural models of myosin XI-tail and RabE14, based on the well-characterized Sec4 and Myo2 interaction, could assist in mapping the functional interface.

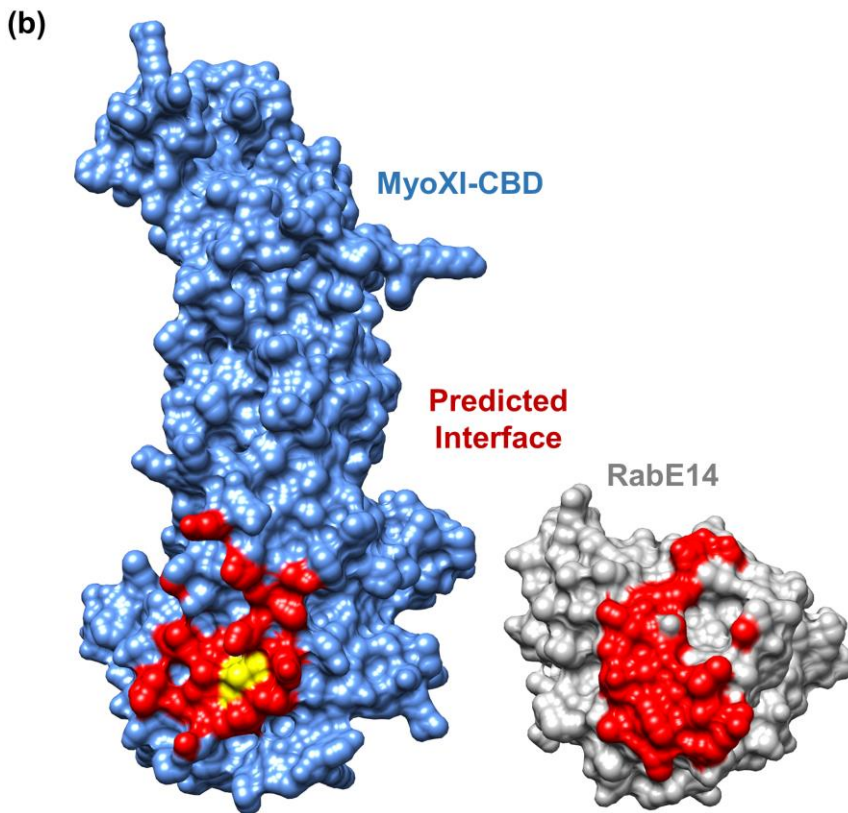
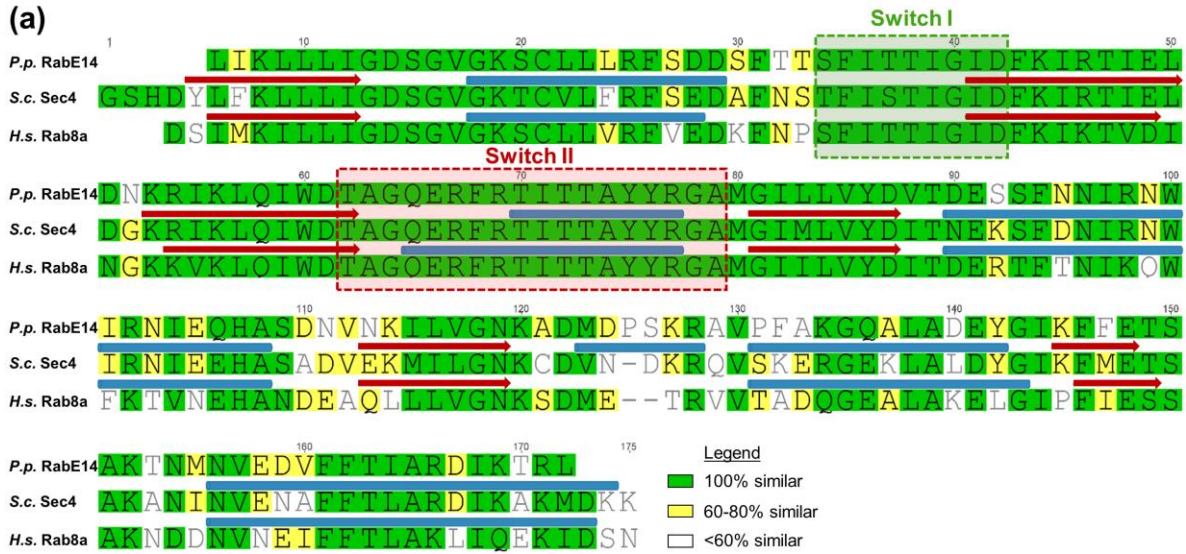


**Figure 3.9** RabE sequence conservation and prediction of Myosin XI-CBD and GTP-bound RabE14 binding interface. A, Multiple sequence alignment of *Physcomitrella patens* (P.p.) RabE14, *Saccharomyces cerevisiae* (S.c.) Sec4, and *Homo sapiens* (H.s.) Rab8a. Secondary structure (red arrow= $\beta$ -sheet, blue tube= $\alpha$ -helix) of Sec4 and Rab8a was manually annotated based on their crystal structures, PDB IDs 1G17 and 4LHW, respectively. B, Predicted MyoXI:RabE interface using homology modeling and structural superposition as described in methods. Modeled contact residues are colored red, with residue V1422 colored yellow.

To identify the putative interface between RabE14 and myosin XI, we employed a homology-based *in silico* approach. We first generated homology models of *P. patens* myosin XI CBD and RabE14 using yeast Myo2-CBD and Sec4-GTP as templates (Figure 3.10).

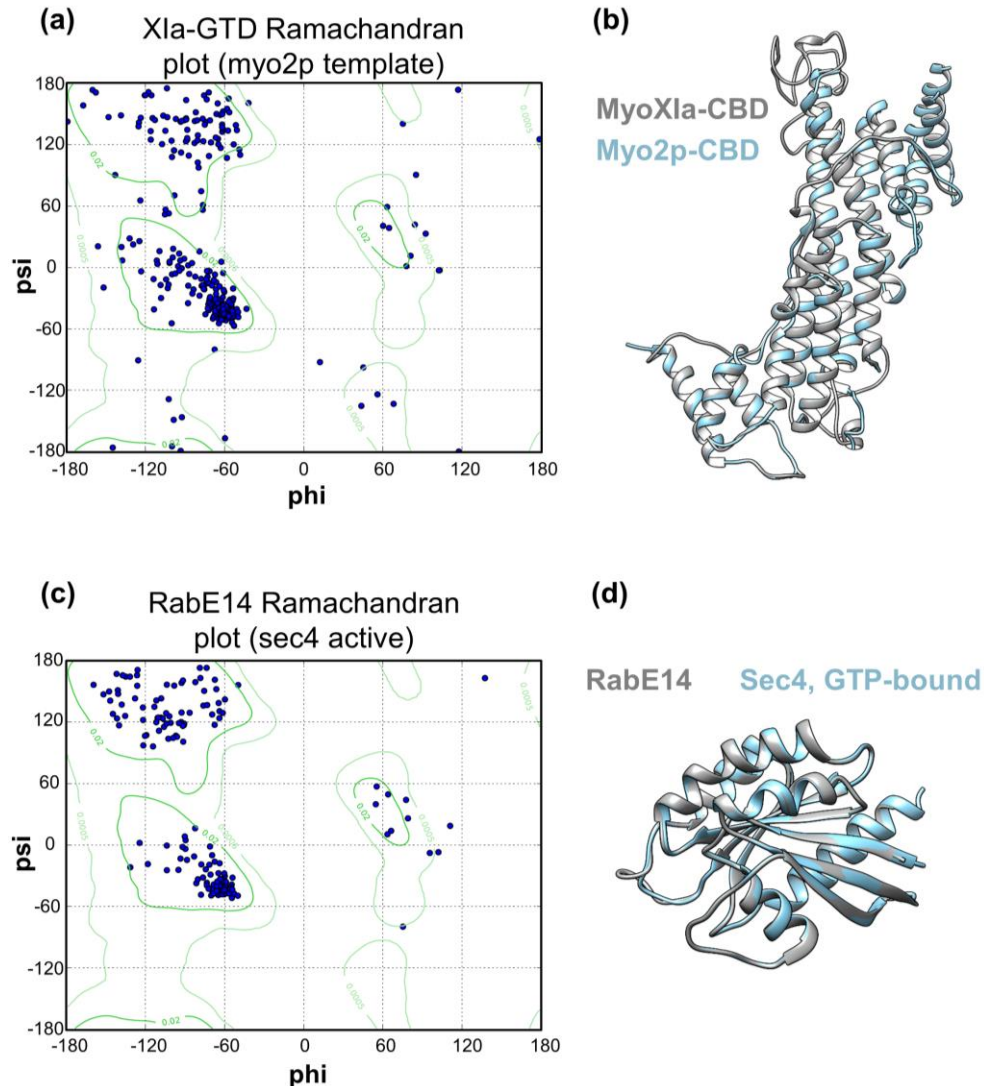


**Figure 3.10** Ramachandran plots and average RMSDs for myoXla-CBD and RabE14 homology models. A-D, Both myoXla-CBD and RabE14 homology models used for interface prediction exceed the conventional cutoff of >95% of all non-glycine residues must occupy the energetically allowed regions within the Ramachandran map to conclude good stereochemical quality. A, Eight non-glycine residues of myoXla-CBD are located outside of these regions (corresponding to ~98% within). B, The average RMSD of myoXla-CBD is 0.291 Å. C, Four non-glycine residues of GTP-bound RabE14 are located outside (corresponding to ~98% within). D, The average RMSD of GTP-bound RabE14 is 0.134 Å

We leveraged these homology models to computationally predict the binding interface between myosin XI and RabE14 using both structural super-positioning (Figure 3.9b) and the template-based algorithm, PRISM (Tuncbag et al., 2011; Baspinar et al., 2014) (Figure 3.12a). At the amino acid level, almost all predicted associations occur within the switch-I, interswitch, switch-II region (Figure 3.12a). Both interface prediction methods and myosin templates identified the myosin XI residue V1422 as a putative interface residue (Figure 3.11a). V1422 of myosin XI structurally aligns with Q1447 of Myo2p (Figure 3.11b); Q1447 was previously determined to reside in the yeast secretory vesicle binding site (Pashkova et al., 2006) and later shown to directly associate with the Rabs Ypt31/32 (Lipatova et al., 2008) and Sec4 (Jin et al., 2011). Altogether, these results support a remarkable degree of structural conservation, and suggest that RabE functions as a myosin XI receptor on secretory vesicles in plants.



**Figure 3.11** Prediction of Myosin XI-CBD and GTP-bound RabE14 binding interface is robust. A, Predicted interface residues for MyoXI-CBD using different templates and methods results in similar interface profiles. All interface residues shared between each condition are bordered in red. Importantly, V1422 (star) was shared between all interface predictions and aligns with known interaction residue Q1447 from *S.c.* Myo2p (shown below). All experimentally identified yeast Myo2p interaction residues, shown in black letters, were captured with structural superposition as described in methods. B, Structure-based sequence alignment of myoXIa-CBD homology model and myo2p-CBD crystal structure. Structure-based sequence alignment was performed with UCSF Chimera using our homology model of *P. patens* myosin XI cargo-binding domain and crystal structure of *S. cerevisiae* myosin V cargo-binding domain (myo2p-CBD), PDB=2f6h.

### **3.3.5 Structure-based Mutants Disrupt the Myosin XI:RabE Interaction, Resulting in a Loss of Polarized Growth**

Prediction of the putative MyoXI:RabE interaction identified several candidate residues on myosin XI-CBD that could mediate an interaction with RabE, with residue V1422 emerging as the primary candidate. To test if V1422 is required for myosin XI-CBD to interact with RabE14, we performed a directed Y2H assay in which V1422 was mutated to arginine. We generated an additional myosin XI-CBD mutant, V1418R, to probe the region near V1422 that is bounded by our predicted interface. Consistent with our interface prediction, both mutants eliminated the interaction with RabE14 (Figure 3.12b). Furthermore, western blot analysis of the positive Y2H interactions confirmed the presence of the myosin XI mutants at levels equivalent to wild-type (Figure 3.13). However, we suspected that the V1418R mutant resulted in a misfolded protein, as evidenced by a slight cytotoxic effect (Figure 3.12b), its buried side chain relative to V1422 (7.7 Å<sup>2</sup> and 36.2 Å<sup>2</sup> solvent accessible surface area, respectively), and low solubility when purified recombinantly (Figure 3.14). Taken together, these data support our *in silico* predicted interface, such that the V1422R mutation within myosin XI's cargo-binding domain specifically abolishes RabE14 binding.

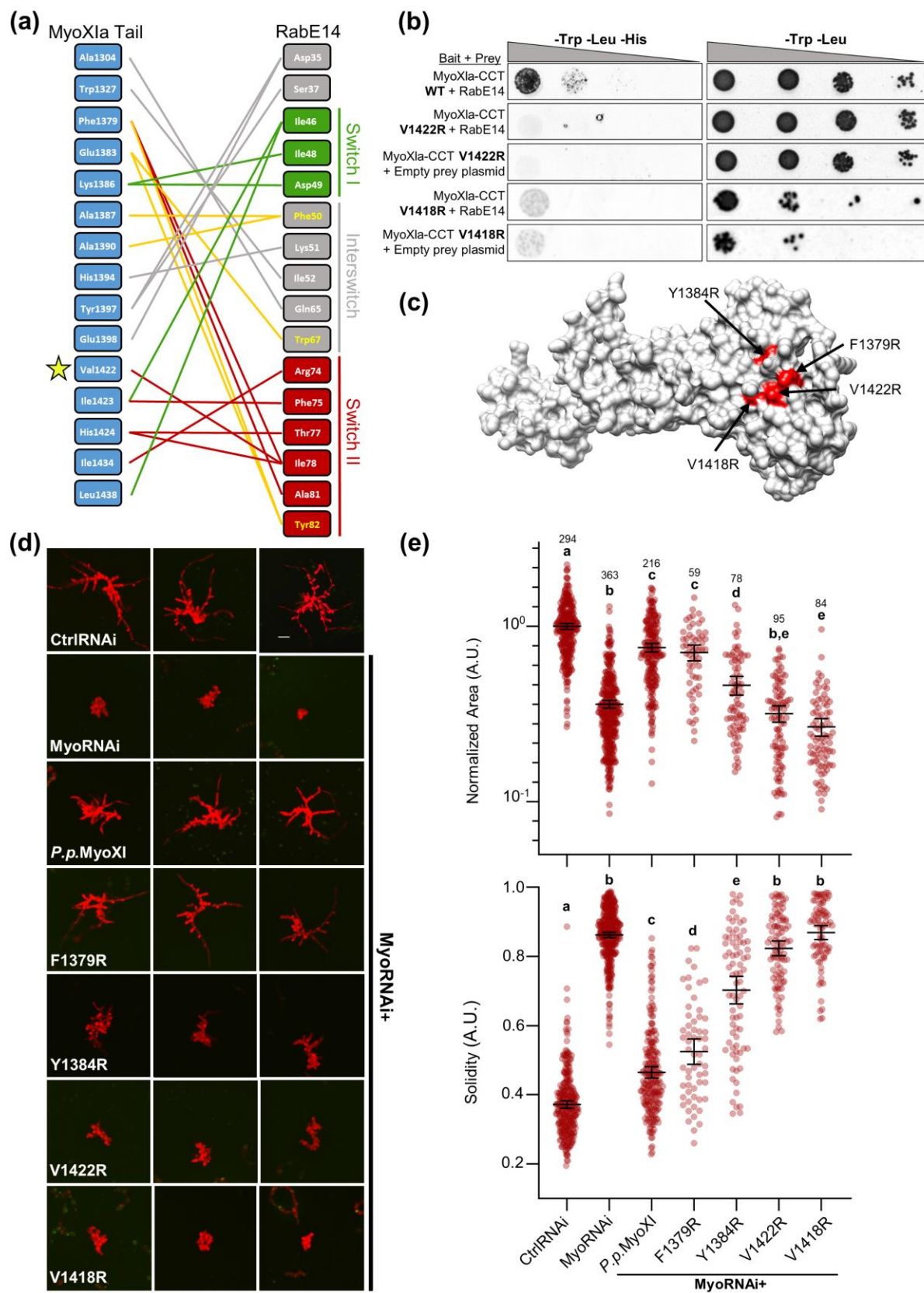


**Figure 3.12** Structure-guided mutagenesis of predicted Myosin XI-CBD:RabE14 binding interface reveals polarized growth mutants. A, Contact map of modeled myosin XI:RabE14 (-17.8 kcal mol<sup>-1</sup>) determined by template-based docking algorithm PRISM (Tuncbag et al., 2011). Hydrophobic triad residues and their putative contacts colored in yellow. Colors of lines representing contacts reflect the domain within RabE14 that the contact belongs. Green=Switch I, Red= Switch II, Grey=Interswitch, Yellow=Hydrophobic triad. B, Directed Y2H with the P.p. myoXI-CCT WT bait fragment from (Fig. 3.8) and bait fragments containing mutations in the myosin XI cargo-binding domain that are required for polarized growth and predicted to interact with RabE14. All yeast strains were grown on the same SD plates, but rearranged for clarity. C, Homology model of P.p. myosin XI-tail is shown, with the candidate interface residues predicted to mediate RabE interactions in red. D, Representative 1-week old RNAi plants—all plants except ‘CtrlRNAi’ are silencing expression of both endogenous myosin XIs. All plants except ‘MyoRNAi’ were co-transformed with the myosin XI silencing construct and another construct expressing either WT myosin XI or mutant myosin XI. Bar = 100 μm. E, Quantification of the morphological parameters of solidity and area extracted from images in (d). Error bars indicate standard error of the mean. Shared letters above the bars show those experimental groups that cannot be statistically distinguished. Statistical significance was determined by a one-way ANOVA-Tukey (P<0.01). Numbers above the letters indicate number of plants analyzed per condition.



**Figure 3.13** Detection of myosin XI protein abundance in Y2H experiments. Strains were grown in SD medium lacking trp and leu to an OD600 of 1 and assayed for expression of myoXIa-CCT via western blot. Total extracted yeast protein was blotted using a myoXI-CCT antibody and ADH1 as a loading control. The condition MyoXIa-CCT V1422R+empty bait plasmid belongs to the western blot shown on the left but was rearranged for clarity.

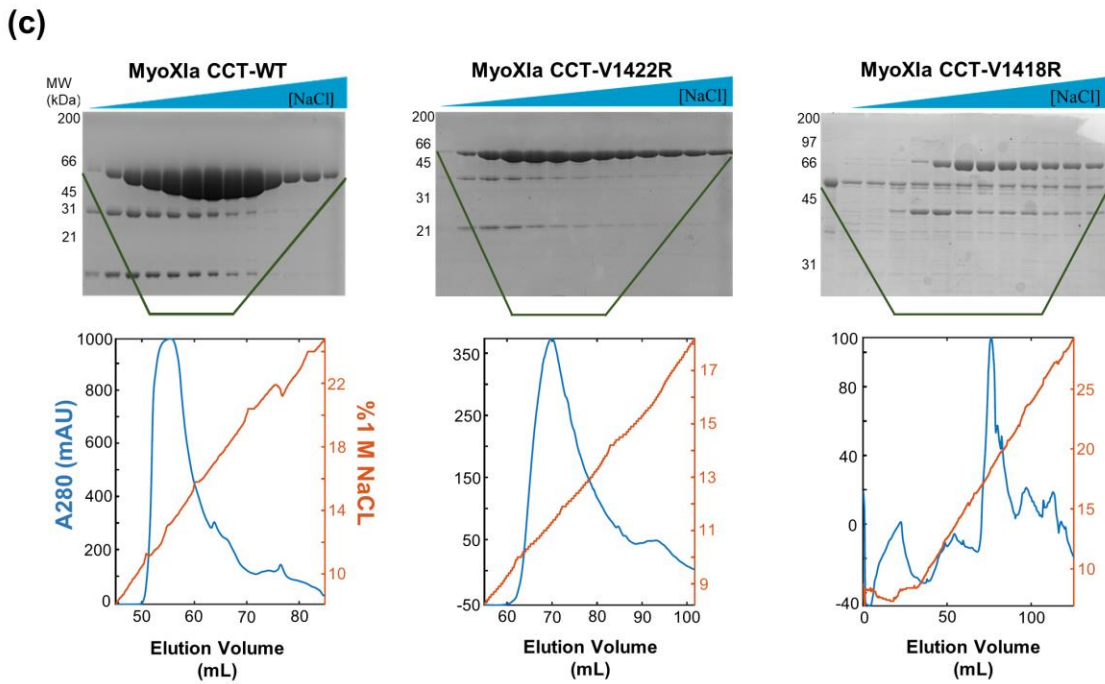
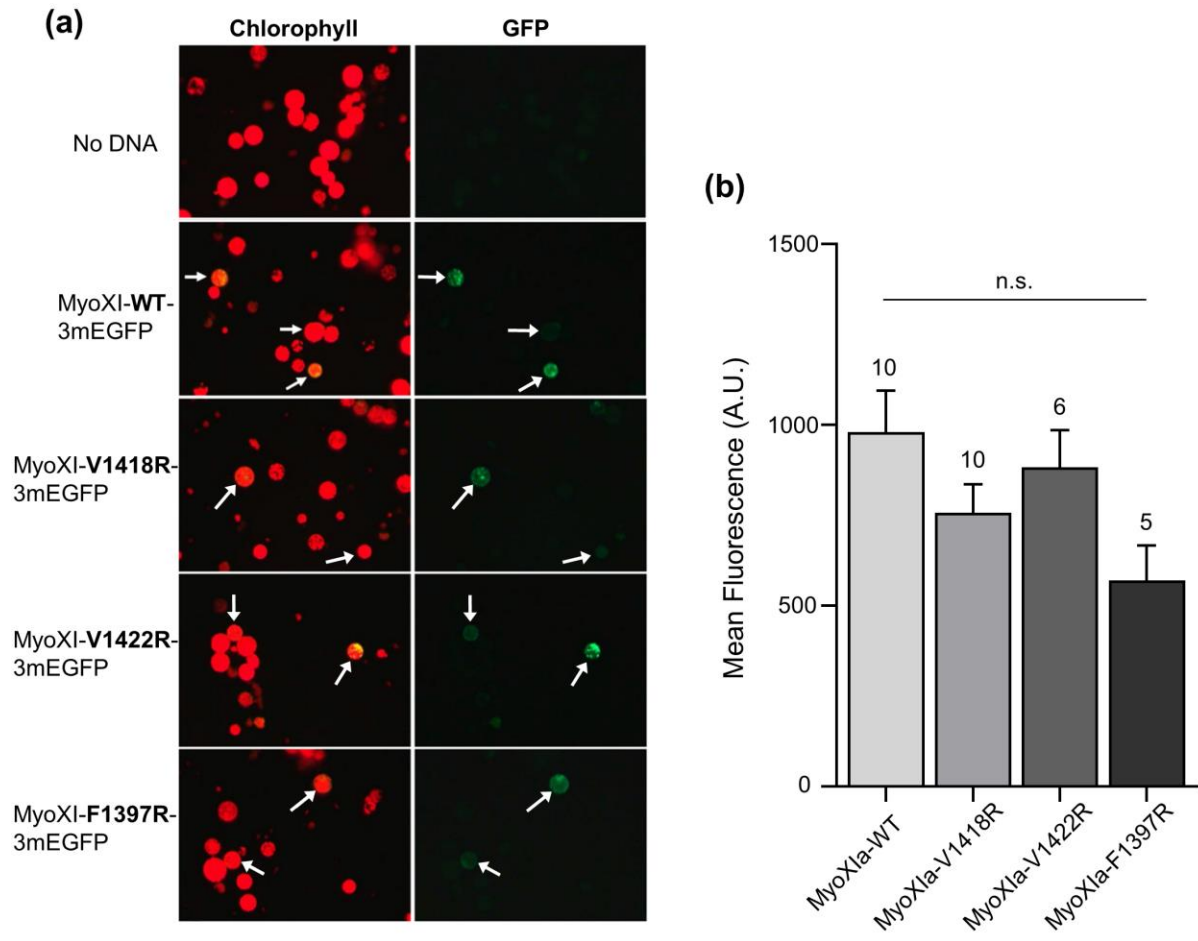


**Figure 3.14** Myosin XI cargo-binding domain mutants show varying levels of solubility. A, Representative fluorescent images of wild-type moss protoplasts one day post-transformation with the indicated construct. B, Quantification of expression for each fluorescent myosin XI fusion construct for images obtained in (a). Within a given condition, the mean fluorescence across all GFP positive protoplasts for a single independent transformation was treated as one sample. We plotted the mean of these independent sample means and failed to distinguish a statistically relevant difference, as tested by a one-way ANOVA ( $P < 0.05$ ). Error bars indicate the standard error of the mean and numbers above the SEM indicate the number of independent experiments. C, SDS-PAGE gels of the elution fractions for WT and mutant myosin XI proteins following anion exchange chromatography. Each lane of the SDS-PAGE corresponds to fractions eluted from the column, with the absorbance at 280nm and percentage of 1 M NaCl plotted below.

Based on our previous results demonstrating cross-species complementarity and interaction between myosin XI and RabE, we predict the MyoXI:RabE interaction to be a fundamental component of the polarized transport process. Therefore, specific disruption of this interaction should manifest as loss of polarized growth. To perturb the predicted MyoXI:RabE interaction, we generated a panel of single-residue myosin XI-CBD mutants within the full-length CDS, which are highlighted in the model (Figure 3.12c). As expected, silencing of endogenous myosin XI results in small and round plants, as determined by significantly reduced area and solidity, respectively (Figure 3.12d,e). All the mutant plants show a statistically significant increase in solidity compared to control RNAi, with the Y1384, V1422R, and V1418R mutants also showing a statistically significant decrease in normalized plant area (Figure 3.12e). The V1422R and V1418R mutants are morphologically equivalent to silencing myosin XI, Y1384 shows an intermediate phenotype, and F1379 displays a near wild-type morphology (Figure 3.12d,e). The dramatic loss of a polarized growth phenotype observed in myosin XI-CBD mutants demonstrates that these individual residues are required for proper functioning of myosin XI in polarized growth.

To exclude the possibility that our observed mutant phenotypes were a consequence of absent or reduced myosin XI expression or stability, we created GFP and His-tagged constructs for the myosin XI mutants. Our GFP reporters confirmed myosin XI mutant expression in protoplasts at wild-type levels (Figure 3.14a,b), and purification of the V1422R mutant suggests normal solubility and stability (Figure 3.14c). Together, these results indicate that V1422 is required to mediate the polarized growth process, and the V1422R mutation specifically abrogates myosin XI's biological function through defective binding to RabE.

### **3.4 Discussion**

Our studies identified a critical interaction between the molecular motor myosin XI and the RabE GTPase subfamily and determined the cross-species ability for RabE to support plant growth. Despite multiple independent lines of research demonstrating the individual requirements for myosin XI and RabE in polarized trafficking, and the sequence homology to myosin V and Sec4, (Zheng et al., 2005; Peremyslov et al., 2008; Speth et al., 2009; Vidali et al., 2010b; Peremyslov et al., 2012; Park and Nebenführ, 2013) direct evidence supporting a myosin:Rab-driven transport model, as in budding yeast, was lacking (Peremyslov et al., 2013; Ryan and Nebenfuhr, 2018). We attribute the dearth of evidence to the expansion of the myosin XI family in vascular plants, background cytoplasmic streaming that confounds observations of vesicle transport, and existence of a promiscuous, plant-specific interaction between divergent myosin XI isoforms and MyoB proteins that decorate a unique endomembrane compartment (Kurth et al., 2017). By exploiting the reduced gene family of myosin XI and absence of cytoplasmic streaming in the moss *Physcomitrella patens*, in combination with Y2H, live-cell imaging, cross-

species complementation, and computationally directed mutant analysis, we identified functional homology between myosin XI/myosin V and RabE/Sec4.

Our Y2H screen used the myosin XI cargo-binding domain from the moss *P. patens* as bait, and isolated one member of the RabE subfamily, RabE14. Subsequent Y2H with other RabE members led us to conclude that binding of myosin XI is a general property of the RabE subfamily. Furthermore, generation of stable moss lines containing different RabE paralogs fused to either GFP or mCherry displayed similar dynamic subcellular localization as MyoXI. Our conclusion of the functional redundancy of the RabE subfamily is consistent not only with initial predictions (Pereira-Leal and Seabra, 2001; Rutherford and Moore, 2002), but subsequent experimental evidence demonstrating conserved RabE effector binding (Camacho et al., 2009; Mayers et al., 2017b).

We reasoned that if an *in vivo* association between myosin XI and RabE exists, we would observe strong co-localization of both proteins at sites of polarized exocytosis. Our live-cell observations of myosin XI and RabE established striking cross-correlation at the site of polarized growth. The distinct co-localization of RabE and myosin XI to the growing apical zone is reminiscent of commonly observed localization patterns of F-actin, secretory vesicles, myosin XI/V, and other secretory components across plants and fungi (Bi and Park, 2012; Furt et al., 2013; Hepler and Winship, 2015; Bibeau et al., 2018b; Riquelme et al., 2018). Additionally, we observed co-localization and co-migration of RabE and myosin XI during expansion of the nascent cell plate. Importantly, this result is not only in agreement with previous reports separately investigating myosin XI and RabE (Zheng et al., 2005; Chow et al., 2008; Yokota et al., 2009; Abu-Abied et al., 2018; Sun

et al., 2018), but is internally consistent with our apical co-localization data and the notion that plant cell division internally recapitulates much of the canonical polarized exocytosis machinery (Fendrych et al., 2010; Mayers et al., 2017b). This observation is significant because one model of myosin XI-based transport depends upon myosin's interaction with an adaptor protein, MyoB (Ryan and Nebenfuhr, 2018). Interestingly, MyoB is not found at the growing cell plate where myosin XI and vesicles localize (Abu-Abied et al., 2018; Sun et al., 2018), suggesting the presence of an unidentified myosin XI interactor. Importantly, myosin XI is required for normal cell division, as a triple myosin XI mutant in *A. thaliana* displays abnormal cross walls and protracted cytokinesis (Abu-Abied et al., 2018). Our observations taken together with emerging evidence of interactions between RabE and vesicle tethering complexes TRAPP II and the exocyst (Rybak et al., 2014; Mayers et al., 2017b; Kalde et al., 2019) supports our hypothesis of a myosin XI-RabE centric model of polarized transport and growth.

If myosin and RabE interact to support polarized growth, then removal of RabE should impart a deleterious growth phenotype. Although other studies implicated RabE in plant growth in development (Zheng et al., 2005; Speth et al., 2009; Ahn et al., 2013), none comprehensively removed and/or knockdown all present RabE isoforms. Our systematic depletion of RabE through genetic knockouts and RNAi establishes RabE as an essential component of plant growth. Complementation experiments with exogenous *Arabidopsis* Rabs demonstrated a cross-kingdom, RabE specific function in supporting plant growth. This result opened the possibility of an ancient, conserved function between myosin and Rabs in polarized trafficking, with the fundamental information encoded at the interaction interface.

Our systematic depletion of RabE through genetic knockouts and RNAi establishes RabE as an essential component of plant growth. Furthermore, complementation and Y2H experiments with *Arabidopsis* Rabs and myosin XI isoforms demonstrated cross-species functional conservation despite ~450 million years of evolutionary divergence between vascular and non-vascular plants. Additionally, our modeling and experimental validation of the putative MyoXI:RabE interface identified that residue V1422 of the myosin XI-CBD is required for RabE binding and polarized growth. Importantly, V1422 structurally aligns to Q1447 of myosin V in yeast and is required for polarized growth and Rab binding (Schott et al., 1999; Pashkova et al., 2006; Jin et al., 2011). Future work is needed to determine if RabE functions as the direct vesicle receptor of myosin XI. If so, the interaction is likely rapid and transient (Bibeau et al., 2020), which may be challenging to verify biochemically.

Here we demonstrate a remarkable degree of functional conservation between *P. patens* and *A. thaliana* RabE and myosin XI. These results coupled with recent discoveries that established functional homology to the well-characterized yeast system, such as the putative RabE GEF SCD1/SCD2 and exocyst components, supports the enticing hypothesis of a myosin XI/V-driven, pan-eukaryotic mechanism of polarized exocytosis. We anticipate future work will employ this fundamental framework of polarized exocytosis through leveraging experiments in both flowering and basal plants to build additional complexity.

## 3.5 Materials and Methods

### 3.5.1 Yeast Two-Hybrid Assay

A Y2H screen was performed using the services of Hybrigenics (France), and we partnered with them to construct their *Physcomitrella patens* cDNA library. We cultured moss protonemata on PpNO<sub>3</sub> and PpNH<sub>4</sub> medium under standard conditions (Vidali et al., 2007b) for 1-week, then harvested the juvenile tissue and isolated total RNA according to the manufacture's recommendations (Zymo Research Corp. Cat#R1056). The RNA was immediately frozen, then shipped to Hybrigenics where they constructed the cDNA library. The MyoX1a-CCT bait fragment corresponds to residues 1061-1536, was cloned into pB27 (Hybrigenics), and was screened by 132 million pairwise interactions. Positively interacting pairs were identified by growth on SD -Trp -Leu -His.

We validated and performed directed Y2H experiments by cloning into the bait and prey plasmids from Hybrigenics and transforming them into their corresponding Y2H strains, L40 and Y187, respectively. Additional RabEs were inserted into the Y2H prey vector via restriction-based cloning using BamHI and NotI. The *A. thaliana* XIK-CCT Y2H bait vector was created by amplification of the CCT region using the primers in Table S1, then PCR product and pB27 were digested with EcoRI/NotI and ligated. The MyoX1a-CCT bait was mutagenized with the Q5 Site-Directed Mutagenesis Kit (New England BioLabs) to create the V1418R and V1422R mutants. All constructs were sequence verified and all necessary primers are in supplemental table 1. Bait and prey pairs were mated, then grown in SD -Trp -Leu until ~2 OD. All strains were normalized to 0.3 OD, then serially diluted and spotted on SD -Trp -Leu, and SD -Trp -Leu -His plates.

### **3.5.2 Construction of Fluorescently Tagged RabE Moss Lines**

Creation of the 3xmEGFP tagged RabE12 construct occurred by a two-element LR Gateway® reaction (ThermoFisher) of entry clones pENT-L1-3xmEGFP-L5r and pENT-L5-RabE12-L2, and the destination vector pTHUbi-gate (Vidali et al., 2007b). The RabE12 entry clone was generated by amplification of cDNA using primers AttB2-PpRabE12Rev and AttB5-PpRabE12For (Table S1) and a BP reaction with the resulting PCR product and pDONR 221 P5P2. cDNA was created from RNA isolated from 1-week old moss protonemal tissue using the SuperScript III Reverse Transcriptase (ThermoFisher) according to manufacturer's protocol. The 3xmCherry-RabE14 construct was generated in a similar manner using RabE14 cDNA, 3xmCherry entry clone, and the destination vector pTKUbi-gate (Wu and Bezanilla, 2014). The moss expression construct pTHUbi-gate:3xmEGFP-RabE12 was transformed into the Gransden wild-type laboratory strain (Liu and Vidali, 2011) and selected for stable transformants. pTKUbi-gate:3xmCherry-RabE14 was transformed into a previously created line that contains myosin XIa endogenously tagged with 3xmEGFP (Sun et al., 2018), as well as wild-type. This procedure yielded multiple independent transformants that were individually screened for fluorescence.

### **3.5.3 Live-cell Confocal Imaging and Kymograph Analysis**

All moss tissue was cultured as previously described (Furt et al., 2013). All moss lines were imaged with a SP5 confocal microscope (Leica) using the 488 nm and 561 laser lines at 5% power, with the emission bandwidth gated to 499-547 nm light for GFP and 574-652 nm for mCherry. For imaging of cell division, all images (512x512) were acquired simultaneously at 400 Hz using a HCX-PL-Apo, 63x, NA1.4 lens (Leica) with a zoom of 6

and a bit depth of 12-bit. All images were single medial slices with the confocal aperture at 1 AU, taken at 10 second intervals, and a line average of 2 was used to increase signal to noise. Images were processed in ImageJ by Gaussian blurring (Sigma radius 1), background subtracted (200-pixel ball radius), and contrast enhanced (normalized using stack histogram and 0.1% saturated pixels).

For long-term imaging required for kymograph analysis, all images (1024 x 256 pixels) were acquired simultaneously at 400 Hz using with a zoom of 3. Nine optical slices, 1  $\mu\text{m}$  apart, were collected using at five-second intervals to capture the entire volume of the apical cytosol. Total laser power was maintained at 5% for both laser lines. The confocal aperture was opened to 2 AU. For creation of live-cell movies of growing tips, all images were post-processed in ImageJ with blurring (Sigma radius 1) and the red channel was contrast enhanced (normalized per frame using 0.2% saturated pixels) to adjust for acquisition photobleaching.

For cross-correlation analysis, all data were processed and analyzed in an analogous manner to previous work (Furt et al., 2013). To reduce manual ROI selection and to ensure proper ROI orientation for kymograph analysis, as well as to facilitate data processing and visualization, we implemented a custom MATLAB (MathWorks) routine that is available upon request.

### **3.5.4 Homology Modeling and Interface Prediction**

Homology models of the *P.patens* myosin XI cargo-binding domain (MyoXI-CBD) and RabE14 were generated using the SWISS-MODEL server (Waterhouse et al., 2018). The MyoXI-CBD model was created using residues 1131-1537 from full-length myosin XIa

and supplying yeast Myo2p (PDB:2f6h) as the template. The RabE14 model uses the entire protein sequence and is based upon the Sec4 GTP-bound structure (PDB: 1g17).

Subsequent molecular visualization and manipulation was performed using UCSF Chimera (Pettersen et al., 2004). MyoXI-CBD and active RabE14 were structurally aligned with the myosin Vb-Rab11a co-crystal structure (PDB: 4lx0) using the MatchMaker tool with default parameters. The template was removed, and putative interface residues were extracted through identification of atoms whose respective van der Waals surfaces were within 1 Å. This process was repeated with Myo2p and active Sec4 to assess the ability of the method to recapitulate a known myosin V:Rab8-like interaction, irrespective of the template containing a Rab11 member.

We also employed the template-based docking algorithm, PRISM (Tuncbag et al., 2011; Baspinar et al., 2014). With this approach, a predicted interface is generated based on mapping template-to-target interfaces, thereby bypassing other structural elements unrelated to the interface. We used our homology models as the two target proteins and specified the co-crystal structure of human myosin Vb and active Rab11a as the template.

### **3.5.5 CRISPR Knockout of RabE14 and RabE15**

The double  $\Delta$ rabE14/15 mutant was created by gene targeting through CRISPR-Cas9 (Collonnier et al., 2017b). Selection of appropriate guide sequences was done with the CRISPOR platform (Haeussler et al., 2016). The final sgRNAs were chemically synthesized (Integrated DNA Technologies, Coralville, IA, USA). Each sgRNA cassette includes the *P. patens* U6 promoter, the guide sequence target, the tracrRNA scaffold, and are flanked by Gateway® attB sites for BP cloning into pDONR207 (ThermoFisher). All sgRNA constructs were co-transformed with pAct-Cas9 into wild-type *P. patens*

protoplasts and selected for transient transformants on 50 mg L<sup>-1</sup> G418. Successful genomic editing events were verified by genotyping and sequencing (Figure 3.4 and Table 2).

### 3.5.6 RNAi Growth Assays

The loss of RabE phenotype was elucidated using a recently developed RNAi method that allowed us to use the  $\Delta$ rabE14/15 line without the need for reporter insertion (Orr et al., 2020b). To maximize silencing efficacy, our target was 401 bp of the RabE11 coding sequence (CDS) (RabE11i), which shares 88% and 90% identity with RabE12 and RabE13, respectively. The RabE1c expression construct contains the cDNA of *A. thaliana* RabE1c cloned into the pTHUbi-gate vector. RNAi and expression constructs were transformed into either the wild-type or  $\Delta$ rabE14/15 protoplasts, regenerated for 4-days, transferred to growth medium supplemented with 1.25  $\mu$ g mL<sup>-1</sup> 2-FA for 4-days. Plants were stained with calcofluor and imaged 8-days post-transformation to measure morphometric parameters.

The effects on plant growth of myosin XI chimeras and myosin XI point mutants were investigated using a previously developed RNAi methodology (Bezanilla et al., 2005b). Myosin XI chimeras were generated via Gateway® cloning. Briefly, an entry clone containing the *P. patens* Head-Neck-CC domains (pL1-MyoHeadNeckCC-R5) was combined with an entry clone containing either XIK-CCT (pL5-XIK\_CCT-L2) or XIE-CCT (pL5-XIK\_CCT-L2) via an LR Reaction. Myosin XI-CBD mutant expression constructs were created via site-directed mutagenesis of wild-type myosin XIa-CBD (Table S1). The mutant and wild-type CBDs were concatenated with the myosin XIa head, neck, and coiled-coil domains through an LR reaction (ThermoFisher) into the moss expression

construct, pTHUbi-gate. The full-length myosin XI mutant constructs leave a small linker between the two fused pieces, so we created an otherwise wild-type control construct to test for possible deleterious effects of the linker fragment, named '*P.p.* MyoXI.' The myosin XI-CBD expression constructs were co-transformed (Liu and Vidali, 2011) into the NLS-4 line (Bezanilla et al., 2003b) with a previously developed myosin XIa+b 5'UTR silencing construct (Vidali et al., 2010b) to evaluate the capacity of the mutant MyoXI-CBDs to rescue polarized growth. Plants were imaged 1-week post-transformation for polarized growth and size defects (Vidali et al., 2007b; Galotto et al., 2019).

### 3.5.7 Phylogenetic Analysis

The full-length clone identified in our Y2H screen was categorized as RabE14 in accordance with its sequence agreement with the predicted cDNA of gene Pp3c6\_11710 (*Physcomitrella patens* v3.3 (Lang et al., 2018)). We then used the predicted protein sequence and BLAST to analyze the *P.patens* proteome using Phytozome (<http://phytozome.jgi.doe.gov>), as well as *C. subellipsoidea*, *C. reinhardtii*, *V. carteri*, and *A. thaliana*, with an expectation threshold of  $E = 10^{-4}$  and BLOSUM62 substitution matrix. All hits were filtered to allow only putative RabE protein sequences for tree construction. We determined if a given sequence was a RabE using the "Rabifier" (rabdb.org) classification pipeline (Diekmann et al., 2011; Surkont et al., 2017) that predicts if the query sequence is a Rab, and if so, groups it into the most likely Rab subfamily based upon canonical subfamily sequence motifs (Pereira-Leal and Seabra, 2000). We added well-characterized Rab8 proteins Sec4 and Rab8a to observe eukaryotic divergence, as well as a known non-Rab8, Ypt1, to function as the outgroup. Sequences were aligned using MUSCLE (Edgar, 2004) under default parameters. The phylogenetic tree was

constructed under the ML information criterion using PhyML (Guindon et al., 2010), model selection was performed using the Akaike Information Criterion (Akaike, 1974), and 100 bootstraps were executed for statistical branch support. This process was facilitated through use of the ATGC PhyML web server (Guindon et al., 2005).

### **3.5.8 Western Blot Analysis**

Y2H strains were analyzed for MyoXla-CCT expression by picking individual colonies from SD -trp -leu plates, growing to 1 OD600 unit, and extracting total protein via a NaOH and SDS-PAGE buffer treatment (Kushnirov, 2000). Total protein was run on a 12% SDS-PAGE gel, transferred to a PVDF membrane, cut, then blotted against myosin XI-CCT (1:10,000---80kDa) using a custom-made antibody, and yeast ADH1 (1:1,000---40kDa) (Abcam:ab34680) as a loading control. The myosin Xla-CCT antibody was generated against a 6xHis fusion of the myosin Xla-CCT (Capralogics, Inc. Hardiwick, MA).

### **3.5.9 Myosin XI Protoplast Expression**

The mutant and WT myosin Xla expression constructs were reamplified with primers containing attB1 and attB5 sites (Table S1) to facilitate c-terminal tagging with three tandem copies of monomeric enhanced GFP (3mEGFP). Entry clones of myosin XI (WT and mutants) and 3mEGFP were cloned into a moss expression plasmid with LR clonase (Thermo Fisher), yielding pB1-MyoHNC-B5-gtail-*mutation*-B5-3mEGFP-B2. Constructs were transformed into moss protoplast as previously described (Vidali et al., 2007b), except transformed protoplasts were left in suspension in liquid plating medium, instead of being cultured on solid medium.

One day post-transformation, protoplasts were removed from the growth chamber and centrifuged at 250 *g* for five minutes. The supernatant was removed, such that 1ml

remained, and the protoplasts were gently resuspended. Slides for imaging were prepared by affixing an approximately 22x22mm square of Parafilm, with a circle cut out of the center, to a glass microscope slide using heat. Approximately 65  $\mu$ l of protoplasts were transferred to the circle bounded by Parafilm on the slide, then sealed with a 22x22mm glass coverslip. Images of fluorescent protoplasts were acquired using the same equipment described by Bibeau and Vidali (Bibeau and Vidali, 2014).

In brief, protoplasts were imaged using three separate filters: chlorophyll channel (480/40 bandpass excitation filter, 505 longpass dichroic, 510 longpass emission); standard GFP filter (for GFP expression); standard dsRed filter (dead cells/background subtraction). All three images were imported into ImageJ, contrast enhanced, then the dsRed signal was subtracted from the GFP channel to avoid quantification of dead protoplasts. The red channel was used to visualize the protoplast morphology and was manually segmented using the magic wand tool and ROI manager. The mean gray values for all ROIs were measured on the GFP channel and exported. All fluorescent values were filtered based on the fluorescence of the “no DNA” condition—the maximum value obtained within the “no DNA” condition was used as a threshold for all other conditions for that respective day to discard untransformed or non-expressing protoplasts. The remaining values were averaged by date of transformation for each condition and tested for statistical differences.

### **3.5.10 Myosin XI-CCT Purification**

The myosin XIa-CCT *E. coli* expression construct was created by primers (Table 2) that amplified residues 1061-1537 and then cloned into the pETDuet vector using restriction

enzymes BamHI and HindIII. Myosin XI mutants were generated for purification using the Q5 Mutagenesis Kit (New England BioLabs) using the previously created mutagenesis primers for protoplast expression and the wild-type MyoXIa-CCT *E. coli* expression construct as the template.

Myosin XIa-CCT expression constructs were transformed into BL21 (DE3) *E. coli*, transferred to liquid culture and grown until OD<sub>600</sub> ~0.6, then shifted to 15°C and induced with 0.1 mM IPTG after cooling. Cells were incubated overnight at 15°C. Harvested cells were resuspended (~20 ml lysis buffer/L of culture) in cold lysis buffer (50 mM NaH<sub>2</sub>PO<sub>4</sub> pH 8.0, 300 mM NaCl, 10mM imidazole, 10% (v/v) glycerol, fresh 5mM β-mercaptoethanol, 1mM PMSF, DNase, and 1 cOmplete Protease Inhibitor Cocktail tablet (Roche Diagnostics) added prior to lysis, then lysed using a microfluidizer M-110S (Microfluidics) at 80 psi. The cleared lysate was batch bound to Ni-NTA agarose beads (Qiagen) for 1 h at 4°C, then packed via gravity flow. The Ni-NTA column was washed (50 mM NaH<sub>2</sub>PO<sub>4</sub> pH8.0, 300 mM NaCl, 20 mM imidazole, 10% (v/v) glycerol, fresh 5 mM β-mercaptoethanol), then eluted with the same buffer plus 250 mM imidazole. Fractions containing protein were pooled and subjected to an anion exchange purification step on a MonoQ 10/10 column (GE LifeSciences), controlled using an ÄKTA pure FPLC (GE LifeSciences).

### **3.5.11 Statistical Analyses**

All statistical analyses were performed using GraphPad Prism. All error bars represent a 95% confidence interval unless otherwise specified. For all experiments, statistical significance was determined by a one-way ANOVA with a post-hoc Tukey test ( $P < 0.01$ ) unless otherwise specified in the figure legend.

**Table 2:** Primers used in this study.

<b>Primer Name</b>	<b>Primer Sequence</b>	<b>Entry clone</b>	<b>Use</b>
AttB1 Myo Head Neck For	GGGGACAAGTTTGTACAAAAAAGC AGGCTTAATGGCGACAGCAGGGAA TGTA	pL1-MyoHeadNeck-R5	Phenotype/Complementation
AttB5r Myo Head Neck Rev	GGGGACAAC TTTTGTATACAAAGTT GTACCCTTGGTCGGTGACAATAC	pL1-MyoHeadNeck-R5	Phenotype/Complementation
AttB5 Myo CC Tail For	GGGGACAAC TTTTGTATACAAAGTT GTGTTGTCTGAATCGATTCAAAGCA CCG	pL5-MyoCC Tail-L2	Phenotype/Complementation
AttB2 Myo CC Tail Rev	GGGGACCACTTTGTACAAGAAAGC TGGGTACTAAGAATCTGGTTGTGG	pL5-MyoCC Tail-L2	Phenotype/Complementation
AttB1 Myo Head Neck CC For	GGGGACAAGTTTGTACAAAAAAGC AGGCTTAATGGCGACAGCAGGGAA TGTA	pL1-MyoHeadNeckC-R5	Phenotype/Complementation
AttB5r Myo Head Neck CC Rev	GGGGACAAC TTTTGTATACAAAGTT GTCAAAGAGTCTTGATTCTCCTGCT	pL1-MyoHeadNeckC-R5	Phenotype/Complementation
AttB5 Myo Tail For	GGGGACAAC TTTTGTATACAAAGTT GTGCTGCAATGTGTCATGCAAGAT	pL5-MyoTail-L2	Phenotype/Complementation
AttB2 Myo Tail Rev	GGGGACCACTTTGTACAAGAAAGC TGGGTACTAAGAATCTGGTTGTGG	pL5-MyoTail-L2	Phenotype/Complementation
Myo F1379R For	CGTGAGTGTTGCTCACGTAGCAAC GGAGAGTAT	pL5-MyoTail F1379R-L2	Phenotype/Complementation
Myo F1379R Rev	TCTCAGCAGCAAAC TGTGAAACAG CTGAACATT	pL5-MyoTail F1379R-L2	Phenotype/Complementation
Myo V1418R For	TATATCCGACAAGCACGTGGATTTT TGGTCATTCATC	pL5-MyoTail V1418R-L2	Phenotype/Complementation/Purification

Myo V1418R Rev	CTTGAGCTCATCCCATGACGCTCC AGCATACTC	pL5- MyoTail V1418R -L2	Phenotype/Compl ementation/Purific ation
Myo V1422R For	GCAGTTGGATTTTTGCGCATTTCATC AAAAGCCA	pL5- MyoTail V1422R -L2	Phenotype/Compl ementation/Purific ation
Myo V1422R Rev	TTGTCGGATATACTTGAGCTCATCC CATGACGCTCC	pL5- MyoTail V1422R -L2	Phenotype/Compl ementation/Purific ation
Myo W1408R For	TATGCTGGAGCGTCACGGGATGAG CTCAAGTAT	pL5- MyoTail W1408 R-L2	Phenotype/Compl ementation
Myo W1408R Rev	CTCCTCCCCAGCTTCATAAATCCAG TGCTCTAGTTCTG	pL5- MyoTail W1408 R-L2	Phenotype/Compl ementation
Myo Y1384R For	TTTAGCAACGGAGAGCGTGTGAAA GCTGGACTT	pL5- MyoTail Y1384R -L2	Phenotype/Compl ementation
Myo Y1384R Rev	TGAGCAACACTCACGTCTCAGCAG CAAAGTGT	pL5- MyoTail Y1384R -L2	Phenotype/Compl ementation
MyoXla-CCT WT For	CGCGGATCCGTTGTCTGAATCGATT CAAAGC	n/a	BamHI site for cloning into pETDuet/Purificati on
MyoXla-CCT WT Rev	CCCAAGCTTCTAAGAATCTGGTTGT GGCATTAG	n/a	HindIII site for cloning into pETDuet/Purificati on
AttB2- PpRabE12 Rev	GGGGACCACTTTGTACAAGAAAGC TGGGTACTACGAGCAGCAGGAAGT AGA	pL5- RabE12 -pL2	Subcellular localization of RabE12/3xmEGF P tagging
AttB5- PpRabE12 For	GGGGACAACCTTTGTATACAAAAGTT GTGATGGCCGCAGGTGGATCAAGA	pL5- RabE12 -pL2	Subcellular localization of RabE12/3xmEGF P tagging

AttB5-PpRabE14 For	GGGGACAACCTTTGTATACAAAAGTT GTGATGGCGACAAGAGCCC	pL5-RabE14 -pL2	Subcellular localization of RabE14/3xmEGF P tagging
AttB5-PpRabE14 Rev	GGGGACCACTTTGTACAAGAAAGC TGGGTACTATGAGCAGCAAGAGCC AGA	pL5-RabE14 -pL2	Subcellular localization of RabE14/3xmEGF P tagging
RabE11CDS _NotI_Forward	TAAGCAGCGGCCGCAATGGCCGCA GGTGGATC	y2hPrey - RabE11	RabE11 full-length in Y2H prey vector
RabE11CDS _BamHI_Reverse	TGCTTAGGATCCTCAAGAGCAACA GGAGCTACC	y2hPrey - RabE11	RabE11 full-length in Y2H prey vector
RabE15CDS _NotI_Forward	TAAGCAGCGGCCGCAATGGCGACA AGAGCTCGG	y2hPrey - RabE15	RabE15 full-length in Y2H prey vector
RabE15CDS _BamHI_Reverse	TGCTTAGGATCCCTATGAGCAGCA AGAGCCAGA	y2hPrey - RabE15	RabE15 full-length in Y2H prey vector
Y2Hprey_Forward	AATACCACTACAATGGAT	n/a	Sequencing primer for Y2H prey vector
Y2Hprey_Reverse	TCTAGACACTAGCTACTC	n/a	Sequencing primer for Y2H prey vector
RabE11i_Reverse	GGGGACCACTTTGTACAAGAAAGC TGGGTAGCTTGACCCTTCGCAGTGG	pL1-RabE11 i-L2	Primer to amplify 401bp of RabE11 CDS for RNAi
RabE11i_Forward	GGGGACAAGTTTGTACAAAAAAGC AGGCTTAGATTACCTCATCAAGCTGCT	pL1-RabE11 i-L2	Primer to amplify 401bp of RabE11 CDS for RNAi
RabE14_P2-F	AGTTTGGAGGGATGCTGAGTG	n/a	RabE14 CRISPR genotyping
RabE14_P2-R	GAGCCTGACCTTTGGCAAAG	n/a	RabE14 CRISPR genotyping
RabE14_P1-F	TGCACATATTGCACAAACAGTCA	n/a	RabE14 CRISPR genotyping
RabE14_P1-R	AACATCACGTTCCCTTCATTTCT	n/a	RabE14 CRISPR genotyping
RabE15_P2-F	CAGAGAGGCGGGTTTTGTAGT	n/a	RabE15 CRISPR genotyping
RabE15_P2-R	CCTCCGAAATGGTCCCAAGAA	n/a	RabE15 CRISPR genotyping
RabE15F_P1-F	CTAAGCCTTGCTAATGTAAACCA	n/a	RabE15 CRISPR genotyping

RabE15F_P1 -R	ACAACGTTAGGTTAACAACACACT	n/a	RabE15 CRISPR genotyping
XIK- CCT_EcoRI For	TAAGCAGAATTCATGCTTTTACCGA GAACTCC	y2hBait- XIK CCT	<i>A. thaliana</i> XIK CCT Y2H bait vector
XIK- CCT_NotI Rev	TAAGCAGCGGCCGCTTACGATGTA CTGCCTTCT	y2hBait- XIK CCT	<i>A. thaliana</i> XIK CCT Y2H bait vector
XIK- CCT_attB5	GGGGACAACCTTTGTATACAAAAGTT GTGATGGCCACACGATCAAAAACA	pL5- XIK_CC T-L2	Creation of chimeric myosin XI with XI-K CCT
XIK- CCT_attB2	GGGGACCACTTTGTACAAGAAAGC TGGGTATTACGATGTACTGCCTTCT TTACG	pL5- XIK_CC T-L2	Creation of chimeric myosin XI with XI-K CCT
XIE- CCT_attB5	GGGGACAACCTTTGTATACAAAAGTT GTGTTTCTCTCTGGCCGGTCC	pL5- XIE_CC T-L2	Creation of chimeric myosin XI with XI-E CCT
XIE- CCT_attB2	GGGGACCACTTTGTACAAGAAAGC TGGGTATTAGTCAGAACATGGCAAT AGAAAG	pL5- XIE_CC T-L2	Creation of chimeric myosin XI with XI-E CCT

**Table 3:** Gene IDs and source of protein sequences used in phylogenetic tree construction

Name	Description	Sequence Length
<i>Volvox carteri</i>	Vocar.0012s0034.1 (Phytozome)	217
<i>S.c. Ypt1</i>	P01123 (Uniprot)	206
<i>Coccomyxa subellipsoidea</i>	26393 (Phytozome)	210
<i>Chlamydomonas reinhardtii</i>	Cre15.g641800.t1.2 (Phytozome)	183
<i>H.s. Rab8a</i>	P61006 (Uniprot)	207
<i>A.t. RabE1E</i>	At3g09900 (Phytozome-TAIR10)	218
<i>A.t. RabE1D</i>	At5g03520 (Phytozome-TAIR10)	216
<i>A.t. RabE1B</i>	AT5G59840 (Phytozome-TAIR10)	216
<i>A.t. RabE1A</i>	At3g53610 (Phytozome-TAIR10)	216
<i>A.t. RabE1C</i>	At3g46060 (Phytozome-TAIR10)	216
<i>P.p. RabE15</i>	Pp3c5_21410 (Phytozome-Pp v3.3)	215

<i>P.p. RabE13</i>	Pp3c25_7430 (Phytozome-Pp v3.3)	216
<i>P.p. RabE14</i>	Pp3c6_11710 (Phytozome-Pp v3.3)	215
<i>P.p. RabE11</i>	Pp3c16_17460 (Phytozome-Pp v3.3)	216
<i>P.p. RabE12</i>	Pp3c16_17470 (Phytozome-Pp v3.3)	216
<i>S.c. Sec4</i>	P07560 (Uniprot)	215

## **Chapter 4 : Future Directions and Conclusions**

---

## 4.1 Extension of the APTi System for Long-Term Imaging and Conditional Activation

Chapter 2 demonstrated the potency and flexibility of the APTi system to simultaneously silence multiple genes. However, I believe there are two fundamental areas where, if addressed, would make the APTi system an even more attractive tool to the community. The first area of improvement is applying long-term imaging to APTi experiments. In Chapter 2, the phenotype profiling of APTi plants was done as an end-point analysis. While informative and easy for other labs to quickly adopt, end-point profiling fails to capture the dynamic and developmental information long-term imaging provides. For example, two independent mutants may display an indistinguishable end-point morphological phenotype. Long-term imaging enables extraction of additional characteristics, such as growth rate or time to cell division, thereby enabling effective distinction of the mutants. I demonstrated a proof-of-principle experiment in Chapter 3 where I imaged APTi plants over a 24-hour period to determine the growth rate. Despite the success of this approach, there are several limitations. The imaging was performed on a standard widefield fluorescent microscope with low magnification, and the plants were grown on a self-contained agar support. This experimental design precludes any perturbation and recovery experiments, such as observing how an APTi-mediated mutant responds to a drug, or single-particle imaging. Fortunately, both limitations can be resolved by growth in microfluidic chambers. *P. patens* has been successfully grown in microfluidic chambers for long-term imaging, drug treatments, and single-particle imaging (Bascom et al., 2016; Kozgunova and Goshima, 2019; Sakai et al., 2019). Translating the APTi system to microfluidics is an exciting future prospect, as it will enable even more

sophisticated experiments. For example, in Chapter 3 I demonstrated the requirement of RabE and its interaction with myosin XI for polarized growth. I hypothesize this is because RabE functions as the secretory vesicle receptor for myosin XI. Therefore, using microfluidics and APTi I could examine secretory vesicle dynamics in the *rabE* mutant, with the prediction that vesicles in the *rabE* plant display slower and/or less directed motion than wild-type.

RNAi-based techniques, such as APTi, are advantageous because they allow investigation of essential genes that are non-viable using traditional knockout approaches. Despite this advantage, traditional RNAi approaches and the current APTi system typically result in homogenous silencing across the entire organism. This limitation prevents precise investigation of gene silencing within a particular cell type or induction of RNAi at a defined developmental stage. To address this, inducible systems have been constructed to allow controlled activation of RNAi (Guo et al., 2003; Nakaoka et al., 2012; Liu and Yoder, 2016). I envision the next generation of APTi to facilitate stable integration into the genome and utilize the XVE estrogen-inducible system (Zuo et al., 2000), which has been successfully applied in *P. patens* (Nakaoka et al., 2012; MacVeigh-Fierro et al., 2017). Development of an inducible APTi system is complemented by a robust long-term imaging platform, as discussed above. Together, these two advancements will significantly improve an already versatile and efficacious system.

#### **4.2 Further Characterization of the Myosin XI:RabE Interaction**

Despite my best efforts, I was unable to reconstitute direct binding of myosin XI to RabE *in vitro*. I attempted traditional equilibrium binding experiments using a quantitative GST pull down assay (Pollard, 2010), as well as using microscale thermophoresis (Wienken

et al., 2010). I speculate that the myosin XI:RabE dissociation constant is high to facilitate the dynamic fluctuations we observe at the growing tip, which would affect my ability to detect the interaction. Furthermore, it is possible myosin XI interacting with RabE is not a simple binary interaction. Rather, additional components, such as phosphoinositides, could coordinate with membrane-localized RabE to impart a coincidence detection mechanism for specific myosin XI recruitment (Jean and Kiger, 2012). Nevertheless, through this endeavor I established reproducible methods to purify recombinant *P. patens* myosin XI and RabE14 from *E. coli*. Although I could purify large quantities of soluble protein, it is currently unknown if the proteins are functional. Recombinant RabE14 could be tested for functionality using a fluorescent nucleotide exchange assay, but at present there is no basis to compare the kinetic results with. A similar but larger problem exists for myosin XI, as very few known interacting partners exist, and none have been demonstrated with *P. patens* to my knowledge.

To avoid the uncertainty inherent to biochemical reconstitution, *in vivo* detection of protein-protein interactions presents a favorable alternative. In Chapter 3 I demonstrated a strong spatiotemporal correlation between RabE14 and myosin XI, but one cannot conclude a direct interaction through this type of observation. Biofluorescence complementation (BiFC) is a popular technique to identify protein-protein interactions in the plant cell biology field due to its ease of use (Xing et al., 2016; Struk et al., 2019). BiFC only requires expression of the two proteins of interest each fused to a fragment of a fluorescent protein—if the two fusion proteins come within a critical distance, the fragments will reconstitute a functional fluorescent protein. Despite multiple caveats of BiFC, the irreversible nature makes it an enticing option to detect weak and transient

interactions as the signal will accumulate over time. With proper controls, such as alternative proteins or specific mutations thought to disrupt the interaction, true interaction signal can be distinguished from the background (Kudla and Bock, 2016). Therefore, I attempted BiFC as an orthogonal approach to test the myosin XI:RabE interaction. To accomplish this, I cloned full-length myosin XI and RabE14 into BiFC vectors that enable ratiometric quantitation of the BiFC signal to an internal red fluorescent protein (RFP) signal (Grefen and Blatt, 2012), which also functions as a positive transformation and expression control. I transformed the BiFC plasmid into *P. patens* protoplasts and observed no BiFC signal (yellow fluorescent protein, YFP), but I also observed no positive RFP signal. As *P. patens* transformation is typically highly efficient (Liu and Vidali, 2011) and I have much personal experience, I suspected the promotor of the BiFC construct resulted in low expression within *P. patens* protoplasts. As this BiFC construct was successfully used in protoplasts of *A. thaliana* (Albert et al., 2015; Stockle et al., 2016), I tested my constructs using *Arabidopsis* mesophyll protoplasts. I observed a few RFP positive protoplasts, but at a frequency well below what the literature suggests as an acceptable transformation. This was not unexpected, as *A. thaliana* protoplasts are notoriously more difficult to work with. Further optimization of the protoplasting and transformation protocol may yield promising results. Alternatively, discovery methods such as affinity purification followed by mass spectrometry (AP-MS) (Van Leene et al., 2015) or proximity-dependent labeling (Kim and Roux, 2016; Branon et al., 2018) are powerful techniques to uncover interactions and higher order protein complexes.

The work of Chapter 3 was motivated by a long-standing vesicle organizing center model of polarized growth (Furt et al., 2013). This model was based upon phenomena in

*P. patens* and research demonstrating that vesicle-localized actin nucleators and a myosin receptor were sufficient to organize myosin-mediated vesicle transport (Schuh, 2011). In this animal system, a Rab GTPase was the vesicle receptor of myosin V, which also occurs in yeast (Jin et al., 2011) and humans (Pylypenko et al., 2016; Alzahofi et al., 2020). The data presented in Chapter 3 is highly supportive of a myosin XI:RabE interaction, but does not establish RabE as the vesicle-localized receptor for myosin XI. Biochemical experiments, such as vesicle purification, will be instrumental in determining if RabE is localized to the vesicle and could also serve to create a molecular census of what proteins reside on a *P. patens* secretory vesicle.

### **4.3 Conclusions**

Previously, despite considerable experimental and mathematical modeling data describing plant polarized growth, our mechanistic understanding of this superficially basic process is underdeveloped relative to other eukaryotic systems. This is likely a consequence of multiple gene duplication events endemic to the land plants, as well as many plant species of interest being recalcitrant to traditional transformation and genetic modification. To this end, the work in this dissertation attempted to both serve a dire need within the community for potent tools to silence gene families, as well as uncover mechanistic insights into how cells achieve polarized growth. As a result, I (with the help of others) developed a novel RNAi methodology that is the first of its kind to enable positive selection of actively silencing plants. I demonstrated the efficacy and versatility of this technique to silence two different gene families, myosin XI(a,b) and Lyk5(a,b,c). In addition, through a combination of structural modeling, gene editing, yeast two-hybrid, chimeric proteins, cross-species complementation, and quantitative microscopy I

identified an interaction between myosin XI and the RabE GTPase family. Furthermore, I demonstrated the conservation of this interaction through complementation with myosin XI and RabE from the distantly related vascular plant, *A. thaliana*. Together, this work represents a substantial step forward in our understanding of plant polarized growth, and the underlying polarized trafficking process that supports growth. Both these insights and the new APTi system should inform and assist future experiments to build upon our growing knowledge of the dynamic and interconnected processes that promote and sustain polarized growth in plants.

## Chapter 5 : References

---

- Abu-Abied, M., Belausov, E., Hagay, S., Peremyslov, V., Dolja, V., and Sadot, E.** (2018). Myosin XI-K is involved in root organogenesis, polar auxin transport, and cell division. *Journal of Experimental Botany* **69**, 2669-2881.
- Ahn, C.S., Han, J.A., and Pai, H.S.** (2013). Characterization of in vivo functions of *Nicotiana benthamiana* RabE1. *Planta* **237**, 161-172.
- Akaike, H.** (1974). A new look at the statistical model identification. *IEEE Trans. Autom. Control* **19**, 716-723.
- Albert, I., Bohm, H., Albert, M., Feiler, C.E., Imkampe, J., Wallmeroth, N., Brancato, C., Raaymakers, T.M., Oome, S., Zhang, H., Krol, E., Grefen, C., Gust, A.A., Chai, J., Hedrich, R., Van den Ackerveken, G., and Nurnberger, T.** (2015). An RLP23-SOBIR1-BAK1 complex mediates NLP-triggered immunity. *Nat Plants* **1**, 15140.
- Allen, M., Qin, W.S., Moreau, F., and Moffatt, B.** (2002). Adenine phosphoribosyltransferase isoforms of *Arabidopsis* and their potential contributions to adenine and cytokinin metabolism. *Physiologia Plantarum* **115**, 56-68.
- Alvarez, A., Montesano, M., Schmelz, E., and de Leon, I.P.** (2016). Activation of shikimate, phenylpropanoid, oxylipins, and auxin pathways in *Pectobacterium carotovorum* elicitors-treated moss. *Front Plant Sci* **7**.
- Alzahofi, N., Welz, T., Robinson, C.L., Page, E.L., Briggs, D.A., Stainthorp, A.K., Reekes, J., Elbe, D.A., Straub, F., Kallemeijn, W.W., Tate, E.W., Goff, P.S., Sviderskaya, E.V., Cantero, M., Montoliu, L., Nedelec, F., Miles, A.K., Bailly, M., Kerkhoff, E., and Hume, A.N.** (2020). Rab27a co-ordinates actin-dependent transport by controlling organelle-associated motors and track assembly proteins. *Nat Commun* **11**, 3495.
- Anzalone, A.V., Randolph, P.B., Davis, J.R., Sousa, A.A., Koblan, L.W., Levy, J.M., Chen, P.J., Wilson, C., Newby, G.A., Raguram, A., and Liu, D.R.** (2019). Search-and-replace genome editing without double-strand breaks or donor DNA. *Nature* **576**, 149+.
- Arif, M.A., Frank, W., and Khraiweh, B.** (2013). Role of RNA interference (RNAi) in the moss *Physcomitrella patens*. *Int. J. Mol. Sci.* **14**, 1516-1540.
- Ashihara, H., Stasolla, C., Fujimura, T., and Crozier, A.** (2018). Purine salvage in plants. *Phytochemistry* **147**, 89-124.
- Ashton, N.W., Grimsley, N.H., and Cove, D.J.** (1979). Analysis of gametophytic development in the moss, *Physcomitrella patens*, using auxin and cytokinin resistant mutants. *Planta* **144**, 427-435.
- Augustine, R.C., Vidali, L., Kleinman, K.P., and Bezanilla, M.** (2008). Actin depolymerizing factor is essential for viability in plants, and its phosphoregulation is important for tip growth. *Plant J* **54**, 863-875.
- Augustine, R.C., Pattavina, K.A., Tuzel, E., Vidali, L., and Bezanilla, M.** (2011). Actin interacting protein1 and actin depolymerizing factor drive rapid actin dynamics in *Physcomitrella patens*. *Plant Cell* **23**, 3696-3710.
- Bascom, C., Burkart, G.M., Mallett, D.R., O'Sullivan, J.E., Tomaszewski, A.J., Walsh, K., and Bezanilla, M.** (2019a). Systematic survey of the function of ROP regulators and effectors during tip growth in the moss *Physcomitrella patens*. *J. Exp. Bot.* **70**, 447-457.
- Bascom, C., Jr., Burkart, G.M., Mallett, D.R., O'Sullivan, J.E., Tomaszewski, A.J., Walsh, K., and Bezanilla, M.** (2019b). Systematic survey of the function of ROP regulators and effectors during tip growth in the moss *Physcomitrella patens*. *J Exp Bot* **70**, 447-457.
- Bascom, C.S., Wu, S.Z., Nelson, K., Oakey, J., and Bezanilla, M.** (2016). Long-Term Growth of Moss in Microfluidic Devices Enables Subcellular Studies in Development. *Plant Physiol.* **172**, 28-37.
- Baspinar, A., Cukuroglu, E., Nussinov, R., Keskin, O., and Gursoy, A.** (2014). PRISM: a web server and repository for prediction of protein-protein interactions and modeling their 3D complexes. *Nucleic Acids Res* **42**, W285-289.

- Basu, D., Le, J., Zakharova, T., Mallery, E.L., and Szymanski, D.B.** (2008). A SPIKE1 signaling complex controls actin-dependent cell morphogenesis through the heteromeric WAVE and ARP2/3 complexes. *Proc. Natl. Acad. Sci. U. S. A.* **105**, 4044-4049.
- Baulcombe, D.** (2004). RNA silencing in plants. *Nature* **431**, 356-363.
- Beike, A.K., von Stackelberg, M., Schallenberg-Rudinger, M., Hanke, S.T., Follo, M., Quandt, D., McDaniel, S.F., Reski, R., Tan, B.C., and Rensing, S.A.** (2014). Molecular evidence for convergent evolution and allopolyploid speciation within the *Physcomitrium-Physcomitrella* species complex. *BMC Evol. Biol.* **14**.
- Bezanilla, M., Pan, A., and Quatrano, R.S.** (2003a). RNA interference in the moss *Physcomitrella patens*. *Plant Physiol* **133**, 470-474.
- Bezanilla, M., Pan, A., and Quatrano, R.S.** (2003b). RNA interference in the moss *Physcomitrella patens*. *Plant Physiology* **133**, 470-474.
- Bezanilla, M., Perroud, P.F., Pan, A., Klueh, P., and Quatrano, R.S.** (2005a). An RNAi system in *Physcomitrella patens* with an internal marker for silencing allows for rapid identification of loss of function phenotypes. *Plant Biol (Stuttg)* **7**, 251-257.
- Bezanilla, M., Perroud, P.-F., Pan, A., Klueh, P., and Quatrano, R.S.** (2005b). An RNAi system in *Physcomitrella patens* with an internal marker for silencing allows for rapid identification of loss of function phenotypes. *Plant Biology* **7**, 251-257.
- Bi, E.F., and Park, H.O.** (2012). Cell Polarization and Cytokinesis in Budding Yeast. *Genetics* **191**, 347-387.
- Bibeau, J.P., and Vidali, L.** (2014). Morphological analysis of cell growth mutants in *Physcomitrella*. *Methods Mol Biol* **1080**, 201-213.
- Bibeau, J.P., Kingsley, J.L., Furt, F., Tuzel, E., and Vidali, L.** (2018a). F-Actin Mediated Focusing of Vesicles at the Cell Tip Is Essential for Polarized Growth. *Plant Physiol* **176**, 352-363.
- Bibeau, J.P., Kingsley, J.L., Furt, F., Tuzel, E., and Vidali, L.** (2018b). F-Actin Mediated Focusing of Vesicles at the Cell Tip Is Essential for Polarized Growth. *Plant Physiol.* **176**, 352-363.
- Bibeau, J.P., Furt, F., Mousavi, S.I., Kingsley, J.L., Levine, M.F., Tuzel, E., and Vidali, L.** (2020). In vivo interactions between myosin XI, vesicles and filamentous actin are fast and transient in *Physcomitrella patens*. *J Cell Sci* **133**.
- Bloch, D., Pleskot, R., Pejchar, P., Potocky, M., Trpkosova, P., Cwiklik, L., Vukasinovic, N., Sternberg, H., Yalovsky, S., and Zarsky, V.** (2016). Exocyst SEC3 and Phosphoinositides Define Sites of Exocytosis in Pollen Tube Initiation and Growth. *Plant Physiol.* **172**, 980-1002.
- Bove, J., Vaillancourt, B., Kroeger, J., Hepler, P.K., Wiseman, P.W., and Geitmann, A.** (2008). Magnitude and direction of vesicle dynamics in growing pollen tubes using spatiotemporal image correlation spectroscopy and fluorescence recovery after photobleaching. *Plant physiology* **147**, 1646-1658.
- Bowers, J.E., Chapman, B.A., Rong, J.K., and Paterson, A.H.** (2003). Unravelling angiosperm genome evolution by phylogenetic analysis of chromosomal duplication events. *Nature* **422**, 433-438.
- Bowman, J.L., Kohchi, T., Yamato, K.T., Jenkins, J., Shu, S.Q., Ishizaki, K., Yamaoka, S., Nishihama, R., Nakamura, Y., Berger, F., Adam, C., Aki, S.S., Althoff, F., Araki, T., Arteaga-Vazquez, M.A., Balasubramanian, S., Barry, K., Bauer, D., Boehm, C.R., Briginshaw, L., Caballero-Perez, J., Catarino, B., Chen, F., Chiyoda, S., Chovatia, M., Davies, K.M., Delmans, M., Demura, T., Dierschke, T., Dolan, L., Dorantes-Acosta, A.E., Eklund, D.M., Florent, S.N., Flores-Sandoval, E., Fujiyama, A., Fukuzawa, H., Galik, B., Grimanelli, D., Grimwood, J., Grossniklaus, U., Hamada, T., Haseloff, J., Hetherington, A.J., Higo, A., Hirakawa, Y., Hundley, H.N., Ikeda, Y., Inoue, K., Inoue, S.I., Ishida, S., Jia, Q.D., Kakita, M., Kanazawa, T., Kawai, Y., Kawashima, T., Kennedy, M., Kinose, K., Kinoshita, T., Kohara, Y., Koide, E., Komatsu, K., Kopischke, S., Kubo, M., Kyojuka, J., Lagercrantz, U., Lin, S.S., Lindquist, E., Lipzen, A.M., Lu, C.W., De Luna, E., Martienssen, R.A., Minamino, N., Mizutani, M., Mizutani, M., Mochizuki, N., Monte, I., Mosher, R., Nagasaki, H., Nakagami, H., Naramoto, S., Nishitani, K., Ohtani, M., Okamoto, T., Okumura, M., Phillips, J.,**

- Pollak, B., Reinders, A., Rovekamp, M., Sano, R., Sawa, S., Schmid, M.W., Shirakawa, M., Solano, R., Spunde, A., Suetsugu, N., Sugano, S., Sugiyama, A., Sun, R., Suzuki, Y., Takenaka, M., Takezawa, D., Tomogane, H., Tsuzuki, M., Ueda, T., Umeda, M., Ward, J.M., Watanabe, Y., Yazaki, K., Yokoyama, R., Yoshitake, Y., Yotsui, I., Zachgo, S., and Schmutz, J. (2017). Insights into Land Plant Evolution Garnered from the *Marchantia polymorpha* Genome. *Cell* **171**, 287-+.
- Bracha, D., Walls, M.T., Wei, M.T., Zhu, L., Kurian, M., Avalos, J.L., Toettcher, J.E., and Brangwynne, C.P. (2018). Mapping Local and Global Liquid Phase Behavior in Living Cells Using Photo-Oligomerizable Seeds. *Cell* **175**, 1467-+.
- Branon, T.C., Bosch, J.A., Sanchez, A.D., Udeshi, N.D., Svinkina, T., Carr, S.A., Feldman, J.L., Perrimon, N., and Ting, A.Y. (2018). Efficient proximity labeling in living cells and organisms with TurboID. *Nat. Biotechnol.* **36**, 880-887.
- Bressendorff, S., Azevedo, R., Kenchappa, C.S., de Leon, I.P., Olsen, J.V., Rasmussen, M.W., Erbs, G., Newman, M.A., Petersen, M., and Mundy, J. (2016). An innate immunity pathway in the moss *Physcomitrella patens*. *Plant Cell* **28**, 1328-1342.
- Burkart, G.M., Baskin, T.I., and Bezanilla, M. (2015). A family of ROP proteins that suppresses actin dynamics, and is essential for polarized growth and cell adhesion. *J. Cell Sci.* **128**, 2553-2564.
- Byzova, M., Verduyn, C., De Brouwer, D., and De Block, M. (2004). Transforming petals into sepaloid organs in *Arabidopsis* and oilseed rape: implementation of the hairpin RNA-mediated gene silencing technology in an organ-specific manner. *Planta* **218**, 379-387.
- Camacho, L., Smertenko, A.P., Perez-Gomez, J., Hussey, P.J., and Moore, I. (2009). Arabidopsis Rab-E GTPases exhibit a novel interaction with a plasma-membrane phosphatidylinositol-4-phosphate 5-kinase. *Journal of Cell Science* **122**, 4383-4392.
- Campas, O., and Mahadevan, L. (2009). Shape and dynamics of tip-growing cells. *Curr Biol* **19**, 2102-2107.
- Cao, Y.R., Liang, Y., Tanaka, K., Nguyen, C.T., Jedrzejczak, R.P., Joachimiak, A., and Stacey, G. (2014). The kinase LYK5 is a major chitin receptor in *Arabidopsis* and forms a chitin-induced complex with related kinase CERK1. *Elife* **3**.
- Case, L.B., Zhang, X., Ditlev, J.A., and Rosen, M.K. (2019). Stoichiometry controls activity of phase-separated clusters of actin signaling proteins. *Science* **363**, 1093-1097.
- Ceccaldi, R., Rondinelli, B., and D'Andrea, A.D. (2016). Repair Pathway Choices and Consequences at the Double-Strand Break. *Trends Cell Biol.* **26**, 52-64.
- Cermak, T., Baltes, N.J., Cegan, R., Zhang, Y., and Voytas, D.F. (2015). High-frequency, precise modification of the tomato genome. *Genome Biol.* **16**.
- Charlot, F., Chelysheva, L., Kamisugi, Y., Vrielynck, N., Guyon, A., Epert, A., Le Guin, S., Schaefer, D.G., Cuming, A.C., Grelon, M., and Nogue, F. (2014). RAD51B plays an essential role during somatic and meiotic recombination in *Physcomitrella*. *Nucleic Acids Research* **42**, 11965-11978.
- Chatterjee, P., Jakimo, N., Lee, J., Amrani, N., Rodriguez, T., Koseki, S.R.T., Tysinger, E., Qing, R., Hao, S.L., Sontheimer, E.J., and Jacobson, J. (2020). An engineered ScCas9 with broad PAM range and high specificity and activity. *Nat. Biotechnol.*
- Chen, K.L., Wang, Y.P., Zhang, R., Zhang, H.W., and Gao, C.X. (2019). CRISPR/Cas Genome Editing and Precision Plant Breeding in Agriculture. *Annual Review of Plant Biology*, Vol 70 **70**, 667-697.
- Chen, T.W., Wardill, T.J., Sun, Y., Pulver, S.R., Renninger, S.L., Baohan, A., Schreiter, E.R., Kerr, R.A., Orger, M.B., Jayaraman, V., Looger, L.L., Svoboda, K., and Kim, D.S. (2013). Ultrasensitive fluorescent proteins for imaging neuronal activity. *Nature* **499**, 295-+.
- Choulika, A., Perrin, A., Dujon, B., and Nicolas, J.F. (1995). Induction of Homologous Recombination in Mammalian Chromosomes by Using the I-SceI System of *Saccharomyces cerevisiae*. *Molecular and Cellular Biology* **15**, 1968-1973.

- Chow, C.M., Neto, H., Foucart, C., and Moore, I.** (2008). Rab-A2 and Rab-A3 GTPases define a trans-Golgi endosomal membrane domain in *Arabidopsis* that contributes substantially to the cell plate. *Plant Cell* **20**, 101-123.
- Chuang, C.F., and Meyerowitz, E.M.** (2000). Specific and heritable genetic interference by double-stranded RNA in *Arabidopsis thaliana*. *PNAS* **97**, 4985-4990.
- Collonnier, C., Guyon-Debast, A., Maclot, F., Mara, K., Chariot, F., and Nogue, F.** (2017a). Towards mastering CRISPR-induced gene knock-in in plants: Survey of key features and focus on the model *Physcomitrella patens*. *Methods* **121**, 103-117.
- Collonnier, C., Epert, A., Mara, K., Maclot, F., Guyon-Debast, A., Charlot, F., White, C., Schaefer, D.G., and Nogue, F.** (2017b). CRISPR-Cas9-mediated efficient directed mutagenesis and RAD51-dependent and RAD51-independent gene targeting in the moss *Physcomitrella patens*. *Plant Biotechnol. J.* **15**, 122-131.
- Dang, Y., Jia, G.X., Choi, J., Ma, H.M., Anaya, E., Ye, C.T., Shankar, P., and Wu, H.Q.** (2015). Optimizing sgRNA structure to improve CRISPR-Cas9 knockout efficiency. *Genome Biol.* **16**.
- Deans, R.M., Morgens, D.W., Okesli, A., Pillay, S., Horlbeck, M.A., Kampmann, M., Gilbert, L.A., Li, A., Mateo, R., Smith, M., Glenn, J.S., Carette, J.E., Khosla, C., and Bassik, M.C.** (2016). Parallel shRNA and CRISPR-Cas9 screens enable antiviral drug target identification. *Nat Chem Biol* **12**, 361-366.
- Deeks, M.J., Fendrych, M., Smertenko, A., Bell, K.S., Oparka, K., Cvrckova, F., Zarsky, V., and Hussey, P.J.** (2010). The plant formin AtFH4 interacts with both actin and microtubules, and contains a newly identified microtubule-binding domain. *J. Cell Sci.* **123**, 1209-1215.
- Delaux, P.M., Hetherington, A.J., Coudert, Y., Delwiche, C., Dunand, C., Gould, S., Kenrick, P., Li, F.W., Philippe, H., Rensing, S.A., Rich, M., Strullu-Derrien, C., and de Vries, J.** (2019). Reconstructing trait evolution in plant evo-devo studies. *Curr. Biol.* **29**, R1110-R1118.
- Demirer, G.S., Zhang, H., Goh, N.S., Pinals, R.L., Chang, R., and Landry, M.P.** (2020). Carbon nanocarriers deliver siRNA to intact plant cells for efficient gene knockdown. *Sci Adv* **6**, eaaz0495.
- Denninger, P., Reichelt, A., Schmidt, V.A.F., Mehlhorn, D.G., Asseck, L.Y., Stanley, C.E., Keinath, N.F., Evers, J.F., Grefen, C., and Grossmann, G.** (2019). Distinct RopGEFs Successively Drive Polarization and Outgrowth of Root Hairs. *Curr. Biol.* **29**, 1854-+.
- Diekmann, Y., Seixas, E., Gouw, M., Tavares-Cadete, F., Seabra, M.C., and Pereira-Leal, J.B.** (2011). Thousands of rab GTPases for the cell biologist. *PLoS Comput Biol* **7**, e1002217.
- Ding, X.X., Pervere, L.M., Bascom, C., Bibeau, J.P., Khurana, S., Butt, A.M., Orr, R.G., Flaherty, P.J., Bezanilla, M., and Vidali, L.** (2018). Conditional genetic screen in *Physcomitrella patens* reveals a novel microtubule depolymerizing-end-tracking protein. *Plos Genet* **14**.
- Dix, J.A., and Verkman, A.S.** (2008). Crowding effects on diffusion in solutions and cells. *Annu Rev Biophys* **37**, 247-263.
- Doetschman, T., Gregg, R.G., Maeda, N., Hooper, M.L., Melton, D.W., Thompson, S., and Smithies, O.** (1987). Targeted correction of a mutant HPRT gene in mouse embryonic stem cells. *Nature* **330**, 576-578.
- Donovan, K.W., and Bretscher, A.** (2012). Myosin-V Is Activated by Binding Secretory Cargo and Released in Coordination with Rab/Exocyst Function. *Developmental Cell* **23**, 769-781.
- Doudna, J.A., and Charpentier, E.** (2014). The new frontier of genome engineering with CRISPR-Cas9. *Science* **346**, 1077-+.
- Ebine, K., and Ueda, T.** (2015). Roles of membrane trafficking in plant cell wall dynamics. *Front Plant Sci* **6**, 878.
- Edgar, R.C.** (2004). MUSCLE: multiple sequence alignment with high accuracy and high throughput. *Nucleic Acids Res.* **32**, 1792-1797.
- Elliott, L., Moore, I., and Kirchhelle, C.** (2020). Spatio-temporal control of post-Golgi exocytic trafficking in plants. *J. Cell Sci.* **133**.

- Feiguelman, G., Fu, Y., and Yalovsky, S.** (2018). ROP GTPases Structure-Function and Signaling Pathways. *Plant Physiol.* **176**, 57-79.
- Fendrych, M., Synek, L., Pečenková, T., Toupalová, H., Cole, R., Drdová, E., Nebesářová, J., Šedinová, M., Hála, M., and Fowler, J.E.** (2010). The Arabidopsis exocyst complex is involved in cytokinesis and cell plate maturation. *The Plant Cell* **22**, 3053-3065.
- Field, K.J., Pressel, S., Duckett, J.G., Rimington, W.R., and Bidartondo, M.I.** (2015). Symbiotic options for the conquest of land. *Trends Ecol. Evol.* **30**, 477-486.
- Fire, A., Xu, S., Montgomery, M.K., Kostas, S.A., Driver, S.E., and Mello, C.C.** (1998). Potent and specific genetic interference by double-stranded RNA in *Caenorhabditis elegans*. *Nature* **391**, 806-811.
- Furt, F., Liu, Y.C., Bibeau, J.P., Tuzel, E., and Vidali, L.** (2013). Apical myosin XI anticipates F-actin during polarized growth of *Physcomitrella patens* cells. *Plant J.* **73**, 417-428.
- Fusaro, A.F., Matthew, L., Smith, N.A., Curtin, S.J., Dedic-Hagan, J., Ellacott, G.A., Watson, J.M., Wang, M.B., Brosnan, C., Carroll, B.J., and Waterhouse, P.M.** (2006). RNA interference-inducing hairpin RNAs in plants act through the viral defence pathway. *EMBO Rep* **7**, 1168-1175.
- Galotto, G., Bibeau, J.P., and Vidali, L.** (2019). Automated image acquisition and morphological analysis of cell growth mutants in *Physcomitrella patens*. *Methods Mol Biol* **1992**, 307-322.
- Galotto, G., Abreu, I., Sherman, C., Liu, B., Gonzalez-Guerrero, M., and Vidali, L.** (2020). Chitin triggers calcium-mediated immune response in the plant model *Physcomitrella patens*. *Mol Plant Microbe Interact*, MPMI03200064R.
- Gaudelli, N.M., Komor, A.C., Rees, H.A., Packer, M.S., Badran, A.H., Bryson, D.I., and Liu, D.R.** (2017). Programmable base editing of A.T to G.C in genomic DNA without DNA cleavage. *Nature* **551**, 464-+.
- Gilbert, L.A., Larson, M.H., Morsut, L., Liu, Z.R., Brar, G.A., Torres, S.E., Stern-Ginossar, N., Brandman, O., Whitehead, E.H., Doudna, J.A., Lim, W.A., Weissman, J.S., and Qi, L.S.** (2013). CRISPR-Mediated Modular RNA-Guided Regulation of Transcription in Eukaryotes. *Cell* **154**, 442-451.
- Goldenring, J.R., Roland, J.T., and Lapierre, L.A.** (2012). Rablla, Rab8a and Myosin V: Regulators of Recycling and Beyond. *Rab GTPases and membrane trafficking*, 123.
- Goodsell, D.S., Olson, A.J., and Forli, S.** (2020). Art and Science of the Cellular Mesoscale. *Trends Biochem. Sci.* **45**, 472-483.
- Grefen, C., and Blatt, M.R.** (2012). A 2in1 cloning system enables ratiometric bimolecular fluorescence complementation (rBiFC). *BioTechniques* **53**, 311-314.
- Guindon, S., Lethiec, F., Duroux, P., and Gascuel, O.** (2005). PHYML Online--a web server for fast maximum likelihood-based phylogenetic inference. *Nucleic Acids Res.* **33**, W557-559.
- Guindon, S., Dufayard, J.F., Lefort, V., Anisimova, M., Hordijk, W., and Gascuel, O.** (2010). New algorithms and methods to estimate maximum-likelihood phylogenies: assessing the performance of PhyML 3.0. *Syst. Biol.* **59**, 307-321.
- Guo, H.S., Fei, J.F., Xie, Q., and Chua, N.H.** (2003). A chemical-regulated inducible RNAi system in plants. *Plant J.* **34**, 383-392.
- Guo, X.Y., Li, Y., Fan, J., Xiong, H., Xu, F.X., Shi, J., Shi, Y., Zhao, J.Q., Wang, Y.F., Cao, X.L., and Wang, W.M.** (2019). Host-induced gene silencing of MoAP1 confers broad-spectrum resistance to *Magnaporthe oryzae*. *Front Plant Sci* **10**.
- Gutierrez-Nava, M.D., Aukerman, M.J., Sakai, H., Tingey, S.V., and Williams, R.W.** (2008). Artificial trans-acting siRNAs confer consistent and effective gene silencing. *Plant Physiol* **147**, 543-551.
- Haeussler, M., Schonig, K., Eckert, H., Eschstruth, A., Mianne, J., Renaud, J.B., Schneider-Maunoury, S., Shkumatava, A., Teboul, L., Kent, J., Joly, J.S., and Concordet, J.P.** (2016). Evaluation of off-target and on-target scoring algorithms and integration into the guide RNA selection tool CRISPOR. *Genome Biol* **17**, 148.

- Halfter, U., Morris, P.C., and Willmitzer, L.** (1992). Gene targeting in *Arabidopsis thaliana*. *Mol. Gen. Genet.* **231**, 186-193.
- Hammer, J.A., and Sellers, J.R.** (2012). Walking to work: roles for class V myosins as cargo transporters. *Nature Reviews Molecular Cell Biology* **13**, 13-26.
- Hanna, R.E., and Doench, J.G.** (2020). Design and analysis of CRISPR-Cas experiments. *Nat. Biotechnol.*
- Hannon, G.J.** (2002). RNA interference. *Nature* **418**, 244-251.
- Hauser, F., Chen, W., Deinlein, U., Chang, K., Ossowski, S., Fitz, J., Hannon, G.J., and Schroeder, J.I.** (2013). A genomic-scale artificial microRNA library as a tool to investigate the functionally redundant gene space in *Arabidopsis*. *Plant Cell* **25**, 2848-2863.
- Havelkova, L., Nanda, G., Martinek, J., Bellinvia, E., Sikorova, L., Slajcherova, K., Seifertova, D., Fischer, L., Fiserova, J., Petrasek, J., and Schwarzerova, K.** (2015). Arp2/3 complex subunit ARPC2 binds to microtubules. *Plant Sci.* **241**, 96-108.
- Heider, M.R., and Munson, M.** (2012). Exorcising the exocyst complex. *Traffic* **13**, 898-907.
- Hepler, P.K., and Winship, L.J.** (2015). The pollen tube clear zone: Clues to the mechanism of polarized growth. *Journal of Integrative Plant Biology* **57**, 79-92.
- Hepler, P.K., Vidali, L., and Cheung, A.Y.** (2001). Polarized cell growth in higher plants. *Annu Rev Cell Dev Biol* **17**, 159-187.
- Hernandez-Gonzalez, M., Bravo-Plaza, I., Pinar, M., de los Rios, V., Arst, H.N., and Penalva, M.A.** (2018). Endocytic recycling via the TGN underlies the polarized hyphal mode of life. *PLoS Genet.* **14**.
- Himber, C., Dunoyer, P., Moissiard, G., Ritzenthaler, C., and Voinnet, O.** (2003). Transitivity-dependent and -independent cell-to-cell movement of RNA silencing. *EMBO J.* **22**, 4523-4533.
- Honkanen, S., Jones, V.A.S., Morieri, G., Champion, C., Hetherington, A.J., Kelly, S., Proust, H., Saint-Marcoux, D., Prescott, H., and Dolan, L.** (2016). The Mechanism Forming the Cell Surface of Tip-Growing Rooting Cells Is Conserved among Land Plants. *Curr. Biol.* **26**, 3238-3244.
- Horlbeck, M.A., Witkowsky, L.B., Guglielmi, B., Replogle, J.M., Gilbert, L.A., Villalta, J.E., Torigoe, S.E., Tjian, R., and Weissman, J.S.** (2016). Nucleosomes impede Cas9 access to DNA in vivo and in vitro. *Elife* **5**.
- Housden, B.E., Muhar, M., Gemberling, M., Gersbach, C.A., Stainier, D.Y., Seydoux, G., Mohr, S.E., Zuber, J., and Perrimon, N.** (2017). Loss-of-function genetic tools for animal models: cross-species and cross-platform differences. *Nat Rev Genet* **18**, 24-40.
- Hyman, A.A., Weber, C.A., and Julicher, F.** (2014). Liquid-liquid phase separation in biology. *Annu Rev Cell Dev Biol* **30**, 39-58.
- Ishizaki, K., Nishihama, R., Yamato, K.T., and Kohchi, T.** (2016). Molecular Genetic Tools and Techniques for *Marchantia polymorpha* Research. *Plant Cell Physiol.* **57**, 262-270.
- Jean, S., and Kiger, A.A.** (2012). Coordination between RAB GTPase and phosphoinositide regulation and functions. *Nat Rev Mol Cell Bio* **13**, 463-470.
- Jensen, K.T., Floe, L., Petersen, T.S., Huang, J., Xu, F., Bolund, L., Luo, Y., and Lin, L.** (2017). Chromatin accessibility and guide sequence secondary structure affect CRISPR-Cas9 gene editing efficiency. *FEBS Lett* **591**, 1892-1901.
- Jin, Y., Sultana, A., Gandhi, P., Franklin, E., Hamamoto, S., Khan, A.R., Munson, M., Schekman, R., and Weisman, L.S.** (2011). Myosin V transports secretory vesicles via a Rab GTPase cascade and interaction with the exocyst complex. *Dev Cell* **21**, 1156-1170.
- Jinek, M., Chylinski, K., Fonfara, I., Hauer, M., Doudna, J.A., and Charpentier, E.** (2012). A Programmable Dual-RNA-Guided DNA Endonuclease in Adaptive Bacterial Immunity. *Science* **337**, 816-821.
- Kalde, M., Elliott, L., Ravikumar, R., Rybak, K., Altmann, M., Klaeger, S., Wiese, C., Abele, M., Al, B., Kalbfuss, N., Qi, X.Y., Steiner, A., Meng, C., Zheng, H.Q., Kuster, B., Falter-Braun, P., Ludwig, C., Moore, I., and Assaad, F.F.** (2019). Interactions between Transport Protein Particle (TRAPP) complexes and Rab GTPases in *Arabidopsis*. *Plant J* **100**, 279-297.

- Kamisugi, Y., Cuming, A.C., and Cove, D.J.** (2005). Parameters determining the efficiency of gene targeting in the moss *Physcomitrella patens*. *Nucleic Acids Res.* **33**.
- Kamthan, A., Chaudhuri, A., Kamthan, M., and Datta, A.** (2015). Small RNAs in plants: recent development and application for crop improvement. *Front Plant Sci* **6**, 208.
- Kang, B.C., Yun, J.Y., Kim, S.T., Shin, Y., Ryu, J., Choi, M., Woo, J.W., and Kim, J.S.** (2018). Precision genome engineering through adenine base editing in plants. *Nat Plants* **4**, 427-431.
- Kang, E., Zheng, M., Zhang, Y., Yuan, M., Yalovsky, S., Zhu, L., and Fu, Y.** (2017). The Microtubule-Associated Protein MAP18 Affects ROP2 GTPase Activity during Root Hair Growth. *Plant Physiol.* **174**, 202-222.
- Kempin, S.A., Liljegren, S.J., Block, L.M., Rounsley, S.D., Yanofsky, M.F., and Lam, E.** (1997). Targeted disruption in *Arabidopsis*. *Nature* **389**, 802-803.
- Khan, A.R., and Menetrey, J.** (2013). Structural biology of Arf and Rab GTPases' effector recruitment and specificity. *Structure* **21**, 1284-1297.
- Khraiwesh, B., Ossowski, S., Weigel, D., Reski, R., and Frank, W.** (2008). Specific gene silencing by artificial MicroRNAs in *Physcomitrella patens*: an alternative to targeted gene knockouts. *Plant Physiol* **148**, 684-693.
- Khraiwesh, B., Arif, M.A., Seumel, G.I., Ossowski, S., Weigel, D., Reski, R., and Frank, W.** (2010). Transcriptional control of gene expression by microRNAs. *Cell* **140**, 111-122.
- Kim, D.I., and Roux, K.J.** (2016). Filling the Void: Proximity-Based Labeling of Proteins in Living Cells. *Trends Cell Biol.* **26**, 804-817.
- Knodler, A., Feng, S., Zhang, J., Zhang, X., Das, A., Peranen, J., and Guo, W.** (2010). Coordination of Rab8 and Rab11 in primary ciliogenesis. *Proc Natl Acad Sci U S A* **107**, 6346-6351.
- Komor, A.C., Kim, Y.B., Packer, M.S., Zuris, J.A., and Liu, D.R.** (2016). Programmable editing of a target base in genomic DNA without double-stranded DNA cleavage. *Nature* **533**, 420-+.
- Kosicki, M., Tomberg, K., and Bradley, A.** (2018). Repair of double-strand breaks induced by CRISPR-Cas9 leads to large deletions and complex rearrangements. *Nat. Biotechnol.* **36**, 765-+.
- Kozgunova, E., and Goshima, G.** (2019). A versatile microfluidic device for highly inclined thin illumination microscopy in the moss *Physcomitrella patens*. *Sci. Rep.* **9**.
- Kudla, J., and Bock, R.** (2016). Lighting the Way to Protein-Protein Interactions: Recommendations on Best Practices for Bimolecular Fluorescence Complementation Analyses. *Plant Cell* **28**, 1002-1008.
- Kurth, E.G., Peremyslov, V.V., Turner, H.L., Makarova, K.S., Iranzo, J., Mekhedov, S.L., Koonin, E.V., and Dolja, V.V.** (2017). Myosin-driven transport network in plants. *Proceedings of the National Academy of Sciences of the United States of America* **114**, E1385-E1394.
- Lan, Y.X., Liu, X.N., Fu, Y., and Huang, S.J.** (2018). Arabidopsis class I formins control membrane-originated actin polymerization at pollen tube tips. *PLoS Genet.* **14**.
- Lang, D., Ullrich, K.K., Murat, F., Fuchs, J., Jenkins, J., Haas, F.B., Piednoel, M., Gundlach, H., Van Bel, M., Meyberg, R., Vives, C., Morata, J., Symeonidi, A., Hiss, M., Muchero, W., Kamisugi, Y., Saleh, O., Blanc, G., Decker, E.L., van Gessel, N., Grimwood, J., Hayes, R.D., Graham, S.W., Gunter, L.E., McDaniel, S.F., Hoernstein, S.N.W., Larsson, A., Li, F.W., Perroud, P.F., Phillips, J., Ranjan, P., Rokshar, D.S., Rothfels, C.J., Schneider, L., Shu, S., Stevenson, D.W., Thummler, F., Tillich, M., Villarreal Aguilar, J.C., Widiez, T., Wong, G.K., Wymore, A., Zhang, Y., Zimmer, A.D., Quatrano, R.S., Mayer, K.F.X., Goodstein, D., Casacuberta, J.M., Vandepoele, K., Reski, R., Cuming, A.C., Tuskan, G.A., Maumus, F., Salse, J., Schmutz, J., and Rensing, S.A.** (2018). The *Physcomitrella patens* chromosome-scale assembly reveals moss genome structure and evolution. *Plant J.* **93**, 515-533.
- Le Bail, A., Schulmeister, S., Perroud, P.F., Ntefidou, M., Rensing, S.A., and Kost, B.** (2019). Analysis of the Localization of Fluorescent PpROP1 and PpROP-GEF4 Fusion Proteins in Moss Protonemata Based on Genomic "Knock-In" and Estradiol-Titratable Expression. *Front Plant Sci* **10**.

- Lee, H., and Kim, J.S.** (2018). Unexpected CRISPR on-target effects. *Nat. Biotechnol.* **36**, 703-+.
- Lee, K.Y., Lund, P., Lowe, K., and Dunsmuir, P.** (1990). Homologous recombination in plant cells after *Agrobacterium*-mediated transformation. *Plant Cell* **2**, 415-425.
- Lenton, T.M., Dahl, T.W., Daines, S.J., Mills, B.J., Ozaki, K., Saltzman, M.R., and Porada, P.** (2016). Earliest land plants created modern levels of atmospheric oxygen. *Proc. Natl. Acad. Sci. U. S. A.* **113**, 9704-9709.
- Lepore, D.M., Martinez-Nunez, L., and Munson, M.** (2018). Exposing the Elusive Exocyst Structure. *Trends Biochem. Sci.* **43**, 714-725.
- Levine, R.A., and Taylor, M.W.** (1982). Mechanism of adenine toxicity in *Escherichia coli*. *Journal of Bacteriology* **149**, 923-930.
- Li, H., Luo, N., Wang, W.D., Liu, Z.Y., Chen, J.S., Zhao, L.T., Tan, L., Wang, C.Y., Qin, Y., Li, C., Xu, T.D., and Yang, Z.B.** (2018). The REN4 rheostat dynamically coordinates the apical and lateral domains of *Arabidopsis* pollen tubes. *Nat Commun* **9**.
- Li, J.-F., and Nebenführ, A.** (2007). Organelle targeting of myosin XI is mediated by two globular tail subdomains with separate cargo binding sites. *Journal of Biological Chemistry* **282**, 20593-20602.
- Li, J.F., Chung, H.S., Niu, Y.J., Bush, J., McCormack, M., and Sheen, J.** (2013). Comprehensive protein-based artificial microRNA screens for effective gene silencing in plants. *Plant Cell* **25**, 1507-1522.
- Li, S.W., Dong, H.J., Pei, W.K., Liu, C.N., Zhang, S., Sun, T.T., Xue, X.H., and Ren, H.Y.** (2017). LIFH1-mediated interaction between actin fringe and exocytic vesicles is involved in pollen tube tip growth. *New Phytol.* **214**, 745-761.
- Li, Y.H., Shen, Y.A., Cai, C., Zhong, C.C., Zhu, L., Yuan, M., and Ren, H.Y.** (2010). The Type II *Arabidopsis* Formin14 Interacts with Microtubules and Microfilaments to Regulate Cell Division. *Plant Cell* **22**, 2710-2726.
- Liang, Y., Toth, K., Cao, Y.R., Tanaka, K., Espinoza, C., and Stacey, G.** (2014). Lipochitooligosaccharide recognition: an ancient story. *New Phytol* **204**, 289-296.
- Lipatova, Z., Tokarev, A.A., Jin, Y., Mulholland, J., Weisman, L.S., and Segev, N.** (2008). Direct interaction between a myosin V motor and the Rab GTPases Ypt31/32 is required for polarized secretion. *Molecular biology of the cell* **19**, 4177-4187.
- Liu, S.M., and Yoder, J.I.** (2016). Chemical induction of hairpin RNAi molecules to silence vital genes in plant roots. *Sci Rep-Uk* **6**.
- Liu, Y., Budke, J.M., and Goffinet, B.** (2012). Phylogenetic inference rejects sporophyte based classification of the Funariaceae (Bryophyta): rapid radiation suggests rampant homoplasy in sporophyte evolution. *Mol. Phylogenet. Evol.* **62**, 130-145.
- Liu, Y.C., and Vidali, L.** (2011). Efficient polyethylene glycol (PEG) mediated transformation of the moss *Physcomitrella patens*. *Jove-J Vis Exp*.
- Lopez-Obando, M., Hoffmann, B., Gery, C., Guyon-Debast, A., Teoule, E., Rameau, C., Bonhomme, S., and Nogue, F.** (2016). Simple and Efficient Targeting of Multiple Genes Through CRISPR-Cas9 in *Physcomitrella patens*. *G3-Genes Genom Genet* **6**, 3647-3653.
- Luo, N., Yan, A., and Yang, Z.B.** (2016). Measuring Exocytosis Rate Using Corrected Fluorescence Recovery After Photoconversion. *Traffic* **17**, 554-564.
- MacVeigh-Fierro, D., Tüzel, E., and Vidali, L.** (2017). The Motor Kinesin 4II is important for growth and chloroplast light avoidance in the moss *Physcomitrella patens*. *American Journal of Plant Sciences* **8**, 791.
- Madison, S.L., and Nebenfuhr, A.** (2013). Understanding myosin functions in plants: are we there yet? *Curr Opin Plant Biol* **16**, 710-717.
- Mallett, D.R., Chang, M.Q., Cheng, X.H., and Bezanilla, M.** (2019). Efficient and modular CRISPR-Cas9 vector system for *Physcomitrella patens*. *Plant Direct* **3**.

- Mara, K., Charlot, F., Guyon-Debast, A., Schaefer, D.G., Collonnier, C., Grelon, M., and Nogue, F.** (2019). POLQ plays a key role in the repair of CRISPR/Cas9-induced double-stranded breaks in the moss *Physcomitrella patens*. *New Phytol.* **222**, 1380-1391.
- Margis, R., Fusaro, A.F., Smith, N.A., Curtin, S.J., Watson, J.M., Finnegan, E.J., and Waterhouse, P.M.** (2006). The evolution and diversification of Dicers in plants. *FEBS Lett.* **580**, 2442-2450.
- Martzoukou, O., Amillis, S., Zervakou, A., Christoforidis, S., and Diallinas, G.** (2017). The AP-2 complex has a specialized clathrin-independent role in apical endocytosis and polar growth in fungi. *Elife* **6**.
- Mayers, J.R., Hu, T.W., Wang, C., Cardenas, J.J., Tan, Y.Q., Pan, J.W., and Bednarek, S.Y.** (2017a). SCD1 and SCD2 Form a Complex That Functions with the Exocyst and RabE1 in Exocytosis and Cytokinesis. *Plant Cell* **29**, 2610-2625.
- Mayers, J.R., Hu, T., Wang, C., Cardenas, J.J., Tan, Y., Pan, J., and Bednarek, S.Y.** (2017b). SCD1 and SCD2 Form a Complex That Functions with the Exocyst and RabE1 in Exocytosis and Cytokinesis. *Plant Cell* **29**, 2610-2625.
- McKenna, S.T., Kunkel, J.G., Bosch, M., Rounds, C.M., Vidali, L., Winship, L.J., and Hepler, P.K.** (2009). Exocytosis precedes and predicts the increase in growth in oscillating pollen tubes. *The Plant Cell* **21**, 3026-3040.
- Medina, R., Johnson, M.G., Liu, Y., Wickett, N.J., Shaw, A.J., and Goffinet, B.** (2019). Phylogenomic delineation of *Physcomitrium* (Bryophyta: Funariaceae) based on targeted sequencing of nuclear exons and their flanking regions rejects the retention of *Physcomitrella*, *Physcomitridium* and *Aphanorrhagma*. *J Syst Evol* **57**, 404-417.
- Medina, R., Johnson, M., Liu, Y., Wilding, N., Hedderson, T.A., Wickett, N., and Goffinet, B.** (2018). Evolutionary dynamism in bryophytes: Phylogenomic inferences confirm rapid radiation in the moss family Funariaceae. *Molecular Phylogenetics and Evolution* **120**, 240-247.
- Miki, T., Nishina, M., and Goshima, G.** (2015). RNAi screening identifies the armadillo repeat-containing kinesins responsible for microtubule-dependent nuclear positioning in *Physcomitrella patens*. *Plant Cell Physiol* **56**, 737-749.
- Mizuno-Yamasaki, E., Rivera-Molina, F., and Novick, P.** (2012). GTPase networks in membrane traffic. *Annu. Rev. Biochem.* **81**, 637-659.
- Moen, E., Bannon, D., Kudo, T., Graf, W., Covert, M., and Van Valen, D.** (2019). Deep learning for cellular image analysis. *Nat Methods* **16**, 1233-1246.
- Moffatt, B., and Somerville, C.** (1988). Positive selection for male-sterile mutants of *Arabidopsis* lacking adenine phosphoribosyl transferase activity. *Plant Physiol* **86**, 1150-1154.
- Moissiard, G., Parizotto, E.A., Himber, C., and Voinnet, O.** (2007). Transitivity in *Arabidopsis* can be primed, requires the redundant action of the antiviral Dicer-like 4 and Dicer-like 2, and is compromised by viral-encoded suppressor proteins. *RNA* **13**, 1268-1278.
- Morel, J.B., Mourrain, P., Beclin, C., and Vaucheret, H.** (2000). DNA methylation and chromatin structure affect transcriptional and post-transcriptional transgene silencing in *Arabidopsis*. *Curr Biol* **10**, 1591-1594.
- Moscatelli, A., Idilli, A., Rodighiero, S., and Caccianiga, M.** (2012). Inhibition of actin polymerisation by low concentration Latrunculin B affects endocytosis and alters exocytosis in shank and tip of tobacco pollen tubes. *Plant biology* **14**, 770-782.
- Nakai, J., Ohkura, M., and Imoto, K.** (2001). A high signal-to-noise Ca<sup>2+</sup> probe composed of a single green fluorescent protein. *Nat Biotechnol* **19**, 137-141.
- Nakaoka, Y., Miki, T., Fujioka, R., Uehara, R., Tomioka, A., Obuse, C., Kubo, M., Hiwatashi, Y., and Goshima, G.** (2012). An inducible RNA interference system in *Physcomitrella patens* reveals a dominant role of augmin in phragmoplast microtubule generation. *Plant Cell* **24**, 1478-1493.

- Napoli, C., Lemieux, C., and Jorgensen, R.** (1990). Introduction of a chimeric chalcone synthase gene into petunia results in reversible co-suppression of homologous genes in trans. *Plant Cell* **2**, 279-289.
- Nishida, K., Arazoe, T., Yachie, N., Banno, S., Kakimoto, M., Tabata, M., Mochizuki, M., Miyabe, A., Araki, M., Hara, K.Y., Shimatani, Z., and Kondo, A.** (2016). Targeted nucleotide editing using hybrid prokaryotic and vertebrate adaptive immune systems. *Science* **353**.
- Offringa, R., Degroot, M.J.A., Haagsman, H.J., Does, M.P., Vandanelzen, P.J.M., and Hooykaas, P.J.J.** (1990). Extrachromosomal Homologous Recombination and Gene Targeting in Plant Cells after *Agrobacterium*-Mediated Transformation. *EMBO J.* **9**, 3077-3084.
- Ojangu, E.L., Jarve, K., Paves, H., and Truve, E.** (2007). Arabidopsis thaliana myosin XIX is involved in root hair as well as trichome morphogenesis on stems and leaves. *Protoplasma* **230**, 193-202.
- Oliver, J.P., Castro, A., Gaggero, C., Cascon, T., Schmelz, E.A., Castresana, C., and de Leon, I.P.** (2009). *Pythium* infection activates conserved plant defense responses in mosses. *Planta* **230**, 569-579.
- Orr, R.G., Cheng, X., Vidali, L., and Bezanilla, M.** (2020a). Orchestrating cell morphology from the inside out - using polarized cell expansion in plants as a model. *Curr. Opin. Cell Biol.* **62**, 46-53.
- Orr, R.G., Foley, S.J., Galotto, G., Liu, B., and Vidali, L.** (2020b). Robust survival-based RNAi using in tandem silencing of adenine phosphoribosyltransferase. *bioRxiv*, 2020.2004.2009.034132.
- Otani, K., Ishizaki, K., Nishihama, R., Takatani, S., Kohchi, T., Takahashi, T., and Motose, H.** (2018). An evolutionarily conserved NIMA-related kinase directs rhizoid tip growth in the basal land plant *Marchantia polymorpha*. *Development* **145**.
- Ovecka, M., Lang, I., Baluska, F., Ismail, A., Illes, P., and Lichtscheidl, I.K.** (2005). Endocytosis and vesicle trafficking during tip growth of root hairs. *Protoplasma* **226**, 39-54.
- Palauqui, J.C., Elmayan, T., Pollien, J.M., and Vaucheret, H.** (1997). Systemic acquired silencing: transgene-specific post-transcriptional silencing is transmitted by grafting from silenced stocks to non-silenced scions. *EMBO J.* **16**, 4738-4745.
- Park, E., and Nebenführ, A.** (2013). Myosin XIX of Arabidopsis thaliana accumulates at the root hair tip and is required for fast root hair growth. *PloS one* **8**, e76745.
- Pashkova, N., Jin, Y., Ramaswamy, S., and Weisman, L.S.** (2006). Structural basis for myosin V discrimination between distinct cargoes. *The EMBO Journal* **25**, 693-700.
- Paterson, A.H., Wendel, J.F., Gundlach, H., Guo, H., Jenkins, J., Jin, D., Llewellyn, D., Showmaker, K.C., Shu, S., Udall, J., Yoo, M.J., Byers, R., Chen, W., Doron-Faigenboim, A., Duke, M.V., Gong, L., Grimwood, J., Grover, C., Grupp, K., Hu, G., Lee, T.H., Li, J., Lin, L., Liu, T., Marler, B.S., Page, J.T., Roberts, A.W., Romanel, E., Sanders, W.S., Szadkowski, E., Tan, X., Tang, H., Xu, C., Wang, J., Wang, Z., Zhang, D., Zhang, L., Ashrafi, H., Bedon, F., Bowers, J.E., Brubaker, C.L., Chee, P.W., Das, S., Gingle, A.R., Haigler, C.H., Harker, D., Hoffmann, L.V., Hovav, R., Jones, D.C., Lemke, C., Mansoor, S., ur Rahman, M., Rainville, L.N., Rambani, A., Reddy, U.K., Rong, J.K., Saranga, Y., Scheffler, B.E., Scheffler, J.A., Stelly, D.M., Triplett, B.A., Van Deynze, A., Vaslin, M.F., Waghmare, V.N., Walford, S.A., Wright, R.J., Zaki, E.A., Zhang, T., Dennis, E.S., Mayer, K.F., Peterson, D.G., Rokhsar, D.S., Wang, X., and Schmutz, J.** (2012). Repeated polyploidization of *Gossypium* genomes and the evolution of spinnable cotton fibres. *Nature* **492**, 423-427.
- Pereira-Leal, J.B., and Seabra, M.C.** (2000). The mammalian Rab family of small GTPases: definition of family and subfamily sequence motifs suggests a mechanism for functional specificity in the Ras superfamily. *J. Mol. Biol.* **301**, 1077-1087.
- Pereira-Leal, J.B., and Seabra, M.C.** (2001). Evolution of the Rab family of small GTP-binding proteins. *J. Mol. Biol.* **313**, 889-901.
- Peremyslov, V.V., Prokhnevsky, A.I., Avisar, D., and Dolja, V.V.** (2008). Two class XI myosins function in organelle trafficking and root hair development in Arabidopsis. *Plant Physiology* **146**, 1109-1116.
- Peremyslov, V.V., Klocko, A.L., Fowler, J.E., and Dolja, V.V.** (2012). Arabidopsis myosin XI-K localizes to the motile endomembrane vesicles associated with F-actin. *Frontiers in plant science* **3**, 184.

- Peremyslov, V.V., Cole, R.A., Fowler, J.E., and Dolja, V.V.** (2015). Myosin-powered membrane compartment drives cytoplasmic streaming, cell expansion and plant development. *PLoS one* **10**, e0139331.
- Peremyslov, V.V., Morgun, E.A., Kurth, E.G., Makarova, K.S., Koonin, E.V., and Dolja, V.V.** (2013). Identification of myosin XI receptors in *Arabidopsis* defines a distinct class of transport vesicles. *The Plant Cell* **25**, 3022-3038.
- Pettersen, E.F., Goddard, T.D., Huang, C.C., Couch, G.S., Greenblatt, D.M., Meng, E.C., and Ferrin, T.E.** (2004). UCSF Chimera—a visualization system for exploratory research and analysis. *Journal of computational chemistry* **25**, 1605-1612.
- Pfeffer, S.R.** (2013). Rab GTPase regulation of membrane identity. *Curr. Opin. Cell Biol.* **25**, 414-419.
- Pfeffer, S.R.** (2017). Rab GTPases: master regulators that establish the secretory and endocytic pathways. *Mol Biol Cell* **28**, 712-715.
- Platre, M.P., Bayle, V., Armengot, L., Bareille, J., Marques-Bueno, M.D., Creff, A., Maneta-Peyret, L., Fiche, J.B., Nollmann, M., Miege, C., Moreau, P., Martiniere, A., and Jaillais, Y.** (2019). Developmental control of plant Rho GTPase nano-organization by the lipid phosphatidylserine. *Science* **364**, 57-+.
- Pollard, T.D.** (2010). A guide to simple and informative binding assays. *Mol Biol Cell* **21**, 4061-4067.
- Prigge, M.J., Lavy, M., Ashton, N.W., and Estelle, M.** (2010). *Physcomitrella patens* auxin-resistant mutants affect conserved elements of an auxin-signaling pathway. *Curr Biol* **20**, 1907-1912.
- Puchta, H., and Fauser, F.** (2013). Gene targeting in plants: 25 years later. *Int. J. Dev. Biol.* **57**, 629-637.
- Puchta, H., Dujon, B., and Hohn, B.** (1993). Homologous Recombination in Plant-Cells Is Enhanced by in-Vivo Induction of Double-Strand Breaks into DNA by a Site-Specific Endonuclease. *Nucleic Acids Res.* **21**, 5034-5040.
- Puttick, M.N., Morris, J.L., Williams, T.A., Cox, C.J., Edwards, D., Kenrick, P., Pressel, S., Wellman, C.H., Schneider, H., Pisani, D., and Donoghue, P.C.J.** (2018). The Interrelationships of Land Plants and the Nature of the Ancestral Embryophyte. *Curr. Biol.* **28**, 733-+.
- Pylypenko, O., Hammich, H., Yu, I.-M., and Houdusse, A.** (2018). Rab GTPases and their interacting protein partners: Structural insights into Rab functional diversity. *Small GTPases* **9**, 22-48.
- Pylypenko, O., Welz, T., Tittel, J., Kollmar, M., Chardon, F., Malherbe, G., Weiss, S., Michel, C.I.L., Samol-Wolf, A., Grasskamp, A.T., Hume, A., Goud, B., Baron, B., England, P., Titus, M.A., Schwillie, P., Weidemann, T., Houdusse, A., and Kerkhoff, E.** (2016). Coordinated recruitment of Spir actin nucleators and myosin V motors to Rab11 vesicle membranes. *Elife* **5**.
- Qin, L., Li, J.Y., Wang, Q.Q., Xu, Z.P., Sun, L., Alariqi, M., Manghwar, H., Wang, G.Y., Li, B., Ding, X., Rui, H.P., Huang, H.M., Lu, T.L., Lindsey, K., Daniell, H., Zhang, X.L., and Jin, S.X.** (2020). High-efficient and precise base editing of C center dot G to T center dot A in the allotetraploid cotton (*Gossypium hirsutum*) genome using a modified CRISPR/Cas9 system. *Plant Biotechnol. J.* **18**, 45-56.
- Qin, T., Liu, X.M., Li, J.J., Sun, J.B., Song, L.N., and Mao, T.L.** (2014). *Arabidopsis* Microtubule-Destabilizing Protein 25 Functions in Pollen Tube Growth by Severing Actin Filaments. *Plant Cell* **26**, 325-339.
- Qu, X.L., Zhang, R.H., Zhang, M., Diao, M., Xue, Y.B., and Huang, S.J.** (2017). Organizational Innovation of Apical Actin Filaments Drives Rapid Pollen Tube Growth and Turning. *Mol Plant* **10**, 930-947.
- Ran, F.A., Hsu, P.D., Lin, C.Y., Gootenberg, J.S., Konermann, S., Trevino, A.E., Scott, D.A., Inoue, A., Matoba, S., Zhang, Y., and Zhang, F.** (2013). Double Nicking by RNA-Guided CRISPR Cas9 for Enhanced Genome Editing Specificity. *Cell* **154**, 1380-1389.
- Rensing, S.A.** (2018). Great moments in evolution: the conquest of land by plants. *Curr. Opin. Plant Biol.* **42**, 49-54.
- Rensing, S.A., Goffinet, B., Meyberg, R., Wu, S.Z., and Bezanilla, M.** (2020). The Moss *Physcomitrium (Physcomitrella) patens*: A Model Organism for Non-Seed Plants. *Plant Cell* **32**, 1361-1376.

- Rensing, S.A., Lang, D., Zimmer, A.D., Terry, A., Salamov, A., Shapiro, H., Nishiyama, T., Perroud, P.F., Lindquist, E.A., Kamisugi, Y., Tanahashi, T., Sakakibara, K., Fujita, T., Oishi, K., Shin-I, T., Kuroki, Y., Toyoda, A., Suzuki, Y., Hashimoto, S., Yamaguchi, K., Sugano, S., Kohara, Y., Fujiyama, A., Anterola, A., Aoki, S., Ashton, N., Barbazuk, W.B., Barker, E., Bennetzen, J.L., Blankenship, R., Cho, S.H., Dutcher, S.K., Estelle, M., Fawcett, J.A., Gundlach, H., Hanada, K., Heyl, A., Hicks, K.A., Hughes, J., Lohr, M., Mayer, K., Melkozernov, A., Murata, T., Nelson, D.R., Pils, B., Prigge, M., Reiss, B., Renner, T., Rombauts, S., Rushton, P.J., Sanderfoot, A., Schween, G., Shiu, S.H., Stueber, K., Theodoulou, F.L., Tu, H., Van de Peer, Y., Verrier, P.J., Waters, E., Wood, A., Yang, L.X., Cove, D., Cuming, A.C., Hasebe, M., Lucas, S., Mishler, B.D., Reski, R., Grigoriev, I.V., Quatrano, R.S., and Boore, J.L. (2008). The *Physcomitrella* genome reveals evolutionary insights into the conquest of land by plants. *Science* **319**, 64-69.
- Riquelme, M., Aguirre, J., Bartnicki-Garcia, S., Braus, G.H., Feldbrugge, M., Fleig, U., Hansberg, W., Herrera-Estrella, A., Kamper, J., Kuck, U., Mourino-Perez, R.R., Takeshita, N., and Fischer, R. (2018). Fungal Morphogenesis, from the Polarized Growth of Hyphae to Complex Reproduction and Infection Structures. *Microbiology and Molecular Biology Reviews* **82**.
- Robatzek, S. (2007). Vesicle trafficking in plant immune responses. *Cell Microbiol* **9**, 1-8.
- Romano, N., and Macino, G. (1992). Quelling: transient inactivation of gene expression in *Neurospora crassa* by transformation with homologous sequences. *Mol. Microbiol.* **6**, 3343-3353.
- Rossi, A., Kontarakis, Z., Gerri, C., Nolte, H., Holper, S., Kruger, M., and Stainier, D.Y. (2015). Genetic compensation induced by deleterious mutations but not gene knockdowns. *Nature* **524**, 230-233.
- Rounds, C.M., and Bezanilla, M. (2013). Growth mechanisms in tip-growing plant cells. *Annu Rev Plant Biol* **64**, 243-265.
- Rozov, S.M., Permyakova, N.V., and Deineko, E.V. (2019). The Problem of the Low Rates of CRISPR/Cas9-Mediated Knock-ins in Plants: Approaches and Solutions. *Int. J. Mol. Sci.* **20**.
- Rutherford, S., and Moore, I. (2002). The Arabidopsis Rab GTPase family: another enigma variation. *Current opinion in plant biology* **5**, 518-528.
- Ryan, J.M., and Nebenfuhr, A. (2018). Update on Myosin Motors: Molecular Mechanisms and Physiological Functions. *Plant Physiology* **176**, 119-127.
- Rybak, K., Steiner, A., Synek, L., Klaeger, S., Kulich, I., Facher, E., Wanner, G., Kuster, B., Zarsky, V., Persson, S., and Assaad, F.F. (2014). Plant Cytokinesis Is Orchestrated by the Sequential Action of the TRAPP II and Exocyst Tethering Complexes. *Developmental Cell* **29**, 607-620.
- Sakai, K., Charlot, F., Le Saux, T., Bonhomme, S., Nogue, F., Palauqui, J.C., and Fattaccioli, J. (2019). Design of a comprehensive microfluidic and microscopic toolbox for the ultra-wide spatio-temporal study of plant protoplasts development and physiology. *Plant Methods* **15**.
- Samaj, J., Read, N.D., Volkmann, D., Menzel, D., and Baluska, F. (2005). The endocytic network in plants. *Trends Cell Biol.* **15**, 425-433.
- Schaefer, D., Zryd, J.P., Knight, C.D., and Cove, D.J. (1991). Stable Transformation of the Moss *Physcomitrella patens*. *Mol. Gen. Genet.* **226**, 418-424.
- Schaefer, D.G. (2001). Gene targeting in *Physcomitrella patens*. *Curr Opin Plant Biol* **4**, 143-150.
- Schaefer, D.G., and Zryd, J.P. (1997). Efficient gene targeting in the moss *Physcomitrella patens*. *Plant J.* **11**, 1195-1206.
- Schaefer, D.G., Delacote, F., Charlot, F., Vrielynck, N., Guyon-Debast, A., Le Guin, S., Neuhaus, J.M., Doutriaux, M.P., and Nogue, F. (2010). RAD51 loss of function abolishes gene targeting and de-represses illegitimate integration in the moss *Physcomitrella patens*. *DNA Repair* **9**, 526-533.
- Schaff, D.A. (1994). The adenine phosphoribosyltransferase (APRT) selectable marker system. *Plant Sci* **101**, 3-9.

- Schaff, D.A., Jarrett, R.A., Dlouhy, S.R., Ponniah, S., Stockelman, M., Stambrook, P.J., and Tischfield, J.A.** (1990). Mouse transgenes in human cells detect specific base substitutions. *P Natl Acad Sci USA* **87**, 8675-8679.
- Schneider, C.A., Rasband, W.S., and Eliceiri, K.W.** (2012). NIH Image to ImageJ: 25 years of image analysis. *Nat Methods* **9**, 671-675.
- Schott, D., Ho, J., Pruyne, D., and Bretscher, A.** (1999). The COOH-terminal domain of Myo2p, a yeast myosin V, has a direct role in secretory vesicle targeting. *J Cell Biol* **147**, 791-808.
- Schuh, M.** (2011). An actin-dependent mechanism for long-range vesicle transport. *Nature Cell Biology* **13**, 1431-U1115.
- Schwab, R., Ossowski, S., Riester, M., Warthmann, N., and Weigel, D.** (2006). Highly specific gene silencing by artificial microRNAs in *Arabidopsis*. *Plant Cell* **18**, 1121-1133.
- Segawa, K., Tamura, N., and Mima, J.** (2019). Homotypic and heterotypic trans-assembly of human Rab-family small GTPases in reconstituted membrane tethering. *J. Biol. Chem.* **294**, 7722-7739.
- Shan, Q.W., Wang, Y.P., Li, J., and Gao, C.X.** (2014). Genome editing in rice and wheat using the CRISPR/Cas system. *Nat. Protoc.* **9**, 2395-2410.
- Shimatani, Z., Kashojiya, S., Takayama, M., Terada, R., Arazoe, T., Ishii, H., Teramura, H., Yamamoto, T., Komatsu, H., Miura, K., Ezura, H., Nishida, K., Ariizumi, T., and Kondo, A.** (2017). Targeted base editing in rice and tomato using a CRISPR-Cas9 cytidine deaminase fusion. *Nat. Biotechnol.* **35**, 441-+.
- Small, I.** (2007). RNAi for revealing and engineering plant gene functions. *Curr. Opin. Biotechnol.* **18**, 148-153.
- Smih, F., Rouet, P., Romanienko, P.J., and Jasin, M.** (1995). Double-strand breaks at the target locus stimulate gene targeting in embryonic stem cells. *Nucleic Acids Res.* **23**, 5012-5019.
- Smits, A.H., Ziebell, F., Joberty, G., Zinn, N., Mueller, W.F., Clauder-Munster, S., Eberhard, D., Falth Savitski, M., Grandi, P., Jakob, P., Michon, A.M., Sun, H., Tessmer, K., Burckstummer, T., Bantscheff, M., Steinmetz, L.M., Drewes, G., and Huber, W.** (2019). Biological plasticity rescues target activity in CRISPR knock outs. *Nat Methods* **16**, 1087-1093.
- Speth, E.B., Imboden, L., Hauck, P., and He, S.Y.** (2009). Subcellular localization and functional analysis of the *Arabidopsis* GTPase RabE. *Plant Physiol* **149**, 1824-1837.
- Stenmark, H.** (2009). Rab GTPases as coordinators of vesicle traffic. *Nat Rev Mol Cell Bio* **10**, 513-525.
- Sternberg, S.H., LaFrance, B., Kaplan, M., and Doucina, J.A.** (2015). Conformational control of DNA target cleavage by CRISPR-Cas9. *Nature* **527**, 110-113.
- Stockle, D., Herrmann, A., Lipka, E., Lauster, T., Gavidia, R., Zimmermann, S., and Muller, S.** (2016). Putative RopGAPs impact division plane selection and interact with kinesin-12 POK1. *Nat Plants* **2**, 16120.
- Strepp, R., Scholz, S., Kruse, S., Speth, V., and Reski, R.** (1998). Plant nuclear gene knockout reveals a role in plastid division for the homolog of the bacterial cell division protein FtsZ, an ancestral tubulin. *Proc. Natl. Acad. Sci. U. S. A.* **95**, 4368-4373.
- Stroupe, C., and Brunger, A.T.** (2000). Crystal structures of a Rab protein in its inactive and active conformations. *J Mol Biol* **304**, 585-598.
- Struk, S., Jacobs, A., Sanchez Martin-Fontecha, E., Gevaert, K., Cubas, P., and Goormachtig, S.** (2019). Exploring the protein-protein interaction landscape in plants. *Plant Cell Environ.* **42**, 387-409.
- Sukrong, S., Yun, K.Y., Stadler, P., Kumar, C., Facciuolo, T., Moffatt, B.A., and Falcone, D.L.** (2012). Improved growth and stress tolerance in the *Arabidopsis oxt1* mutant triggered by altered adenine metabolism. *Mol Plant* **5**, 1310-1332.
- Sun, H., Furt, F., and Vidali, L.** (2018). Myosin XI localizes at the mitotic spindle and along the cell plate during plant cell division in *Physcomitrella patens*. *Biochem Biophys Res Commun.*

- Surkont, J., Diekmann, Y., and Pereira-Leal, J.B.** (2017). Rabifler2: an improved bioinformatic classifier of Rab GTPases. *Bioinformatics* **33**, 568-570.
- Synek, L., Schlager, N., Elias, M., Quentin, M., Hauser, M.T., and Zarsky, V.** (2006). AtEXO70A1, a member of a family of putative exocyst subunits specifically expanded in land plants, is important for polar growth and plant development. *Plant J.* **48**, 54-72.
- Szymanski, D., and Staiger, C.J.** (2018). The Actin Cytoskeleton: Functional Arrays for Cytoplasmic Organization and Cell Shape Control. *Plant Physiol.* **176**, 106-118.
- Takehita, N.** (2016). Coordinated process of polarized growth in filamentous fungi. *Biosci Biotech Bioch* **80**, 1693-1699.
- Tang, H., de Keijzer, J., Overdijk, E.J.R., Sweep, E., Steentjes, M., Vermeer, J.E.M., Janson, M.E., and Ketelaar, T.** (2019). Exocyst subunit Sec6 is positioned by microtubule overlaps in the moss phragmoplast prior to cell plate membrane arrival. *J. Cell Sci.* **132**.
- Thevenaz, P., Ruttimann, U.E., and Unser, M.** (1998). A pyramid approach to subpixel registration based on intensity. *IEEE Trans. Image Process.* **7**, 27-41.
- Thomas, K.R., and Capecchi, M.R.** (1987). Site-directed mutagenesis by gene targeting in mouse embryo-derived stem cells. *Cell* **51**, 503-512.
- Tominaga, M., Kimura, A., Yokota, E., Haraguchi, T., Shimmen, T., Yamamoto, K., Nakano, A., and Ito, K.** (2013). Cytoplasmic Streaming Velocity as a Plant Size Determinant. *Developmental Cell* **27**, 345-352.
- Tran, M.L., McCarthy, T.W., Sun, H., Wu, S.Z., Norris, J.H., Bezanilla, M., Vidali, L., Anderson, C.T., and Roberts, A.W.** (2018). Direct observation of the effects of cellulose synthesis inhibitors using live cell imaging of Cellulose Synthase (CESA) in *Physcomitrella patens*. *Sci. Rep.* **8**.
- Tuncbag, N., Gursoy, A., Nussinov, R., and Keskin, O.** (2011). Predicting protein-protein interactions on a proteome scale by matching evolutionary and structural similarities at interfaces using PRISM. *Nat Protoc* **6**, 1341-1354.
- van Damme, D., Coutuer, S., De Rycke, R., Bouget, F.Y., Inze, D., and Geelen, D.** (2006). Somatic cytokinesis and pollen maturation in *Arabidopsis* depend on TPLATE, which has domains similar to coat proteins. *Plant Cell* **18**, 3502-3518.
- van Gisbergen, P.A.C., Li, M., Wu, S.Z., and Bezanilla, M.** (2012). Class II formin targeting to the cell cortex by binding PI(3,5)P2 is essential for polarized growth. *J. Cell Biol.* **198**, 235-250.
- van Gisbergen, P.A.C., Wu, S.Z., Chang, M.Q., Pattavina, K.A., Bartlett, M.E., and Bezanilla, M.** (2018a). An ancient Sec10-formin fusion provides insights into actin-mediated regulation of exocytosis. *J Cell Biol* **217**, 945-957.
- van Gisbergen, P.A.C., Wu, S.Z., Chang, M.Q., Pattavina, K.A., Bartlett, M.E., and Bezanilla, M.** (2018b). An ancient Sec10-formin fusion provides insights into actin-mediated regulation of exocytosis. *J. Cell Biol.* **217**, 945-957.
- Van Leene, J., Eeckhout, D., Cannoot, B., De Winne, N., Persiau, G., Van De Slijke, E., Vercruyse, L., Dedecker, M., Verkest, A., Vandepoele, K., Martens, L., Witters, E., Gevaert, K., and De Jaeger, G.** (2015). An improved toolbox to unravel the plant cellular machinery by tandem affinity purification of Arabidopsis protein complexes. *Nat. Protoc.* **10**, 169-187.
- Veillet, F., Perrot, L., Guyon-Debast, A., Kermarrec, M.P., Chauvin, L., Chauvin, J.E., Gallois, J.L., Mazier, M., and Nogue, F.** (2020). Expanding the CRISPR Toolbox in *P. patens* Using SpCas9-NG Variant and Application for Gene and Base Editing in Solanaceae Crops. *Int. J. Mol. Sci.* **21**.
- Verkuijl, S.A., and Rots, M.G.** (2019). The influence of eukaryotic chromatin state on CRISPR-Cas9 editing efficiencies. *Curr Opin Biotechnol* **55**, 68-73.
- Vidali, L., and Bezanilla, M.** (2012). *Physcomitrella patens*: a model for tip cell growth and differentiation. *Curr. Opin. Plant Biol.* **15**, 625-631.

- Vidali, L., Augustine, R.C., Kleinman, K.P., and Bezanilla, M.** (2007a). Profilin is essential for tip growth in the moss *Physcomitrella patens*. *Plant Cell* **19**, 3705-3722.
- Vidali, L., Augustine, R.C., Kleinman, K.P., and Bezanilla, M.** (2007b). Profilin is essential for tip growth in the moss *Physcomitrella patens*. *The Plant Cell* **19**, 3705-3722.
- Vidali, L., Burkart, G.M., Augustine, R.C., Kerdavid, E., Tuzel, E., and Bezanilla, M.** (2010a). Myosin XI Is Essential for Tip Growth in *Physcomitrella patens*. *Plant Cell* **22**, 1868-1882.
- Vidali, L., Burkart, G.M., Augustine, R.C., Kerdavid, E., Tüzel, E., and Bezanilla, M.** (2010b). Myosin XI is essential for tip growth in *Physcomitrella patens*. *The Plant Cell* **22**, 1868-1882.
- Vidali, L., van Gisbergen, P.A.C., Guerin, C., Franco, P., Li, M., Burkart, G.M., Augustine, R.C., Blanchoin, L., and Bezanilla, M.** (2009). Rapid formin-mediated actin-filament elongation is essential for polarized plant cell growth. *P Natl Acad Sci USA* **106**, 13341-13346.
- Voigt, B., Timmers, A.C.J., Samaj, J., Hlavacka, A., Ueda, T., Preuss, M., Nielsen, E., Mathur, J., Emans, N., Stenmark, H., Nakano, A., Baluska, F., and Menzel, D.** (2005). Actin-based motility of endosomes is linked to the polar tip growth of root hairs. *Eur. J. Cell Biol.* **84**, 609-621.
- Voinnet, O., and Baulcombe, D.C.** (1997). Systemic signalling in gene silencing. *Nature* **389**, 553.
- Walton, R.T., Christie, K.A., Whittaker, M.N., and Kleinstiver, B.P.** (2020). Unconstrained genome targeting with near-PAMless engineered CRISPR-Cas9 variants. *Science* **368**, 290-+.
- Wang, H., Zhuang, X.H., Wang, X.F., Law, A.H.Y., Zhao, T., Du, S.W., Loy, M.M.T., and Jiang, L.W.** (2016). A Distinct Pathway for Polar Exocytosis in Plant Cell Wall Formation. *Plant Physiol.* **172**, 1003-1018.
- Wang, J., Zhang, Y., Wu, J., Meng, L., and Ren, H.** (2013). AtFH16, an *Arabidopsis* type II formin, binds and bundles both microfilaments and microtubules, and preferentially binds to microtubules. *J. Integr. Plant Biol.* **55**, 1002-1015.
- Wang, X.F., Chung, K.P., Lin, W.L., and Jiang, L.W.** (2018). Protein secretion in plants: conventional and unconventional pathways and new techniques. *J. Exp. Bot.* **69**, 21-37.
- Waterhouse, A., Bertoni, M., Bienert, S., Studer, G., Tauriello, G., Gumienny, R., Heer, F.T., de Beer, T.A.P., Rempfer, C., Bordoli, L., Lepore, R., and Schwede, T.** (2018). SWISS-MODEL: homology modelling of protein structures and complexes. *Nucleic Acids Res.*
- Weirich, K.L., Banerjee, S., Dasbiswas, K., Witten, T.A., Vaikuntanathan, S., and Gardel, M.L.** (2017). Liquid behavior of cross-linked actin bundles. *Proc. Natl. Acad. Sci. U. S. A.* **114**, 2131-2136.
- Welz, T., and Kerkhoff, E.** (2017). Exploring the iceberg: Prospects of coordinated myosin V and actin assembly functions in transport processes. *Small GTPases*, 1-11.
- Wen, T.J., Hochholdinger, F., Sauer, M., Bruce, W., and Schnable, P.S.** (2005). The roothairless1 gene of maize encodes a homolog of sec3, which is involved in polar exocytosis. *Plant Physiol.* **138**, 1637-1643.
- Wiedemann, G., van Gessel, N., Kochl, F., Hunn, L., Schulze, K., Maloukh, L., Nogue, F., Decker, E.L., Hartung, F., and Reski, R.** (2018). RecQ Helicases Function in Development, DNA Repair, and Gene Targeting in *Physcomitrella patens*. *Plant Cell* **30**, 717-736.
- Wienken, C.J., Baaske, P., Rothbauer, U., Braun, D., and Duhr, S.** (2010). Protein-binding assays in biological liquids using microscale thermophoresis. *Nat Commun* **1**, 100.
- Wilson, R.C., and Doudna, J.A.** (2013). Molecular mechanisms of RNA interference. *Annu Rev Biophys* **42**, 217-239.
- Wolf, L., Rizzini, L., Stracke, R., Ulm, R., and Rensing, S.A.** (2010). The molecular and physiological responses of *Physcomitrella patens* to ultraviolet-B radiation. *Plant Physiol.* **153**, 1123-1134.
- Wu, S.Z., and Bezanilla, M.** (2012). Transient RNAi assay in 96-well plate format facilitates high-throughput gene function studies in planta. *Methods Mol Biol* **918**, 327-340.
- Wu, S.Z., and Bezanilla, M.** (2014). Myosin VIII associates with microtubule ends and together with actin plays a role in guiding plant cell division. *Elife* **3**.

- Wu, S.Z., and Bezanilla, M.** (2018). Actin and microtubule cross talk mediates persistent polarized growth. *J. Cell Biol.* **217**, 3531-3544.
- Wu, S.Z., Ritchie, J.A., Pan, A.H., Quatrano, R.S., and Bezanilla, M.** (2011a). Myosin VIII Regulates Protonemal Patterning and Developmental Timing in the Moss *Physcomitrella patens*. *Mol Plant* **4**, 909-921.
- Wu, S.Z., Ritchie, J.A., Pan, A.H., Quatrano, R.S., and Bezanilla, M.** (2011b). Myosin VIII regulates protonemal patterning and developmental timing in the moss *Physcomitrella patens*. *Mol Plant* **4**, 909-921.
- Xing, S., Wallmeroth, N., Berendzen, K.W., and Grefen, C.** (2016). Techniques for the analysis of protein-protein interactions in vivo. *Plant Physiol.* **171**, 727-758.
- Xu, P., Zhang, Y.J., Kang, L., Roossinck, M.J., and Mysore, K.S.** (2006). Computational estimation and experimental verification of off-target silencing during posttranscriptional gene silencing in plants. *Plant Physiol* **142**, 429-440.
- Yamada, M., and Goshima, G.** (2018). The KCH Kinesin Drives Nuclear Transport and Cytoskeletal Coalescence to Promote Tip Cell Growth in *Physcomitrella patens*. *Plant Cell* **30**, 1496-1510.
- Yan, F., Kuang, Y.J., Ren, B., Wang, J.W., Zhang, D.W., Lin, H.H., Yang, B., Zhou, X.P., and Zhou, H.B.** (2018). Highly Efficient A.T to G.C Base Editing by Cas9n-Guided tRNA Adenosine Deaminase in Rice. *Mol Plant* **11**, 631-634.
- Yi, P.S., and Goshima, G.** (2020). Transient cotransformation of CRISPR/Cas9 and oligonucleotide templates enables efficient editing of target loci in *Physcomitrella patens*. *Plant Biotechnol. J.* **18**, 599-601.
- Yokota, E., Ueda, S., Tamura, K., Orii, H., Uchi, S., Sonobe, S., Hara-Nishimura, I., and Shimmen, T.** (2009). An isoform of myosin XI is responsible for the translocation of endoplasmic reticulum in tobacco cultured BY-2 cells. *Journal of Experimental Botany* **60**, 197-212.
- Zhang, N., Zhang, D., Chen, S.L., Gong, B.Q., Guo, Y., Xu, L., Zhang, X.N., and Li, J.F.** (2018). Engineering artificial microRNAs for multiplex gene silencing and simplified transgenic screen. *Plant Physiol* **178**, 989-1001.
- Zhang, T., Hu, Y., Jiang, W., Fang, L., Guan, X., Chen, J., Zhang, J., Saski, C.A., Scheffler, B.E., Stelly, D.M., Hulse-Kemp, A.M., Wan, Q., Liu, B., Liu, C., Wang, S., Pan, M., Wang, Y., Wang, D., Ye, W., Chang, L., Zhang, W., Song, Q., Kirkbride, R.C., Chen, X., Dennis, E., Llewellyn, D.J., Peterson, D.G., Thaxton, P., Jones, D.C., Wang, Q., Xu, X., Zhang, H., Wu, H., Zhou, L., Mei, G., Chen, S., Tian, Y., Xiang, D., Li, X., Ding, J., Zuo, Q., Tao, L., Liu, Y., Li, J., Lin, Y., Hui, Y., Cao, Z., Cai, C., Zhu, X., Jiang, Z., Zhou, B., Guo, W., Li, R., and Chen, Z.J.** (2015). Sequencing of allotetraploid cotton (*Gossypium hirsutum* L. acc. TM-1) provides a resource for fiber improvement. *Nat. Biotechnol.* **33**, 531-537.
- Zhang, Y.X., Malzahn, A.A., Sretenovic, S., and Qi, Y.P.** (2019). The emerging and uncultivated potential of CRISPR technology in plant science. *Nat Plants* **5**, 778-794.
- Zhang, Z., Zhang, Y., Tan, H.X., Wang, Y., Li, G., Liang, W.Q., Yuan, Z., Hu, J.P., Ren, H.Y., and Zhang, D.B.** (2011). RICE MORPHOLOGY DETERMINANT Encodes the Type II Formin FH5 and Regulates Rice Morphogenesis. *Plant Cell* **23**, 681-700.
- Zhao, Y., Yan, A., Feijo, J.A., Furutani, M., Takenawa, T., Hwang, I., Fu, Y., and Yang, Z.B.** (2010). Phosphoinositides Regulate Clathrin-Dependent Endocytosis at the Tip of Pollen Tubes in *Arabidopsis* and Tobacco. *Plant Cell* **22**, 4031-4044.
- Zhen, Y., and Stenmark, H.** (2015). Cellular functions of Rab GTPases at a glance. *J. Cell Sci.* **128**, 3171-3176.
- Zheng, H., Camacho, L., Wee, E., Batoko, H., Legen, J., Leaver, C.J., Malho, R., Hussey, P.J., and Moore, I.** (2005). A Rab-E GTPase mutant acts downstream of the Rab-D subclass in biosynthetic membrane traffic to the plasma membrane in tobacco leaf epidermis. *Plant Cell* **17**, 2020-2036.

- Zhou, C.J., Li, J., Zou, J.C., Liang, F.S., Ye, C.J., Jin, D.M., Weng, M.L., and Wang, B.** (2006). Cloning and characterization of a second form of the rice adenine phosphoribosyl transferase gene (OsAPT2) and its association with TGMS. *Plant Mol Biol* **60**, 365-376.
- Zhou, H.X., Rivas, G., and Minton, A.P.** (2008). Macromolecular crowding and confinement: biochemical, biophysical, and potential physiological consequences. *Annu Rev Biophys* **37**, 375-397.
- Zhu, L., Zhang, Y., Kang, E.F., Xu, Q.Y., Wang, M.Y., Rui, Y., Liu, B.Q., Yuan, M., and Fu, Y.** (2013). MAP18 Regulates the Direction of Pollen Tube Growth in *Arabidopsis* by Modulating F-Actin Organization. *Plant Cell* **25**, 851-867.
- Zimmer, A.M., Pan, Y.K., Chandrapalan, T., Kwong, R.W.M., and Perry, S.F.** (2019). Loss-of-function approaches in comparative physiology: is there a future for knockdown experiments in the era of genome editing? *J Exp Biol* **222**.
- Zong, Y., Wang, Y.P., Li, C., Zhang, R., Chen, K.L., Ran, Y.D., Qiu, J.L., Wang, D.W., and Gao, C.X.** (2017). Precise base editing in rice, wheat and maize with a Cas9-cytidine deaminase fusion. *Nat. Biotechnol.* **35**, 438-+.
- Zuo, J., Niu, Q.W., and Chua, N.H.** (2000). Technical advance: An estrogen receptor-based transactivator XVE mediates highly inducible gene expression in transgenic plants. *Plant J.* **24**, 265-273.